

sensors

Advanced Sensors for Real-Time Monitoring Applications

Edited by

Olga Korostynska and Alex Mason

Printed Edition of the Special Issue Published in *Sensors*

Advanced Sensors for Real-Time Monitoring Applications

Advanced Sensors for Real-Time Monitoring Applications

Editors

Olga Korostynska

Alex Mason

MDPI • Basel • Beijing • Wuhan • Barcelona • Belgrade • Manchester • Tokyo • Cluj • Tianjin



Editors

Olga Korostynska

Oslo Metropolitan University

Norway

Alex Mason

Norwegian University of Life Sciences

Norway

Editorial Office

MDPI

St. Alban-Anlage 66

4052 Basel, Switzerland

This is a reprint of articles from the Special Issue published online in the open access journal *Sensors* (ISSN 1424-8220) (available at: https://www.mdpi.com/journal/sensors/special.issues/Sensors_Real-Time_Monitoring_Applications).

For citation purposes, cite each article independently as indicated on the article page online and as indicated below:

LastName, A.A.; LastName, B.B.; LastName, C.C. Article Title. <i>Journal Name</i> Year , <i>Volume Number</i> , Page Range.
--

ISBN 978-3-0365-0426-1 (Hbk)

ISBN 978-3-0365-0427-8 (PDF)

© 2021 by the authors. Articles in this book are Open Access and distributed under the Creative Commons Attribution (CC BY) license, which allows users to download, copy and build upon published articles, as long as the author and publisher are properly credited, which ensures maximum dissemination and a wider impact of our publications.

The book as a whole is distributed by MDPI under the terms and conditions of the Creative Commons license CC BY-NC-ND.

Contents

About the Editors	vii
Preface to “Advanced Sensors for Real-Time Monitoring Applications”	ix
Irina Yaroshenko, Dmitry Kirsanov, Monika Marjanovic, Peter A. Lieberzeit, Olga Korostynska, Alex Mason, Ilaria Frau and Andrey Legin Real-Time Water Quality Monitoring with Chemical Sensors Reprinted from: <i>Sensors</i> 2020 , <i>20</i> , 3432, doi:10.3390/s20123432	1
Thi Thi Zin, Pann Thinzar Seint, Pyke Tin, Yoichiro Horii and Ikuo Kobayashi Body Condition Score Estimation Based on Regression Analysis Using a 3D Camera Reprinted from: <i>Sensors</i> 2020 , <i>20</i> , 3705, doi:10.3390/s20133705	25
Ritesh Misra, Hoda Jalali, Samuel J. Dickerson and Piervincenzo Rizzo Wireless Module for Nondestructive Testing/Structural Health Monitoring Applications Based on Solitary Waves Reprinted from: <i>Sensors</i> 2020 , <i>20</i> , 3016, doi:10.3390/s20113016	35
Daehyeon Yim, Won Hyuk Lee, Johanna Inhyang Kim, Kangryul Kim, Dong Hyun Ahn, Young-Hyo Lim, Seok Hyun Cho and Sung Ho Cho Quantified Activity Measurement for Medical Use in Movement Disorders through IR-UWB Radar Sensor Reprinted from: <i>Sensors</i> 2019 , <i>19</i> , 688, doi:10.3390/s19030688	53
Ning Chen, Jieji Zheng and Dapeng Fan Pre-Pressure Optimization for Ultrasonic Motors Based on Multi-Sensor Fusion Reprinted from: <i>Sensors</i> 2020 , <i>20</i> , 2096, doi:10.3390/s20072096	67
Se-beom Oh, Yong-moo Cheong, Dong-jin Kim and Kyung-mo Kim On-Line Monitoring of Pipe Wall Thinning by a High Temperature Ultrasonic Waveguide System at the Flow Accelerated Corrosion Proof Facility Reprinted from: <i>Sensors</i> 2019 , <i>19</i> , 1762, doi:10.3390/s19081762	83
David Gillett and Alan Marchiori A Low-Cost Continuous Turbidity Monitor Reprinted from: <i>Sensors</i> 2019 , <i>19</i> , 3039, doi:10.3390/s19143039	93
Nessrine Zemni, Fethi Bouksila, Magnus Persson, Fairouz Slama, Ronny Berndtsson and Rachida Bouhlila Laboratory Calibration and Field Validation of Soil Water Content and Salinity Measurements Using the 5TE Sensor Reprinted from: <i>Sensors</i> 2019 , <i>19</i> , 5272, doi:10.3390/s19235272	111
Wen Sha, Jiangtao Li, Wubing Xiao, Pengpeng Ling and Cuiping Lu Quantitative Analysis of Elements in Fertilizer Using Laser-Induced Breakdown Spectroscopy Coupled with Support Vector Regression Model Reprinted from: <i>Sensors</i> 2019 , <i>19</i> , 3277, doi:10.3390/s19153277	129
Baohua Zhang, Pengpeng Ling, Wen Sha, Yongcheng Jiang and Zhifeng Cui Univariate and Multivariate Analysis of Phosphorus Element in Fertilizers Using Laser-Induced Breakdown Spectroscopy Reprinted from: <i>Sensors</i> 2019 , <i>19</i> , 1727, doi:10.3390/s19071727	143

Joost Laurus Dinant Nelis, Laszlo Bura, Yunfeng Zhao, Konstantin M. Burkin, Karen Rafferty, Christopher T. Elliott and Katrina Campbell The Efficiency of Color Space Channels to Quantify Color and Color Intensity Change in Liquids, pH Strips, and Lateral Flow Assays with Smartphones Reprinted from: <i>Sensors</i> 2019 , <i>19</i> , 5104, doi:10.3390/s19235104	153
Chin-Chi Cheng, Yen-Hsiang Tseng and Shih-Chang Huang An Innovative Ultrasonic Apparatus and Technology for Diagnosis of Freeze-Drying Process Reprinted from: <i>Sensors</i> 2019 , <i>19</i> , 2181, doi:10.3390/s19092181	173
Lu Peng, Genqiang Jing, Zhu Luo, Xin Yuan, Yixu Wang and Bing Zhang Temperature and Strain Correlation of Bridge Parallel Structure Based on Vibrating Wire Strain Sensor Reprinted from: <i>Sensors</i> 2020 , <i>20</i> , 658, doi:10.3390/s20030658	187
Xiangming Liu and Valéri L. Markine Train Hunting Related Fast Degradation of a Railway Crossing—Condition Monitoring and Numerical Verification Reprinted from: <i>Sensors</i> 2020 , <i>20</i> , 2278, doi:10.3390/s20082278	203
X. Liu and V. L. Markine Correlation Analysis and Verification of Railway Crossing Condition Monitoring Reprinted from: <i>Sensors</i> 2019 , <i>19</i> , 4175, doi:10.3390/s19194175	223
Qiuming Nan, Sheng Li, Yiqiang Yao, Zhengying Li, Honghai Wang, Lixing Wang and Lizhi Sun A Novel Monitoring Approach for Train Tracking and Incursion Detection in Underground Structures Based on Ultra-Weak FBG Sensing Array Reprinted from: <i>Sensors</i> 2019 , <i>19</i> , 2666, doi:10.3390/s19122666	245
Lin Li, Hongli Hu, Yong Qin and Kaihao Tang Digital Approach to Rotational Speed Measurement Using an Electrostatic Sensor Reprinted from: <i>Sensors</i> 2019 , <i>19</i> , 2540, doi:10.3390/s19112540	261
Zhinong Jiang, Yuehua Lai, Jinjie Zhang, Haipeng Zhao and Zhiwei Mao Multi-Factor Operating Condition Recognition Using 1D Convolutional Long Short-Term Network Reprinted from: <i>Sensors</i> 2019 , <i>19</i> , 5488, doi:10.3390/s19245488	281
Ran Jia, Biao Ma, Changsong Zheng, Xin Ba, Liyong Wang, Qiu Du and Kai Wang Comprehensive Improvement of the Sensitivity and Detectability of a Large-Aperture Electromagnetic Wear Particle Detector Reprinted from: <i>Sensors</i> 2019 , <i>19</i> , 3162, doi:10.3390/s19143162	299
Andrzej Felski, Krzysztof Jaskólski, Karolina Zwolak and Paweł Piskur Analysis of Satellite Compass Error's Spectrum Reprinted from: <i>Sensors</i> 2020 , <i>20</i> , 4067, doi:10.3390/s20154067	319

About the Editors

Olga Korostynska has a B.Eng. (1998) and M.Sc. (2000) in Biomedical Engineering from National Technical University of Ukraine (KPI); Ph.D. (2003) in Electronics and Computer Engineering from the University of Limerick, Limerick, Ireland; and LLB (2011) from the University of Limerick, Limerick, Ireland. Currently, she is a Professor in Biomedical Engineering at Oslo Metropolitan University (OsloMet), Oslo, Norway. Before that, she was a Senior Lecturer in Advanced Sensor Technologies at the Liverpool John Moores University, Liverpool, UK. She was an EU Postdoctoral Research Fellow developing electromagnetic wave sensors for real-time water quality monitoring, as well as a Postdoctoral Researcher at the University of Limerick, working on a number of projects, including projects funded by IRCSET, EI, and EU FP7. She also was a Lecturer in Physics at Dublin Institute of Technology, Dublin, Ireland. Olga has co-authored a book, 15 book chapters, 4 UK patents, and over 200 scientific papers in peer-reviewed journals and conference proceedings.

Alex Mason has a B.Sc. (Hons), 2005, in Computer and Multimedia Systems from the University of Liverpool and Ph.D., 2008, in Wireless Sensor Networks and their Industrial Applications from Liverpool John Moores University. He led a sensor research team in Liverpool for several years as Reader in Sensor Technologies, before moving to Norway to take a dual industry/academic role. Today he is a Project Engineer at Animalia AS, Oslo, as well as Research Professor at the Norwegian University of Life Sciences (NMBU), Ås. Alex has a strong track record of over 200 publications, including several patents. He also leads a team working on food automation topics at NMBU, and amongst other activities co-ordinates the H2020 project RoBUTCHER, where sensing and robotics are key themes.

Preface to "Advanced Sensors for Real-Time Monitoring Applications"

It is impossible to imagine the modern world without sensors, or without real-time information about almost everything—from local temperature to material composition and health parameters. We sense, measure, and process data and act accordingly all the time. In fact, real-time monitoring and information is becoming the key to a successful business, an assistant in life-saving decisions that healthcare professionals make, a facility to optimize value-chains in manufacturing, and a tool in research that could revolutionize the future. To ensure that sensors address the rapidly developing needs of various areas of our lives and activities, scientists, researchers, manufacturers, and end-users have established an efficient dialogue so that the newest technological achievements in all aspects of real-time sensing can be implemented for the benefit of the wider community. This book documents some of the results of such a dialogue and reports on advances in sensors and sensor systems for existing and emerging real-time monitoring applications.

Olga Korostynska, Alex Mason

Editors

Review

Real-Time Water Quality Monitoring with Chemical Sensors

Irina Yaroshenko ¹, Dmitry Kirsanov ^{1,*}, Monika Marjanovic ², Peter A. Lieberzeit ², Olga Korostynska ^{3,4}, Alex Mason ^{4,5,6}, Ilaria Frau ⁶ and Andrey Legin ¹

¹ Institute of Chemistry, St. Petersburg State University, Mendeleev Center, Universitetskaya nab. 7/9, 199034 St. Petersburg, Russia; irina.s.yaroshenko@gmail.com (I.Y.); andrey.legin@gmail.com (A.L.)

² Faculty for Chemistry, Department of Physical Chemistry, University of Vienna, Waehringer Strasse 42, 1090 Vienna, Austria; Monika.Marjanovic@univie.ac.at (M.M.); Peter.Lieberzeit@univie.ac.at (P.A.L.)

³ Faculty of Technology, Art and Design, Department of Mechanical, Electronic and Chemical Engineering, Oslo Metropolitan University, 0166 Oslo, Norway; olga.korostynska@oslomet.no

⁴ Faculty of Science and Technology, Norwegian University of Life Sciences, 1432 Ås, Norway; alex.mason@nmbu.no

⁵ Animalia AS, Norwegian Meat and Poultry Research Centre, P.O. Box 396, 0513 Økern, Oslo, Norway

⁶ Faculty of Engineering and Technology, Liverpool John Moores University, Liverpool L3 3AF, UK; i.frau@2016.ljmu.ac.uk

* Correspondence: d.kirsanov@gmail.com; Tel.: +7-921-333-1246

Received: 25 May 2020; Accepted: 14 June 2020; Published: 17 June 2020

Abstract: Water quality is one of the most critical indicators of environmental pollution and it affects all of us. Water contamination can be accidental or intentional and the consequences are drastic unless the appropriate measures are adopted on the spot. This review provides a critical assessment of the applicability of various technologies for real-time water quality monitoring, focusing on those that have been reportedly tested in real-life scenarios. Specifically, the performance of sensors based on molecularly imprinted polymers is evaluated in detail, also giving insights into their principle of operation, stability in real on-site applications and mass production options. Such characteristics as sensing range and limit of detection are given for the most promising systems, that were verified outside of laboratory conditions. Then, novel trends of using microwave spectroscopy and chemical materials integration for achieving a higher sensitivity to and selectivity of pollutants in water are described.

Keywords: water quality; real-time monitoring; multisensor system; molecularly imprinted polymers; functionalised coating; microwave spectroscopy

1. Introduction

Water is one of the major natural resources for people. In 2012 it was declared that a safe water supply for every person is a crucially important task worldwide [1]. There are special water sustainability guides issued by the World Health Organization and regulated water quality standards [2]. The United Nations Sustainable Development Goals are the blueprint to achieving a better and more sustainable future for all-goal six specifically aims to ensure clean and accessible water. This, in turn, requires adequate water quality monitoring solutions specific to the situation. For example, summer 2019 was marked by catastrophic events in Norway, when more than 2000 people became sick, with more than 60 being hospitalized and 2 people dying as a result of an outbreak of *Campylobacter* and *Escherichia Coli* (*E. Coli*) that arose in the drinking water in Askøy, on the west coast of Norway. It is even more remarkable that this occurred in a country which has the status of being one of the countries with the highest quality of water in the world. The exact origin of the bacterial contamination that has

caused this is still not confirmed, but the fact that there is a need for real-time monitoring of all drinking water reservoirs everywhere is undisputed. Therefore, this review examines various technologies that could meet these demands.

The conventional approach to qualitative water analysis assumes application of various chemical, physical and microbiological methods [3]. Most such methods demand specialized laboratories equipped with expensive and sophisticated scientific devices. Furthermore, highly qualified personnel are needed to operate such devices and special efforts and manpower must be spent for representative water sampling. More effective water quality control methods must be developed. Such methods should be fast, low-cost, with minimum automatic sampling and, ultimately, provide real-time results.

2. Current Situation with Online Water Analysis

A comprehensive description of the current situation with online water analysis can be found in [4]. Mobile chemical analysis stations were used in this work to monitor different water parameters. The systems were deployed in specially produced trailers (Figure 1) that were towed to the river banks.

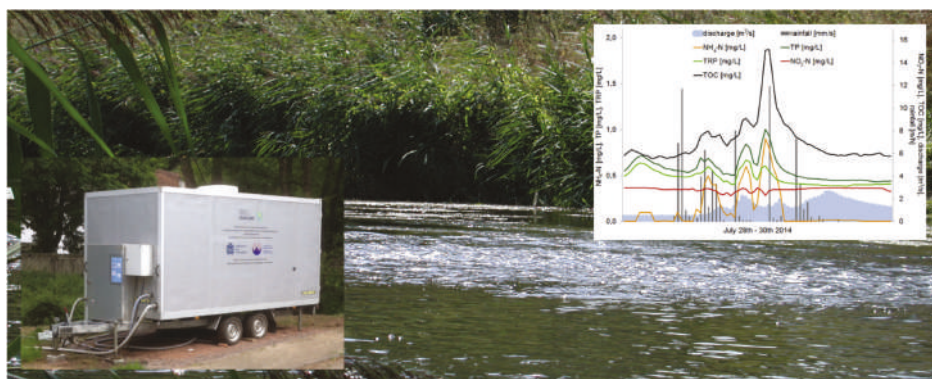


Figure 1. Mobile station for water quality monitoring and a sample of typical output of this station. Reprinted from *Science of the Total Environment*, Vol. 651, Angelika M. Meyer, Christina Klein, Elisabeth Fünfroeken, Ralf Kautenburger, Horst P. Beck, Real-time monitoring of water quality to identify pollution pathways in small and middle scale rivers, Pages 2323–2333, Copyright (2019), with permission from Elsevier.

The sensors, based on various principles, measured temperature, total phosphorus, pH and ammonium ions (by standard electrochemical sensors), dissolved oxygen, conductivity, nitrate ions and total organic carbon (by optical sensors). The measurements were performed by different stations in different locations. The measurement accuracy was within 10% for most measured parameters over 5 years of experiments in 35 locations along 25 small- and medium-size rivers. Such stations may likely improve our understanding of pollution types and pathways depending on water basins, seasonal factors and anthropogenic load. However, such stations cannot be considered as a practical instrument for wide-scale water quality monitoring due to their high cost, need for maintenance and significant power supply requirements.

Chemical sensors are attractive instruments for water quality analysis. The electrochemical or optical properties of such sensors may depend on the concentration of analytes in the water. Such sensors are already widely applied to the analysis of natural and potable water [5].

The growth of publication numbers in the field is shown in Figure 2.

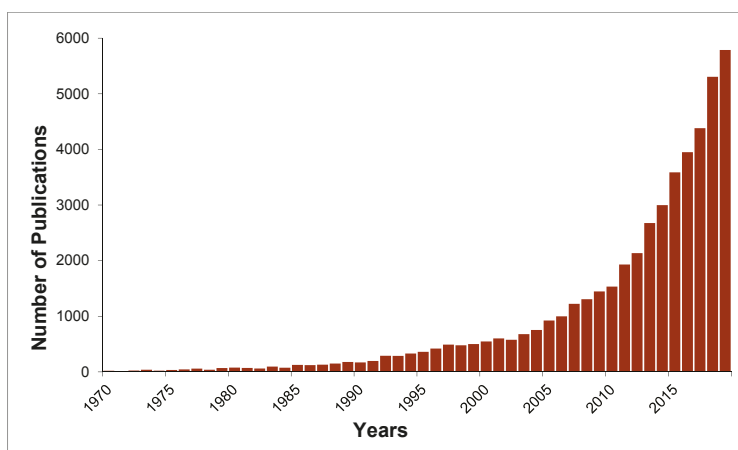


Figure 2. Number of publications published on the topic of the review in the last 50 years. Search keywords: “real-time water quality sensors”. Scopus (October 2019).

3. Water Quality Monitoring Systems

The first sensor really suitable for water monitoring was the glass pH electrode, which appeared, in the present shape, along with a pH meter, around 1930. Since then, pH is a primary parameter of most water monitoring devices.

It is obvious, however, that multiple water parameters must be evaluated to responsibly judge its quality and multisensor systems should be applied for such purposes.

There have been multiple attempts to develop multisensor systems that could be applied for water quality control, e.g., [6,7]. However, the first efforts mostly dealt with laboratory water analysis rather than being applied in real-time, online mode.

For instance, a voltammetric sensor array with four electrodes (Au, Pt, Ir and Rh) served for multisite water quality monitoring at a water treatment plant [8]. The aqueous samples were taken at nine filtration steps, as well as before and after the complete procedure of water purification. The voltammetric data were processed by principal component analysis (PCA), revealing pronounced difference between raw, rapidly filtered and clean water. However, it was observed that the samples collected after treatment by several slow filters were close to the rapidly filtered water samples on the PCA scores graph. This can potentially be explained by the low efficiency of these filters. Therefore, it was concluded that a multisensor system approach is suitable for continuous control of water quality at treatment facilities, indication of the possible malfunctioning units and for checking the water status after maintenance. Significant influence of sensor drift and the necessity to compensate this drift was pointed out.

The system developed in [9] was designed to measure pH, temperature, dissolved oxygen, conductivity, redox potential and turbidity. This set of parameters is the most common one in water quality assessment since the sensors for these parameters can run in continuous mode. The whole set of sensors was mounted on aluminum oxide. All sensors were united into a single PVC body and their outputs were collected by the data acquisition system, which could also perform remote data transmission. The work suggests that the body might be dipped into water or even built into water flow. The device also included a set of electric valves and pumps for sampling, cleaning and calibration. The authors proposed that such a portable system can be suitable for water quality monitoring from different sources.

Chinese authors published a paper where a multisensor system was applied for the determination of several elements such as iron, chromium, manganese, arsenic, zinc, cadmium, lead and copper [10].

The device comprised three analytical detection systems: a multiple light-addressable potentiometric sensor (MLAPS) based on a thin chalcogenide film for simultaneous detection of Fe(III) and Cr(VI) and two groups of electrodes for detection of other elements using anodic and cathodic stripping voltammetry. The following detection limits were obtained: Zn—60 µg/L, Cd—1 µg/L, Pb—2 µg/L, Cu—8 µg/L, Mn—60 µg/L, As—30 µg/L, Fe—280 µg/L and Cr—26 µg/L. The authors recommended their method to determine metals simultaneously in seawater and wastewater; however, the possibility of application of this device for online analysis was unclear.

Potable water quality is of primary interest to people. Such type of water was studied in [11], using two sensor stations. The first one was used for detecting free chlorine with a precision of 0.5% and limit of detection (LoD) of 0.02 mg/L, as well as total chloride by colorimetric method with precision of 5% and LoD 0.035 mg/L. The second station used was a multisensor for detection of pH, redox potential, dissolved oxygen, turbidity and conductivity. Eleven different contaminants were injected into the flow of the studied liquid, namely pesticides, herbicides, alkaloids, E. coli, mercury chloride and potassium ferricyanide. It was demonstrated that the set of sensors produces a response for each type of contaminants. Unfortunately, the work does not report any data about the precision of such systems during long-term application.

Another device for online water analysis was suggested in [12]. Fourteen buoys were installed in a freshwater lake; each of them was equipped with three ion-selective electrodes detecting the concentration of ammonium ions along with nitrate and chloride. Wireless connection between buoys could be implemented using Global System for Mobile Communications (GSM) and General Packet Radio Services (GPRS) protocols. The data was accumulated in a single place. The data was accessible via the internet allowing real-time control of the system performance (Figure 3).

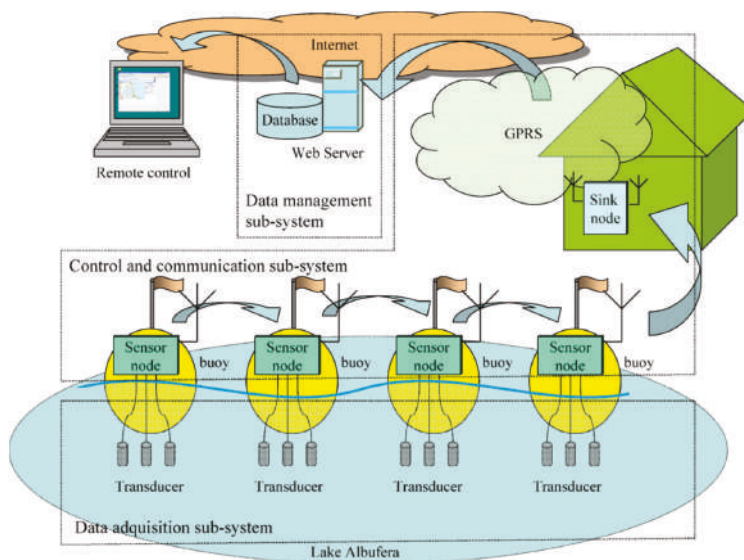


Figure 3. System for water quality monitoring. Reprinted from Talanta, Vol. 80, J.V. Capella, A. Bonastre, R. Ors, M. Perisa, A Wireless Sensor Network approach for distributed in-line chemical analysis of water, Pages 1789–1798, Copyright (2010), with permission from Elsevier.

The authors reported daily drift of sensor readings of about 1.5 mV. Since the measurements were performed for only 7 days, the accumulated drift was not that significant. However, the influence of drift can be critical over longer periods of time.

Two multisensor systems were suggested in [13] for environmental monitoring of various contaminants. One was dealing with contents of ammonium, potassium, and sodium in a river with low anthropogenic load. The second system was installed in river water in a populated region and was designed for detection of heavy metals such as copper, lead, zinc and cadmium. The systems were also equipped with radio transmission devices. The system was tested just for 8 h, which is obviously too short a period for any serious conclusions about such a technology.

Wider research was performed in [14], which was conducted over a period of 12 months. A sensor array comprising eight conducting polymer sensors for gas phase analysis was used to detect abrupt changes in the wastewater quality. Free gas emanating from bubbled liquid in the flow cell with constant temperature was delivered to the sensor chamber for analysis. The results of field tests at the water treatment plants using automatic systems produced water quality profiles and displayed the possibility of determining both random and model contaminants. This approach showed high sensitivity and flexibility and low dependence on long-term drift, daily oscillations, temperature and humidity. It must be noted, however, that the described experiments were carried out not at a real water treatment plant, but in a pilot system. Thus, the diversity of its performance may not be representative for real-world conditions. Besides, the idea to follow water quality via headspace analysis is obviously limited: it is impossible to follow contaminants which are not volatile enough.

4. Application of Biosensors and Optical Sensors for Water Quality Assessment

Biosensors were also used for water quality control, though quite a few of them were applied for online flow analysis. Pesticides were the main target of biosensors.

A system of biosensors capable of determining dichlorvos and methylparaoxon in the water was suggested in [15]. The systems consisted of three amperometric biosensors based on various AChE (acetylcholinesterase) enzymes. These enzymes were immobilised in a polymeric matrix onto the surface of screen-printing electrodes. The enzymes solutions were deposited over the electrode surface and irradiated by light, inducing photo polymerisation of the azide groups in the molecules. Such a sensor array was built into a flow system permitting automatic analysis. Bottled and river water was studied. The concentration of pesticides was detected in the ranges 10^{-4} – $0.1 \mu\text{M}$ for dichlorvos and 0.001 – $2.5 \mu\text{M}$ for methylparaoxon. Solely spiked samples were considered; therefore it is necessary to further verify performance of such a system in online mode.

Another work [16], reports on using Pt electrodes instead of screen-printed ones and self-made carbon paste was applied as a sensing layer. The paper implies that such a procedure may improve sensitivity of the substrate for some of the immobilized enzymes. The total number of biosensors in the array was eight. The ultimate aim of this research was not a quantification of pollutants but a global evaluation of water quality. It is doubtful though, if such a quality can be precisely determined by biosensors, which are highly selective to the main substance and would exhibit low cross-sensitivity to many other analytes present in the natural water.

One more attempt to evaluate global water toxicity by biosensors is described in [17]. The online toxicity monitoring system employed sulfur oxidizing bacteria (SOB) and consisted of three reactors. No toxicity changes in the natural flow water were observed over a period of six months. When the flow was spiked with diluted pig farm waste, the activity of sulfur oxidizing bacteria decreased by 90% in 1 h. The addition of $30 \mu\text{g/L}$ of nitrite ions or $2 \mu\text{g/L}$ of dichromate ions resulted in full degradation of sulfur oxidizing bacteria activity in 2 h. Thus, the sensitivity of the system to both inorganic and organic pollutants was demonstrated. It must be noted that one or two hours is a rather long period of time for detecting acute contaminations; functionality of the system could be regained only by introducing a new portion of bacteria, which significantly impairs real-time, online application of such device.

Optical sensors were also recently applied for water quality analysis, however, these are mostly discrete sensors, though tuned sometimes for integral parameters such as water color, turbidity or even COD and BOD. Discrete sensors were used to determine chlorophyll in the seawater on the basis

of its fluorescence [18], for evaluation of water opacity and color evolution by LED [19], for analysis of water turbidity and color in online mode [20] as well as for determination of heavy metal ions [21].

5. Biomimetic Approaches for Sensing Water Quality

5.1. Chemical Sensors for Sensing in “Real-Life Environments”

Biosensors reveal exceptional selectivity and often sensitivity, but usually are limited in terms of ruggedness and technical applicability in non-physiological conditions. One way to overcome this is to implement bioanalogous selectivity into systems that are able to withstand harsh and non-physiological conditions, so-called biomimetic systems [22]. Molecularly imprinted polymers (MIPs) are a promising example of such synthetic materials [23], since they are robust due to their highly cross-linked nature. Furthermore, they come at much lower costs than natural materials and provide longer storage and use periods. MIPs can also be produced for molecules that cannot be detected by natural receptors [24].

MIPs are generally synthesized by co-polymerization of functional and cross-linking monomers in the presence of a template (see Figure 4). Initially, a complex forms between functional monomers and the template through weak, noncovalent interactions (mainly hydrogen bonds, Van-der-Waals or π - π interactions), followed by polymerisation with cross-linking monomers to form a rigid, three-dimensional polymeric network. Removal of the template leads to recognition sites (cavities) within the polymer that are complementary to the target molecule in size, shape, and chemical functionality and are suitable to selectively rebind the analyte [25].

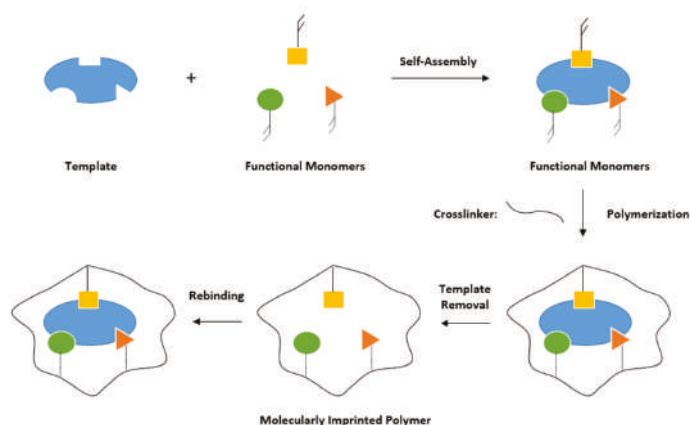


Figure 4. Schematic overview of molecular imprinting.

Except for MIPs, target recognition can also be obtained using other strategies. Aptamers, for example, are single-stranded RNA or DNA oligonucleotides, whose tertiary structure selectively binds their target molecules [26]. Another option is whole-cell-based sensors, which were also already applied to real wastewater samples [27,28]. In this case, mammalian cells were used for detecting harmful and toxic compounds, because their closeness physiology is close to that of humans. Although this strategy may not be regarded biomimetic in the strict sense of the word, it provides direct information about the overall toxicity of samples rather than detecting or quantifying one specific substance. When applying this method, unknown or new chemicals and pollutants may be detected. Kubisch et al. used rat myoblast cells in combination with a commercially available multiparametric readout system to measure impedance (morphological integrity) and two metabolic parameters—acidification and respiration—to investigate the overall toxicity and bioavailability of substances in water samples [27]. This was achieved by using three different types of electrodes on a single chip surface: impedance, pH and oxygen (CLARK) electrodes. After testing different test

compounds, including metal ions and neurotoxins, the system was exposed to real wastewater samples. It responded to different contaminants and was indeed suitable for monitoring unknown, harmful compounds in water. Similarly, the group of C. Guijarro applied rat liver cells in a whole-cell-based sensor system to monitor environmental contaminants, including an insecticide and a flame retardant, in water samples using the same analyzing system [28].

The aforementioned advantages of MIPs make them an attractive tool for different applications, such as solid phase extraction, drug targeting, development of sensors for various types of analytes, and environmental monitoring. Although the number of publications concerning MIP-based sensors is rising, only a small amount is actually applied to real-life environments or complex matrices. This part of the review will provide an overview of chemical sensors that were tested in (real-life) water samples with a special focus on receptor layers based on MIPs.

5.2. MIP-Based Sensors for Water Analyses

In 2018, Ayankojo et al. introduced a sensor system capable of detecting pharmaceutical pollution in aqueous solutions [29]. They chose amoxicillin as the model analyte and implemented a hybrid MIP, consisting of organic and inorganic components, on the gold surface of a surface plasmon resonance (SPR) transducer. The hybrid MIP film was synthesized by applying the sol-gel technique and using methacrylamide as organic monomer and vinyltrimethoxysilane as inorganic coupling agent to form a stable and rigid polymeric network. Sol-gels have a highly porous structure and recognition sites are usually formed in a more ordered way. This results in enhanced sensitivity and faster sensor response times. Rebinding experiments of the amoxicillin MIP in phosphate-buffered saline (PBS) and tap water revealed an imprinting factor of 16 compared to the nonimprinted polymer (NIP) and a limit of detection $LoD = 73$ pM. Furthermore, the MIP responded almost exclusively to its target analyte thus exhibiting utmost specificity. In the same year, the group of Cardoso also developed a sensor for detecting chloramphenicol, an antibiotic used in fish farms [30] (see Figure 5). The corresponding MIPs were electro-polymerized on screen-printed carbon electrodes.

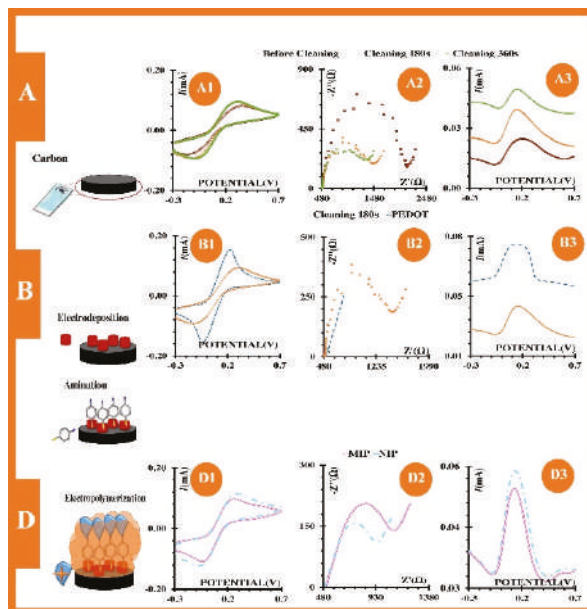


Figure 5. Construction principle and setup of chloramphenicol sensor. Reproduced from [30] with permission © Elsevier B.V. 2018.

Impedance and square wave voltammetry (SVW) in both electrolyte solution and water from a fish tank served to investigate the performance of the recognition element. In case of impedance measurements in electrolyte solution, sensor characteristics were linear in a concentration range from 1 nM to 100 μ M, achieving an LoD = 0.260 nM; SVW yielded similar characteristics and an LoD = 0.653 nM. In real-life samples—water from a fish tank—sensors responded linearly down to 1 nM and achieved an LoD of 0.54 nM and 0.029 nM for impedance and SVW measurements, respectively. These results suggest that there is no significant impact on sensor behavior when switching from standard solutions to real water samples leading to reproducible and sensitive sensor characteristics over five orders of magnitude down to 1 nM.

The real-life feasibility of MIP-based sensor systems were also demonstrated in case of detection of faecal contamination of seawater samples [31]. MIP nanoparticles were fabricated for sensing *Enterococcus faecalis* (*E. faecalis*) serving as faecal indicator to assess the water quality. Such MIP nanoparticles have the advantage of a higher surface-to-volume ratio, which means that the resulting cavities or binding sites are easier to access by target analytes [5]. *E. faecalis*-imprinted nanoparticles demonstrated good SPR sensor performance in aqueous and real seawater samples:

As can be seen from Figure 6, changes in refractive index were linear in a concentration range from 2×10^4 – 1×10^8 CFU/mL covering four orders of magnitude with a limit of detection of 1.05×10^2 CFU/mL. Selectivity studies with structurally similar bacteria revealed higher affinity of MIP nanoparticles towards the imprinted analyte compared to the other competitors. Selectivity coefficients for *E. coli*, *Staphylococcus aureus* and *Bacillus subtilis* were as follows: 1.38, 1.25 and 1.37.

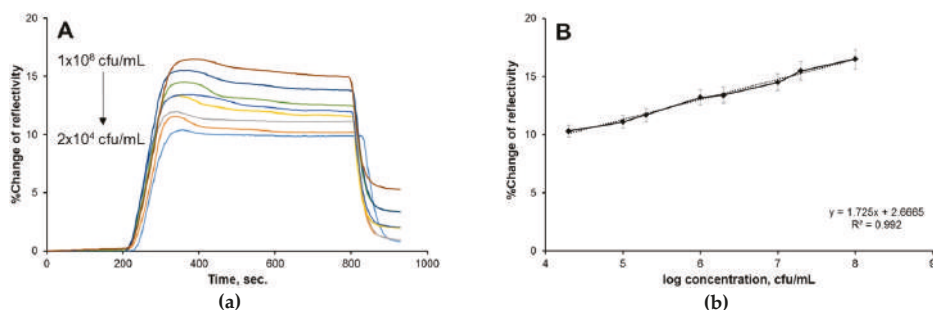


Figure 6. Sensor responses for faecal indicators, showing the (a) % change of reflectivity by time and (b) its linear correlation with the concentration. Reproduced from [31] with permission © Elsevier B.V. 2019.

Khadem et al. fabricated an electrochemical sensor for detecting diazinon, an insecticide, based on a modified carbon paste electrode combined with MIPs and multi-wall carbon nanotubes (MWCNTs) [32]. Using the latter modifier improves conductivity, whereas MIPs offer the necessary sensitivity towards the template molecule. After optimizing electrode composition, the method was first validated in aqueous standard solutions. SVW measurements revealed that the MIP showed much higher affinity to the analyte than the reference, the nonimprinted polymer; the system achieved linear performance in the concentration range from 5×10^{-10} to 1×10^{-6} mol/L with a calculated LoD = 1.3×10^{-10} mol/L. Furthermore, it was considerably more selective to the analyte than to other tested substances (ions and other pesticides). To investigate the applicability of the system to real biological and water samples, different amounts of diazinon were spiked to urine, tap and river water. In all these cases the sensors detected the target analyte with high recovery rates (>92%). This work demonstrates the use of MIP-based sensors in real-life samples and environments without the need of special sample pretreatment or preconcentration steps.

Another example for pesticide detection is presented in the work of Sroysee et al. [33]. They developed an MIP-based quartz crystal microbalance (QCM) sensor for quantification of carbofuran

(CBF) and profenofos (PFF). For that purpose, an in-house-developed dual-electrode system was used, where one electrode pair served as reference with the upper electrode being coated with the NIP. Doing so offers the advantage of measuring MIP and NIP simultaneously under the same conditions. Applying the bulk imprinting method, MIPs for PFF were based on polyurethanes whereas CBF MIPs were synthesized using acrylic monomers. Frequency measurements of MIP- and NIP-coated QCMs are shown in Figure 7.

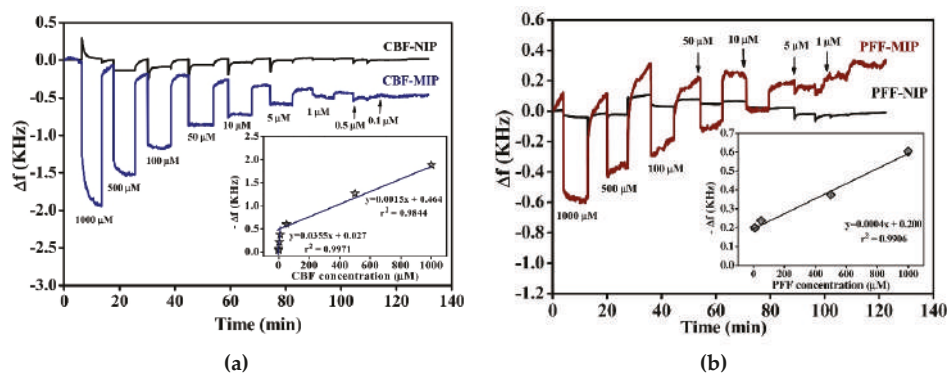


Figure 7. Frequency measurements of MIP- and NIP-coated QCMs for detection of (a) CBF and (b) PFF at different analyte concentrations. Reproduced from [33] Creative Commons License CC BY-NC-ND 4.0.

One can clearly see that both CBF and PFF MIPs led to linear sensor responses between 0.5–1000 μM and 5–1000 μM for CBF and PFF, respectively, whereas the frequency signal of the NIP stayed more or less constant.

Polycyclic aromatic hydrocarbons (PAH) are organic compounds which consist of at least two condensed aromatic rings. They are released into the environment through incomplete combustion of organic materials and considered to be mutagenic and carcinogenic. They usually occur in mixtures and their concentrations in air, water and sediments can be very low. Therefore, detection systems for PAH analysis need to be sensitive and selective. In particular, fluorescent sensors based on MIPs have gained in popularity due to their advantageous properties, such as high specificity, sensitivity and reversibility. Having a linear concentration dependency and low LoDs, those sensors seem to be quite promising for rapid detection of PAHs in aqueous solutions [34].

Sensors for the detection of nutrient components have been developed as well. For example, Warwick et al. reported a detection system based on MIPs combined with conductometric transducer for monitoring phosphates in environmental water samples [35]. Previous studies demonstrated that N-allylthiourea was the appropriate monomer for phosphate recognition [36]. The thiourea-based MIP was first optimized in terms of the optimal cross-linking monomer and ideal ratio of functional monomer to template (phenylphosphonic acid). Of all cross-linking monomers that were tested, ethylene glycol dimethacrylate (EGDMA) had the highest capacity of retaining phosphate as well as a monomer to template ratio of 2:1. After optimization, MIP membranes were integrated into the conductometric measuring cell. Selectivity tests in laboratory samples revealed no cross-talk to other ions, nitrate and sulfate. Both types of samples—standard and real-life ones—led to a linear increase in conductance with increased phosphate concentrations. In wastewater samples spiked with different amounts of potassium phosphate, the system allowed for LoD and LoQ values of 0.16 mg/L and 0.66 mg/L, respectively. The maximum acceptable amount of phosphate in wastewater is 1–2 mg/mL. The implemented sensor system with a linear range from 0.66 to 8 mg/mL therefore seems very promising for detecting small amounts of phosphate in environmental samples.

5.3. MIP-Based Sensors for On-Site Applications

For a pollutant sensor to be applicable on-site in real-life environments, it needs to be selective, reusable, robust and able to withstand harsh conditions. In 2015, Lenain et al. [37] reported a sensor that met all those criteria: it consists of spherical MIP beads deposited onto the electrodes of a capacitive transducer via electro-polymerization. Corresponding MIP beads for detecting metergoline—a model analyte for small molecules such as insecticides and pharmaceuticals—were synthesized through emulsion polymerization. Different concentrations of metergoline in PBS buffer were measured with the difference in capacitance between MIP and NIP representing the specific binding of the analyte as depicted in Figure 8. As shown in the figure, capacitance decreased with increased concentrations (10–50 μM). Furthermore, the system was able to regenerate itself without adding regeneration buffer, demonstrating reusability of the sensor.

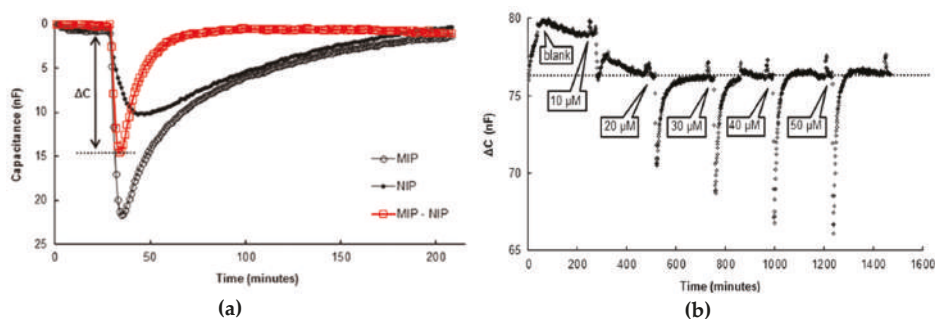


Figure 8. (a) Capacitance (nF) vs. time (min) of MIP, NIP and the differential signal ΔC (MIP-NIP). (b) Differential signal (ΔC in nF) for different concentrations of metergoline vs. time (min). Reproduced with permission from [37] © Elsevier. MIP: molecularly imprinted polymers, NIP: nonimprinted polymers.

The sensor was also able to withstand harsh environments and achieved both a low LoD (1 μM) and low cross-selectivity. All these results suggest its suitability for monitoring pollutions originating from substances like pesticides or antibiotics in water samples (rivers, seawater) on-site.

Another example of a method suitable to the monitoring of contaminants in water *in situ* was introduced by Cennamo et al. [38]. It consists of an SPR sensor with an integrated plastic optical fiber (POF) combined with MIPs for detecting the model analyte perfluorobutanesulfonic acid (PFBS). With an LoD of 1 ppb, an interface software and the ability to connect to the internet directly, the SPR-POF-MIP technique is inherently suitable to detect small concentrations of different toxic or harmful compounds in real water samples *in situ*. Other advantageous features such as its reduced size, robustness and remote sensing abilities are further key factors for industrial applications of MIP-based sensor systems.

5.4. Mass Production of MIP-Based Sensor Systems

To prove that MIP-based sensors are inherently suitable for mass manufacturing, Aikio et al. developed a low-cost and robust optical sensor platform based on integrated Young interferometer sensor chips, where waveguides were fabricated on top of a carrier foil via roll-to-roll manufacturing techniques [39]. For chemical sensing of melamine, MIPs were used as recognition materials, whereas for biosensing of multiple biomolecules, sensor chips were functionalized with antibodies. In case of melamine sensing, the change in phase depended on the analyte concentration: Sensor responses increased with higher concentrations. Furthermore, the reference (NIP) led to much lower phase changes compared to sensor responses of the MIP. However, injection of higher concentrations (>0.5 g/L) led to saturation effects. For multianalyte biosensing, the sensor chip was functionalised with antibodies

for C-reactive protein (CRP) and human chorionic gonadotropin (hCG) via inkjet printing. The results indicated that the Young interferometer bearing a specific antibody indeed selectively detected its corresponding protein. This work demonstrated the use of large-scale production techniques to develop a cost-efficient and rugged sensor system.

6. Functionalised Electromagnetic Wave Sensors

6.1. Microwave Spectroscopy and Water Analysis

Using electromagnetic (EM) waves at microwave frequencies for sensing purposes is an active research approach with potential for commercialization. This novel sensing approach has several advantages, including noninvasiveness, nondestructiveness, immediate response when the EM waves are in contact with a material under test, low-cost and power. Microwave spectroscopy provides the opportunity to guarantee continuous monitoring of water resources and intercept unexpected changes in water quality [40].

During the last 3 decades, microwave spectroscopy for liquid sensing has been investigated [41]. A water sample is placed in direct contact through a sensing structure and measured in real-time using an EM source (such as a vector network analyzer). The EM field interacts with the sample under test in a unique manner, depending on the polarization of water molecules and other compounds in the water samples, which produces a specific reflected or transmitted signal. The spectral response at specific frequencies depends on the conductivity and permittivity of the material under test [42]. Considering the variability of the sensing structures, the most successful experiments for detecting water quality were obtained using resonant cavities and planar sensors, due to the practicability of measuring a liquid sample.

Cavities resonate when the wavelength of the excitation within the cavity coincides with the cavity's dimension [43]. They enable noncontact, real-time measurements, as liquid samples in plastic or glass containers with known dimensions and properties can be inserted into the cavity. Several experiments have shown the resonant cavity ability to detect the presence and concentration of various materials. Specifically, cylindrical cavities were used to determine water hardness [43], nitrates [44], silver materials [45] and mixtures such as NaCl and KMnO_4 [46]. A rectangular resonant cavity was developed and tested for measuring pork-loin drip loss for meat production industry applications [47]. Another rectangular cavity was designed and tested for monitoring water quality, specifically the presence and concentration (>10 mg/L) of sulphides and nitrates [48].

During the last few years, several planar microwave sensors with different conformations have been developed and tested for differentiate compositions of water for both qualitative and quantitative concentration measurements [49–53]. Between planar sensing structures, Korostynska et al. [49] confirmed the action of a novel planar sensor with a sensing element consisted of interdigitated electrodes (IDE, also defined as interdigital by other researchers) metal patterns (silver, gold and/or copper) for water analysis observing changes in the microwave part of the EM spectrum analysing 20 μL of deionized water (DIW), KCl, NaCl and MnCl at various concentrations (Figure 9a,b). Then, Mason et al. [50], Moejes et al. [51] and Frau et al. [52] demonstrated the ability to detect respectively Lincomycin and Tylosin antibiotics, *Tetraselmis suecica* and lead ions (Pb^{2+}) using gold (Au) eight-pair IDE sensors.

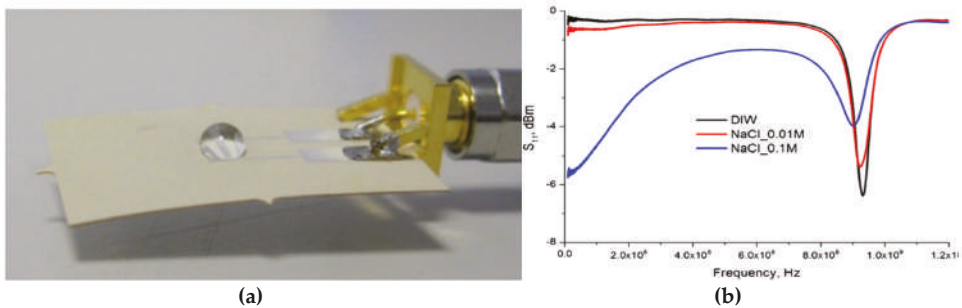


Figure 9. (a) Microwave flexible sensor with 20 μ L of water sample placed the silver IDEs and (b) its output sensing response comparing deionized water (DIW), and 0.01 and 0.1 M of NaCl. Reproduced with permission from [49] © 2020 IOP Publishing Ltd.

6.2. Progresses and Challenges in Microwave Spectroscopy

Microwave spectroscopy is an attractive option for detecting changes in materials in a noninvasive manner, at low cost with the option of portability and rapid measurements. This strategy, however, suffers from a deficiency of specificity, related to low sensitivity (Δ dB related with small changes in material changes) and selectivity (diverse spectral response for similar pollutants) [48,53]. Some of the disadvantages are also related to the capability to detect minor changes in the water sample which are not related to the changes in the target analyte, such as temperature and density [54].

There has been increasing research and development on understanding and improving the sensing performance of microwave spectroscopy for a deeper analysis of specific pollutants and small concentration changes related to them. Also, changes in the shape pattern of the sensing structure are not able to improve the performance of required sensitivity and selectivity of pollutants [55]. The bigger problem remains the detection of more than two pollutants at low concentrations.

Novel strategies are being adopted to improve sensitivity and selectivity using microwave spectroscopy, but no one has yet demonstrated the feasibility of distinguishing low concentrations of similar substances in water. Amirian et al. [56] simulated the feasibility of distinguishing between pure liquid materials, such as ethanol, ammonia, benzene and pentene using a novel sensor design and mathematical approach, reaching higher sensitivity and noise reduction. Harnsoongnoen et al. [57] demonstrated the discrimination of organic and inorganic materials using planar sensors and principal component analysis (PCA). Magnitude spectra at 2.3–2.6 GHz were able to measure specific concentrations of sucrose, glucose, NaCl and CaCl₂ citric acid between others, generating linear and nonlinear prediction models, correlating the transmission coefficient (S_{21}) and R^2 . PCR method was used to divide samples into two groups using the S_{21} magnitude: sugars and organic acids (blue oval) and salts (red oval) in Figure 10.

The following year Harnsoongnoen et al. [58] proposed a novel approach to discriminate between phosphorus and nitrate using the transmission coefficient and the ratio between the resonance frequency and the frequency bandwidth at the magnitude of 10 dB. This proposed method offers high sensitivity for both nitrate and phosphates, but not yet the required specificity.

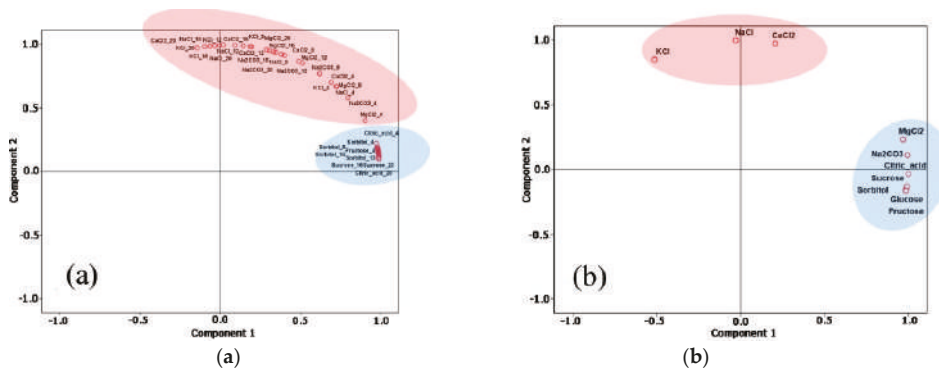


Figure 10. Discrimination between sugars and organic acid (blue oval) and salts (red ovals) using principal component analysis (PCA). (a): magnitudes of the transmission coefficient (S_{21}) between 2.3 and 2.6 GHz; (b): amplitude of S_{21} at the resonance frequency. Reproduced with permission from [57] © Elsevier.

Other researchers are using machine learning features for selecting and distinguishing a target material [44]. The developed model has been able to estimate the presence of nitrate in deionized water above the threshold, but it has not been able to quantify the precise concentration. Mason et al. [49] adopted a combined sensor approach using microwave analysis, combined with optical and impedance measurements for a more selective and sensitive determination of antibiotics, tylosin and lincomycin at different frequencies (at 8.7 and 1.8 GHz respectively) reaching high sensitivity (Figure 11a,b). Specifically, the selected planar microwave sensors were able to detect 0.20 $\mu\text{g/L}$ of lincomycin and 0.25 $\mu\text{g/L}$ of tylosin, a common concentration found in both surface and groundwater.

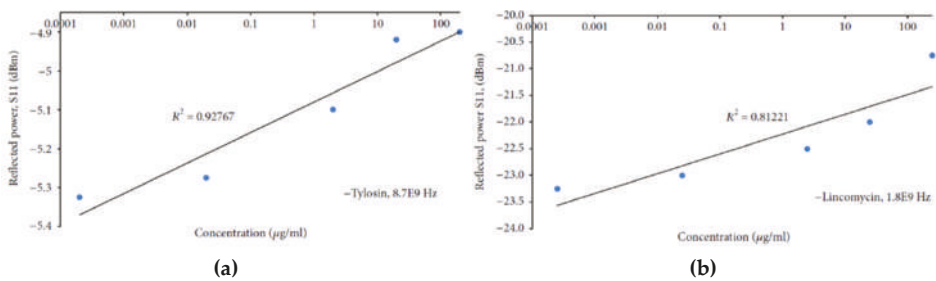


Figure 11. (a) Dependence of the S_{11} -transmitted signal on tylosin and lincomycin at respectively, 8.7 GHz and (b) 1.8 GHz. Copyright © [50] under the Creative Commons Attribution License.

6.3. Microwave and Materials Integration

Further improvement in sensitivity and selectivity are essential steps for water quality sensing, especially in complex mixtures [59]. A recent attractive approach is the integration of sensing materials onto the sensing structure, which has been experimented with the use of electrochemical impedance spectroscopy (EIS) and IDE sensors [60] using diverse coating thicknesses and for microwave gas sensing [61]. Planar sensors are an attractive option for the implementation of materials such as thin and thick films or microfluidic structures [53].

The synergy between microwave sensing technology and chemical materials provides interesting advantages in the field of quality monitoring for adapting this method to a specific purpose and it is consequently a promising area of research and development. The integration of specific materials in the form of thin and thick films onto planar sensors has been recently recognized as a novel and

attractive approach for reaching higher selectivity, sensitivity and specificity for a selected material under tests using microwave and impedance spectroscopy [59,62–64]. The principle is based on two processes: the sensing process, where the target analyte interacts, via physical or chemical interaction, with the material on the sensing structure, and the transduction process, where the interaction between EM waves, material and sample generate a particular signal [61]. A vector network analyser is used as a microwave source and can be configured with one or two ports. One-port configuration (S_{11} measurement) measures the reflection coefficient of a material under test, which depends on how much the incident wave propagates through, or is reflected by the sample. Two-port configuration (S_{21} measurement) allows for measuring the transmission coefficient, which depends on how much EM power propagates from one port (port 1) through the sample and is received at the second port (port 2). This configuration allows the determination of both transmitted and reflected signals. S-parameters vary with frequency. By functionalizing planar sensors with certain sensitive materials using screen-printing technology, which are defined functionalized electromagnetic sensors (f-EM) sensors, it is possible to obtain the desired sensitivity and/or selectivity to one or more specific analyte in water obtaining an immediate specific response as the sample is placed onto the microwave sensor (uncoated or f-EM sensor) [65] (Figure 12). Accordingly, such work has the foundations for developing new methods, based on EM sensors and functional chemical materials, capable of determining specific chemicals in water, both qualitatively and quantitatively [65]. The sensing response as S_{11} can be determined by direct contact between the material and the analyte under test, which changes the permittivity of each component, and the consequent overall complex permittivity changes. The improvement can be associated with the increase of material thickness as well as the composition itself [66].

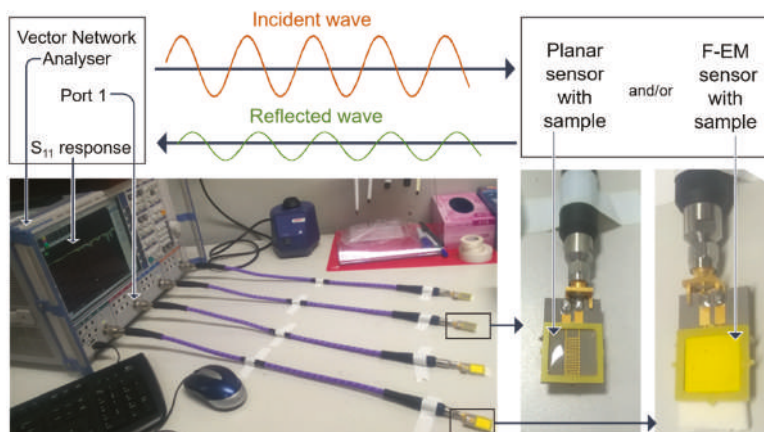


Figure 12. Scheme of the microwave interaction generated from a vector network analyser (VNA) which interact with a planar sensor (uncoated or functionalized with a coating, defined f-EM sensor) and a water sample placed onto it which generate a specific reflected signal (S_{11}) at selected frequencies. Reproduced from [65], Creative Commons Attribution 4.0 International License.

6.4. F-EM Sensors for Toxic Metals Analysis

Among the toxic elements, copper (Cu) and zinc (Zn) belong to the most common contaminants associated with mine wastes, which pollute water resources. Progress has been made in the last decade in developing chemo-sensors using mostly optical and electrochemical techniques. These are able to recognize specific metal ions using synthetic, natural and biological receptors [67], zeolites, inorganic oxides [68], organic polymers, biological materials [69], carbon-based materials [70] and

hybrid ion-exchangers [71]. The interaction between the material and metal ions is the base for accredited optical and electrochemical sensing systems for detecting small concentrations in water

Currently, no certified method can guarantee real-time monitoring of toxic metals in water. Microwave sensing technology is promising for facing this challenge, although new strategies must be developed for obtaining more specific response. The integration of certain sensitive materials onto the planar sensing structure can be used to obtain the desired sensitivity and/or selectivity to specific analytes in water. Among these functional chemical compounds, inorganic oxide compositions are considered advantageous owing to their strong adsorption and rapid electron transfer kinetics [68,72]. Inorganic materials have attracted considerable attention owing to their low cost, compatibility and strong adsorption of toxic metal ions [69]. For instance, zinc oxide (ZnO) nanoparticles are well-known for strongly adsorbing Cu and Pb ions [73].

Frau et al. [74] laid the foundations for developing new methods, based on EM sensors and functional chemical materials, capable of determining in real-time metal content in mining-impacted waters, both qualitatively and quantitatively. Specifically, integrating planar electromagnetic wave sensors operating at microwave frequencies with bespoke thick film coatings was proven feasible for monitoring of environmental pollution in water with metals caused by mining [74]. A recently developed f-EM sensor based on L-CyChBCZ (acronym for a mixture based on l-cysteine, chitosan and bismuth zinc cobalt oxide) was tested by probing a polluted water sample spiked with Cu and Zn solutions using the standard addition method. The S_{11} response has shown linear correlation with Cu and Zn concentration at three resonant frequencies. Especially at 0.91–1.00 GHz (peak 2) the f-EM sensor shows an improvement for Cu detection with an improvement in sensitivity, higher Q-factor and low LoD compared with an uncoated (UNC) sensor, shown in bold in Table 1 [74]. The sensor was able to detect Cu concentration with a limit of detection (LoD) of 0.036, just above the environmental quality standards for freshwater (28–34 $\mu\text{g/L}$) Responses for Cu and Zn were then compared by analysing microwave spectral responses using a Lorentzian peak fitting function and investigating multi-peaks (peaks 0–6) and multi-peaks' parameters (peak center, x_c , FWHM, w , area, A , and height, H , of the peaks) for specific discrimination between these two similar toxic metals [74]. It is useful to compare additional parameters for determining the selectivity, as it was demonstrated by Harnsoongnoen et al. [57], to distinguish between sugars and salts. However, more work is required for reaching higher discrimination between similar contaminants.

Table 1. Comparison of statistical features between uncoated and coated sensors for a water sample collected in a mining area spiked with Cu using the standard addition method. Reproduced from [74], Creative Commons Attribution 4.0 International License. LoD: limit of detection.

	R^2		CV (dB)		Sensitivity ($\Delta\text{dB}/\text{mg/L}$)		LoD (mg/L)		Q-Factor	
	UNC	f-EM	UNC	f-EM	UNC	f-EM	UNC	f-EM	UNC	f-EM
Peak 0	0.970	0.928	0.20	0.25	0.362	0.222	0.194	0.379	/	/
Peak 1	0.963	0.981	0.02	0.03	0.354	0.260	0.146	0.409	2.60	6.57
Peak 2	0.888	0.983	0.01	0.02	0.824	1.651	0.083	0.036	30.71	135.48

The microwave sensor functionalized with a 60- μm -thick $\beta\text{-Bi}_2\text{O}_3$ -based film was developed specifically for the detection of Zn in water [66]. It showed an improved performance compared with the uncoated sensor and repeatedly detected the changes of Zn concentrations in water at 0–100 ppm levels with a linear response (Figure 13). Globally, Zn concentrations in mine water can be greater than 500 ppm, with typical concentrations ranging from 0.1 to 10 ppm. Thus, the proposed system can be adapted as a sensing platform for monitoring Zn in water in abandoned mining areas that would be able to detect unexpected events of pollution and to clarify metal dynamics. As recently reported by Véléz et al. [75], the f-EM sensor based on $\beta\text{-Bi}_2\text{O}_3$ is the one that exhibits the best performance (but a

limited dynamic range) comparing glucose and NaCl, between others. Between the evaluated sensors, this sensor was the one that presented the highest sensitivity and the best resolution.

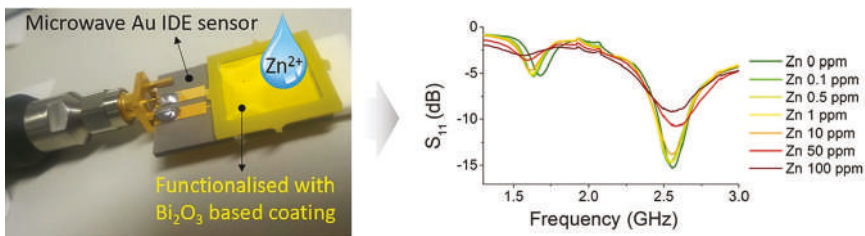


Figure 13. Microwave sensor functionalized with Bi₂O₃-based coating for the detection of Zn in water (left), and the dependence of the reflected signal (S_{11}) response on Zn concentration (right). Reproduced with permission from [66] © Elsevier.

6.5. F-EM Sensors for On-Site and In Situ Applications

The sensing system developed in [74] was tested on real water samples from two abandoned mining areas in Wales, UK, and evaluated the possibility of detecting both small and big differences between mining-impacted waters by comparing peak parameters in multiple peaks (Figure 14). Between the four samples, PM (a drainage adit from Parys Mountain mining district) was the most polluted (with 9.3 mg/L of Cu and 10.5 mg/L of Zn) compared to the other three samples (FA, MR and NC, from Wemyss mine) (with <0.001 mg/L of Cu and 2.9–9.3 mg/L of Zn). The sensor was able to distinguish between the two groups of samples in all the peaks, and at peaks 2–6 between the four samples, with both resonant frequency and amplitude shifts. Multiple peak characterization can give more information about the water composition. The sensor was able to perform a real-time identification of more- and less-polluted samples with high repeatability (with a coefficient of variation <0.05 dB), and evaluate changes in water composition. However, interferences were noticed, and more work is necessary for achieving higher selectivity.

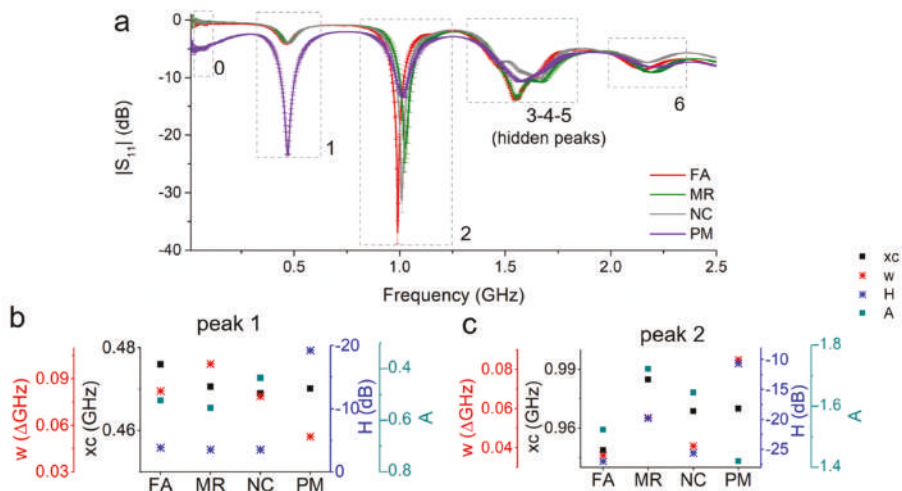


Figure 14. (a) Microwave spectral output for four polluted mining-impacted water samples collected in Wales (UK) analysed with an f-EM sensor based on L-CyCHBCZ coating and (b) peak parameters (w , x_c , H and A) comparison for peaks 1 and (c) 2. Reproduced from [74], Creative Commons Attribution 4.0 International License.

Therefore, f-EM sensors can be considered a feasible option for real-time monitoring of water quality for a broad range of pollutants. Choosing the right coating or sensor functionalization allows for adapting the system to selected pollutants in a given scenario to ensure sensor response with high selectivity and sensitivity.

The sensing structure was adapted for directly probing the water, for then providing an *in situ* monitoring. Despite many recent technological advances and positive results obtained using this novel sensing system, significant work remains to be accomplished before a reliable smart sensor for water quality monitoring is achievable. Real mine water is more complex and characterized by high levels of dissolved metals and sulphate and, frequently, low pH. Though, there are obviously several challenges that must be overcome before this technology can ensure that measurements correctly identify distinct contaminants, and qualifying and quantifying the interferences caused by complex water matrices and similar pollutants.

7. New Trends in Water Quality Monitoring

The most interesting and recent efforts of online water quality monitoring rely on multisensor systems based on electrochemical methods along with advances in data processing and automatization of measurements.

A miniature device was reported in [76], where the authors combined a pH meter and a conductometer for evaluating drinking water quality. The system was tested over a period of 30 days in water streams of different speeds. It was shown that the device was working stably under these conditions. Though pH and conductivity are important water parameters, they are obviously not enough for comprehensive evaluation of water quality.

The demand for simplicity of the analysis is gaining momentum in the recent years. A combination of paper-based sensors and a smartphone application is described as an analytical instrument for water quality monitoring in [77]. The paper sensors generate colorimetric signals depending on the content of certain analytes and the cell phone captures such signals and compares them to that from a clean control sample. The smartphone would also transmit the results to the special site mapping the water quality. The schematic of this system is shown in Figure 15.



Figure 15. Concept of water quality evaluation using paper-based colorimetric sensors and a smartphone. Reprinted from Water Research, Vol. 70, Clemence Sicard, Chad Glen, Brandon Aubie, Dan Wallace, Sana Jahanshahi-Anbuh, Kevin Pennings, Glen T. Daigger, Robert Pelton, John D. Brennan, Carlos D.M. Filipe, Tools for water quality monitoring and mapping using paper-based sensors and cell phones, Pages 360–369, Copyright (2015), with permission from Elsevier.

It was demonstrated that the system may quantify some organophosphorous pesticides like paraoxon and malathion in the natural water at the level 10^{-8} – 10^{-6} mol/L for both analytes. It is not clear however if such a device would perform correctly and precisely if multiple interfering species are present.

The successful application of a multisensor array for continuous online monitoring of processed water quality at an aeration plant was reported in [78]. The responses of 23 sensors of the array were continuously registered every seven seconds over a period of 26 days. The sensors were located in a special container with short direct connection to outlet water line of the aeration plant. The results of the multisensor were available immediately in a real-time mode. The use of topological data analysis (TDA) allowed for exploration of a very large dataset (295,828 measurements) accumulated through the whole period of continuous measurements. The achieved precision of analysis was suitable to monitor possible alarm events. No significant changes in water quality were observed over the experimental period. TDA helped visualizing some sharp changes related to sensor cleaning procedures and electrical power shortages.

Figure 16 shows a multisensor system (MSS) applied to evaluate integral and discrete parameters of wastewater at two urban water treatment plants around St. Petersburg (Russia) [79]. A closely similar system was used for evaluation of the water quality from the Ganga river and city ponds in Kolkata (India). Good correlations ($R^2 = 0.85$ for cross-validation) of MSS readings with COD values produced by laboratory chemical analysis were observed for all locations. This proves once again the applicability of MSS for real-time water quality analysis. A number of traditional water analytical parameters, such as ammonium and nitrate nitrogen and phosphorous were also determined with precision around 25% using the same MSS. All integral and discrete characteristics were calculated on the basis of the same set of measurements with MSS, without using any additional laboratory procedures, materials or qualified staff.



Figure 16. The sensor array after long-term online measurements at an aeration water plant. The sensors were cleaned by intensive washing. In spite of significant contamination, the sensors were stable for at least two months [79].

Along with traditional water quality analysis by analytical devices, a totally different approach has been developed. The global water toxicity (safety) can be also evaluated with the help of living creatures—from single-cell microorganisms to fishes, crustacea and mollusks. As a result, an ISO standard appeared in 1989, which suggested fresh water algae such as *Scenedesmus subspicatus* and *Selenastrum capricornutum* as a test. The decay of growth and reproduction of these bioassays is occurring in the contaminated water and can be used as its quality measure [80]. Another widespread

method is based on the application of *Vibrio fischeri* bacteria exhibiting variations of luminescence dependent on water pollution [81]. Unfortunately, such methods have also been burdened by specific drawbacks such as the necessity to strictly maintain the livestock of biotests and realistic analysis times of at least 15–30 min (and up to few days) depending on bioassay applied. Therefore, these approaches can hardly be treated as online ones.

It must be noted that multisensor devices can also perform like biotests. The toxicity of polluted water samples was evaluated in [82] by a standard bioassay method and a potentiometric multisensor system comprising 23 cross-sensitive electrodes. Real wastewater samples from different regions in Catalonia (Spain) in addition to a set of model aqueous solutions of hazardous substances (54 samples in total) were used for the measurements. The obtained data set was treated by several regression algorithms; the results of the bioassay tests, expressed as EC50 (the concentration of sample causing a 50% luminescence reduction), were taken as Y-variable. The regression models were validated by full cross-validation and randomized test set selection. It was demonstrated that the proposed system was able to evaluate integral water toxicity with the errors of EC50 prediction from 20% to 25%. The suggested sensor array can be implemented in online mode, unlike bioassay techniques, which makes it a beneficial tool in industrial water quality monitoring.

8. Conclusions

The global need for developing novel platforms for real-time monitoring of various water pollutants is well-recognized. This paper provides a critical assessment of recent achievements in real-time water quality monitoring with chemical sensors in particular. The focus is given to those systems that were reportedly tested online, with real water samples and their feasibility for long-term use is considered. The review shows that there are still many obstacles for having one sensing approach that would satisfy different situations. The most successful systems based on chemical sensing or its combination with other methods rely on specificity of a coating material that is capable of accurate detection of certain water pollutants, with molecularly imprinted polymers providing an increased flexibility for the designing of those systems.

Author Contributions: Conceptualization, A.L. and D.K.; writing—original draft preparation, I.Y.; writing—review and editing, A.L., I.F., A.M., O.K., M.M., P.A.L., and D.K. All authors have read and agreed to the published version of the manuscript.

Funding: D.K. and A.L.: acknowledge the funding from the RSF project #18-19-00151. I.Y. acknowledges partial financial support of this work from the RFBR project #18-53-80010.

Conflicts of Interest: The authors declare no conflict of interest.

References

1. The United Nations World Water Development Report 4: Managing Water under Uncertainty and Risk, Executive Summary. Available online: <https://unesdoc.unesco.org/ark:/48223/pf0000217175> (accessed on 19 October 2019).
2. Environment. Available online: http://ec.europa.eu/environment/water/water-drink/legislation_en.html (accessed on 19 October 2019).
3. Methods Approved to Analyze Drinking Water Samples to Ensure Compliance with Regulations. Available online: <https://www.epa.gov/dwanalyticalmethods> (accessed on 19 October 2019).
4. Meyer, A.M.; Klein, C.; Fünfroeken, E.; Kautenburger, R.; Beck, H.P. Real-time monitoring of water quality to identify pollution pathways in small and middle scale rivers. *Sci. Total. Environ.* **2019**, *651*, 2323–2333. [CrossRef]
5. Lvova, L.; Di Natale, C.; Paolesse, R. Chemical Sensors for Water Potability Assessment. In *Bottled Packaged Water*; Grumezescu, A., Holban, A.M., Eds.; Elsevier Science: Amsterdam, The Netherlands, 2019; Volume 7, pp. 177–208.
6. Legin, A.V.; Bychkov, E.A.; Seleznev, B.L.; Vlasov, Y.G. Development and analytical evaluation of a multisensor system for water quality monitoring. *Sens. Actuators. B Chem.* **1995**, *27*, 377–379. [CrossRef]

7. Rudnitskaya, A.; Ehlert, A.; Legin, A.; Vlasov, Y.G.; Büttgenbach, S. Multisensor system on the basis of an array of non-specific chemical sensors and artificial neural networks for determination of inorganic pollutants in a model groundwater. *Talanta* **2001**, *55*, 425–431. [[CrossRef](#)]
8. Krantz-Rülcker, C.; Stenberg, M.; Winquist, F.; Lundström, I. Electronic tongues for environmental monitoring based on sensor arrays and pattern recognition: A review. *Anal. Chim. Acta* **2001**, *426*, 217–226. [[CrossRef](#)]
9. Martinez-Manez, R.; Soto, J.; Garcia-Breijo, E.; Gil, L.; Ibanez, J.; Gadea, E. A multisensor in thick-film technology for water quality control. *Sens. Actuators. A Phys.* **2005**, *120*, 589–595. [[CrossRef](#)]
10. Men, H.; Zou, S.; Li, Y.; Wang, Y.; Ye, X.; Wang, P. A novel electronic tongue combined MLAPS with stripping voltammetry for environmental detection. *Sens. Actuators B Chem.* **2005**, *110*, 350–357. [[CrossRef](#)]
11. Yang, Y.J.; Haught, R.C.; Goodrich, J.A. Real-time contaminant detection and classification in a drinking water pipe using conventional water quality sensors: Techniques and experimental results. *J. Env. Manag.* **2009**, *90*, 2494–2506. [[CrossRef](#)] [[PubMed](#)]
12. Capella, J.V.; Bonastre, A.; Ors, R.; Peris, M. A Wireless Sensor Network approach for distributed in-line chemical analysis of water. *Talanta* **2010**, *80*, 1789–1798. [[CrossRef](#)] [[PubMed](#)]
13. Mimendia, A.; Gutierrez, J.M.; Leija, L.; Hernandez, P.R.; Favari, L.; Munoz, R.; del Valle, M. A review of the use of the potentiometric electronic tongue in the monitoring of environmental systems. *Environ. Modell. Softw.* **2010**, *25*, 1023–1030. [[CrossRef](#)]
14. Bourgeois, W.; Gardey, G.; Servieres, M.; Stuetz, R.M. A chemical sensor array based system for protecting wastewater treatment plants. *Sens. Actuators. B Chem.* **2003**, *91*, 109–116. [[CrossRef](#)]
15. Valdes-Ramirez, G.; Gutierrez, M.; del Valle, M.; Ramirez-Silva, M.T.; Fournier, D.; Marty, J.-L. Automated resolution of dichlorvos and methylparaoxon pesticide mixtures employing a Flow Injection system with an inhibition electronic tongue. *Biosens. Bioelectron.* **2009**, *24*, 1103–1108. [[CrossRef](#)] [[PubMed](#)]
16. Czolkos, I.; Dock, E.; Tønning, E.; Christensen, J.; Winther-Nielsen, M.; Carlsson, C.; Mojžíková, R.; Skládal, P.; Wollenberger, U.; Nørgaard, L.; et al. Prediction of wastewater quality using amperometric bioelectronic tongues. *Biosens. Bioelectron.* **2016**, *75*, 375–382. [[CrossRef](#)] [[PubMed](#)]
17. Hassan, S.H.A.; Gurung, A.; Kang, W.-G.; Shin, B.-S.; Rahimnejad, M.; Jeon, B.-H.; Kim, J.R.; Oh, S.-E. Real-time monitoring of water quality of stream water using sulfur oxidizing bacteria as bio-indicator. *Chemosphere* **2019**, *223*, 58–63. [[CrossRef](#)] [[PubMed](#)]
18. Attivissimo, F.; Carducci, C.G.C.; Lanzolla, A.M.L.; Massaro, A.; Vadrucci, M.R. A portable optical sensor for sea quality monitoring. *IEEE Sens. J.* **2015**, *15*, 146–153. [[CrossRef](#)]
19. Murphy, K.; Heery, B.; Sullivan, T.; Zhang, D.; Paludetti, L.; Lau, K.T.; Diamond, D.; Costa, E.; O'Connor, N.; Regan, F. A low-cost autonomous optical sensor for water quality monitoring. *Talanta* **2015**, *132*, 520–527. [[CrossRef](#)]
20. Skouteris, G.; Webb, D.P.; Shin, K.L.F.; Rahimifard, S. Assessment of the capability of an optical sensor for in-line real time wastewater quality analysis in food manufacturing. *Water. Resour. Ind.* **2018**, *20*, 75–81. [[CrossRef](#)]
21. Vaughan, A.A.; Narayanaswamy, R. Optical fibre reflectance sensors for the detection of heavy metal ions based on immobilised Br-PADAP. *Sens. Actuators. B Chem.* **1998**, *51*, 368–376. [[CrossRef](#)]
22. Lieberzeit, P.A.; Dickert, F.L. Sensor technology and its application in environmental analysis. *Anal. Bioanal. Chem.* **2007**, *387*, 237–247. [[CrossRef](#)]
23. Haupt, K.; Mosbach, K. Molecularly imprinted polymers and their use in biomimetic sensors. *Chem. Rev.* **2000**, *100*, 2495–2504. [[CrossRef](#)]
24. Latif, U.; Qian, J.; Can, S.; Dickert, F.L. Biomimetic receptors for bioanalyte detection by quartz crystal microbalances—From molecules to cells. *Sensors* **2014**, *14*, 23419–23438. [[CrossRef](#)]
25. Wackerlig, J.; Lieberzeit, P.A. Molecularly imprinted polymer nanoparticles in chemical sensing - Synthesis, characterisation and application. *Sens. Actuators B Chem.* **2015**, *207*, 144–157. [[CrossRef](#)]
26. Zhang, Y.; Lai, B.S.; Juhas, M. Recent advances in aptamer discovery and applications. *Molecular* **2019**, *24*, 941. [[CrossRef](#)] [[PubMed](#)]
27. Kubisch, R.; Bohrn, U.; Fleischer, M.; Stütz, E. Cell-based sensor system using L6 cells for broad band continuous pollutant monitoring in aquatic environments. *Sensors* **2012**, *12*, 3370–3393. [[CrossRef](#)] [[PubMed](#)]
28. Guijarro, C.; Fuchs, K.; Bohrn, U.; Stütz, E.; Wöfl, S. Simultaneous detection of multiple bioactive pollutants using a multiparametric biochip for water quality monitoring. *Biosens. Bioelectron.* **2015**, *72*, 71–79. [[CrossRef](#)] [[PubMed](#)]

29. Ayankojo, A.G.; Reut, J.; Öpik, A.; Furchner, A.; Syritski, V. Hybrid molecularly imprinted polymer for amoxicillin detection. *Biosens. Bioelectron.* **2018**, *118*, 102–107. [[CrossRef](#)] [[PubMed](#)]
30. Cardoso, A.R.; Tavares, A.P.M.; Sales, M.G.F. In-situ generated molecularly imprinted material for chloramphenicol electrochemical sensing in waters down to the nanomolar level. *Sens Actuators B Chem.* **2018**, *256*, 420–428. [[CrossRef](#)]
31. Erdem, Ö.; Saylan, Y.; Cihangir, N.; Denizli, A. Molecularly imprinted nanoparticles based plasmonic sensors for real-time *Enterococcus faecalis* detection. *Biosens. Bioelectron.* **2019**, *126*, 608–614. [[CrossRef](#)]
32. Khadem, M.; Faridbod, F.; Norouzi, P.; Rahimi Foroushani, A.; Ganjali, M.R.; Shahtaheri, S.J.; Yarahmadi, R. Modification of Carbon Paste Electrode Based on Molecularly Imprinted Polymer for Electrochemical Determination of Diazinon in Biological and Environmental Samples. *Electroanalysis* **2017**, *29*, 708–715. [[CrossRef](#)]
33. Sroysee, W.; Chunta, S.; Amatatongchai, M.; Lieberzeit, P.A. Molecularly imprinted polymers to detect profenofos and carbofuran selectively with QCM sensors. *Phys. Med.* **2019**, *7*, 100016. [[CrossRef](#)]
34. Nsibande, S.A.; Montaseri, H.; Forbes, P.B.C. Advances in the application of nanomaterial-based sensors for detection of polycyclic aromatic hydrocarbons in aquatic systems. *Trends Anal. Chem.* **2019**, *115*, 52–69. [[CrossRef](#)]
35. Warwick, C.; Guerreiro, A.; Gomez-Caballero, A.; Wood, E.; Kitson, J.; Robinson, J.; Soares, A. Conductance based sensing and analysis of soluble phosphates in wastewater. *Biosens. Bioelectron.* **2014**, *52*, 173–179. [[CrossRef](#)] [[PubMed](#)]
36. Warwick, C.; Guerreiro, A.; Wood, E.; Kitson, J.; Robinson, J.; Soares, A. A molecular imprinted polymer based sensor for measuring phosphate in wastewater samples. *Water Sci. Technol.* **2014**, *69*, 48–54. [[CrossRef](#)] [[PubMed](#)]
37. Lenain, P.; De Saeger, S.; Mattiasson, B.; Hedström, M. Affinity sensor based on immobilised molecular imprinted synthetic recognition elements. *Biosens. Bioelectron.* **2015**, *69*, 34–39. [[CrossRef](#)] [[PubMed](#)]
38. Cennamo, N.; Arcadio, F.; Perri, C.; Zeni, L.; Sequeira, F.; Billo, L.; Nogueira, R.; D’Agostino, G.; Porto, G.; Biasiolo, A. Water monitoring in smart cities exploiting plastic optical fibers and molecularly imprinted polymers. In Proceedings of the 2019 IEEE International Symposium on Measurements & Networking (M&N), Catania, Italy, 8–10 July 2019.
39. Aikio, S.; Zeilinger, M.; Hiltunen, J.; Hakalahti, L.; Hiitola-Keinänen, J.; Hiltunen, M.; Kontturi, V.; Siitonen, S.; Puustinen, J.; Lieberzeit, P.; et al. Disposable (bio)chemical integrated optical waveguide sensors implemented on roll-to-roll produced platforms. *RSC Adv.* **2016**, *6*, 50414–50422. [[CrossRef](#)]
40. Mohammadi, S.; Nadaraja, A.V.; Roberts, D.J.; Zarifi, M.H. Real-time and hazard-free water quality monitoring based on microwave planar resonator sensor. *Sens. Actuators A Phys.* **2020**, *303*, 111663. [[CrossRef](#)]
41. Zhang, K.; Amineh, R.K.; Dong, Z.; Nadler, D. Microwave sensing of water quality. *IEEE Access* **2019**, *7*, 69481–69493. [[CrossRef](#)]
42. Korostynska, O.; Mason, A.; Al-Shamma’a, A.I. Flexible microwave sensors for real-time analysis of water contaminants. *J. Electromagn. Waves Appl.* **2013**, *27*, 2075–2089. [[CrossRef](#)]
43. Teng, K.H.; Shaw, A.; Ateeq, M.; Al-Shamma’a, A.; Wylie, S.; Kazi, S.N.; Chew, B.T.; Kot, P. Design and implementation of a non-invasive real-time microwave sensor for assessing water hardness in heat exchangers. *J. Electromagn. Waves Appl.* **2018**, *32*, 797–811. [[CrossRef](#)]
44. Cashman, S.; Korostynska, O.; Shaw, A.; Lisboa, P.; Conroy, L. Detecting the presence and concentration of nitrate in water using microwave spectroscopy. *IEEE Sens. J.* **2017**, *17*, 4092–4099. [[CrossRef](#)]
45. Ateeq, M.; Shaw, A.; Garrett, R.; Dickson, P. A proof of concept study on utilising a non-invasive microwave analysis technique to characterise silver based materials in aqueous solution. *Sens. Imaging* **2017**, *18*, 13. [[CrossRef](#)]
46. Kapilevich, B.; Litvak, B. Microwave Sensor for Accurate Measurements of Water Solution Concentrations. In Proceedings of the 2007 Asia-Pacific Microwave Conference, Bangkok, Thailand, 11–14 December 2007.
47. Mason, A.; Abdullah, B.; Muradov, M.; Korostynska, O.; Al-Shamma’a, A.; Bjarnadottir, S.G.; Lunde, K.; Alvseike, O. Theoretical basis and application for measuring pork loin drip loss using microwave spectroscopy. *Sensors* **2016**, *16*, 182. [[CrossRef](#)] [[PubMed](#)]
48. Gennarelli, G.; Soldovieri, F. A non-specific microwave sensor for water quality monitoring. *Int. Water Technol. J.* **2013**, *3*, 70–77.

49. Korostynska, O.; Ortoneda-Pedrola, M.; Mason, A.; Al-Shamma'a, A.I. Flexible electromagnetic wave sensor operating at GHz frequencies for instantaneous concentration measurements of NaCl, KCl, MnCl₂ and CuCl solutions. *Meas. Sci. Technol.* **2014**, *25*, 065105. [[CrossRef](#)]
50. Mason, A.; Soprani, M.; Korostynska, O.; Amirthalingam, A.; Cullen, J.; Muradov, M.; Carmona, E.N.; Sberveglieri, G.; Sberveglieri, V.; Al-Shamma'a, A. Real-time microwave, dielectric, and optical sensing of lincomycin and tylosin antibiotics in water: Sensor fusion for environmental safety. *J. Sens.* **2018**, *2018*, 7976105. [[CrossRef](#)]
51. Moejes, K.; Sherif, R.; Dürr, S.; Conlan, S.; Mason, A.; Korostynska, O. Real-time monitoring of tetraselmis suecica in a saline environment as means of early water pollution detection. *Toxics* **2018**, *6*, 57. [[CrossRef](#)]
52. Frau, I.; Korostynska, O.; Mason, A.; Byrne, P. Comparison of electromagnetic wave sensors with optical and low-frequency spectroscopy methods for real-time monitoring of lead concentrations in mine water. *Mine Water Environ.* **2018**, *37*, 617–624. [[CrossRef](#)]
53. Zarifi, M.H.; Daneshmand, M. Liquid sensing in aquatic environment using high quality planar microwave resonator. *Sens. Actuators B Chem.* **2016**, *225*, 517–521. [[CrossRef](#)]
54. Al-Kizwini, M.A.; Wylie, S.R.; Al-Khafaji, D.A.; Al-Shamma'a, A.I. The monitoring of the two phase flow-annular flow type regime using microwave sensor technique. *Measurement* **2013**, *46*, 45–51. [[CrossRef](#)]
55. Salim, A.; Lim, S. Review of recent metamaterial microfluidic sensors. *Sensors* **2018**, *18*, 232. [[CrossRef](#)]
56. Amirian, M.; Karimi, G.; Wiltshire, B.D.; Zarifi, M.H. Differential narrow bandpass microstrip filter design for material and liquid purity interrogation. *IEEE Sens. J.* **2019**, *19*, 10545–10553. [[CrossRef](#)]
57. Harnsoongnoen, S.; Wanthong, A.; Charoen-In, U.; Siritaratiwat, A. Planar microwave sensor for detection and discrimination of aqueous organic and inorganic solutions. *Sens. Actuators B Chem.* **2018**, *271*, 300–305. [[CrossRef](#)]
58. Harnsoongnoen, S.; Wanthong, A.; Charoen-In, U.; Siritaratiwat, A. Microwave sensor for nitrate and phosphate concentration sensing. *IEEE Sens. J.* **2019**, *19*, 2950–2955. [[CrossRef](#)]
59. Zarifi, M.H.; Farsinezhad, S.; Abdolrazzagh, M.; Daneshmand, M.; Shankar, K. Selective microwave sensors exploiting the interaction of analytes with trap states in tio₂ nanotube arrays. *Nanoscale* **2016**, *8*, 7466–7473. [[CrossRef](#)] [[PubMed](#)]
60. Afsarimanesh, N.; Mukhopadhyay, S.C.; Kruger, M. Performance assessment of interdigital sensor for varied coating thicknesses to detect ctx-i. *IEEE Sens. J.* **2018**, *18*, 3924–3931. [[CrossRef](#)]
61. Li, F.; Zheng, Y.; Hua, C.; Jian, J. Gas sensing by microwave transduction: Review of progress and challenges. *Front. Mater.* **2019**, *6*. [[CrossRef](#)]
62. Azmi, A.; Azman, A.A.; Kaman, K.K.; Ibrahim, S.; Mukhopadhyay, S.C.; Nawawi, S.W.; Yunus, M.A.M. Performance of coating materials on planar electromagnetic sensing array to detect water contamination. *IEEE Sens. J.* **2017**, *17*, 5244–5251. [[CrossRef](#)]
63. Ebrahimi, A.; Withayachumnankul, W.; Al-Sarawi, S.; Abbott, D. High-sensitivity metamaterial-inspired sensor for microfluidic dielectric characterisation. *IEEE Sens. J.* **2014**, *14*, 1345–1351. [[CrossRef](#)]
64. Chen, T.; Li, S.; Sun, H. Metamaterials application in sensing. *Sensors* **2012**, *12*, 2742. [[CrossRef](#)]
65. Frau, I.; Wylie, S.; Byrne, P.; Cullen, J.; Korostynska, O.; Mason, A. New sensing system based on electromagnetic waves and functionalised em sensors for continuous monitoring of zn in freshwater. In Proceedings of the 11th ICARD | IMWA | MWD Conference—"Risk to Opportunity", Pretoria, South Africa, 10–14 September 2018.
66. Frau, I.; Wylie, S.; Byrne, P.; Cullen, J.; Korostynska, O.; Mason, A. Detection of zn in water using novel functionalised planar microwave sensors. *Mater. Sci. Eng. B* **2019**, *247*, 114382. [[CrossRef](#)]
67. Aragay, G.; Pons, J.; Merkoci, A. Recent trends in macro-, micro-, and nanomaterial-based tools and strategies for heavy-metal detection. *Chem. Rev.* **2011**, *111*, 3433–3458. [[CrossRef](#)]
68. Sen Gupta, S.; Bhattacharyya, K.G. Kinetics of adsorption of metal ions on inorganic materials: A review. *Adv. Colloid Interface Sci.* **2011**, *162*, 39–58. [[CrossRef](#)] [[PubMed](#)]
69. Cui, L.; Wu, J.; Ju, H. Electrochemical sensing of heavy metal ions with inorganic, organic and bio-materials. *Biosens. Bioelectron.* **2015**, *63*, 276–286. [[CrossRef](#)] [[PubMed](#)]
70. Wanekaya, A.K. Applications of nanoscale carbon-based materials in heavy metal sensing and detection. *Analysis* **2011**, *136*, 4383–4391. [[CrossRef](#)] [[PubMed](#)]
71. Chatterjee, P.K.; SenGupta, A.K. Toxic metal sensing through novel use of hybrid inorganic and polymeric ion-exchangers. *Solvent Extr. Ion Exch.* **2011**, *29*, 398–420. [[CrossRef](#)]

72. Gumpu, M.B.; Sethuraman, S.; Krishnan, U.M.; Rayappan, J.B.B. A review on detection of heavy metal ions in water—An electrochemical approach. *Sens. Actuators B Chem.* **2015**, *213*, 515–533. [CrossRef]
73. Bhatia, M.; Satish Babu, R.; Sonawane, S.H.; Gogate, P.R.; Girdhar, A.; Reddy, E.R.; Pola, M. Application of nanoadsorbents for removal of lead from water. *Int. J. Environ. Sci. Technol.* **2017**, *14*, 1135–1154. [CrossRef]
74. Frau, I.; Wylie, S.R.; Byrne, P.; Cullen, J.D.; Korostynska, O.; Mason, A. Functionalised microwave sensors for real-time monitoring of copper and zinc concentration in mining-impacted water. *Int. J. Environ. Sci. Technol.* **2019**, *17*, 1861–1876. [CrossRef]
75. Vélez, P.; Muñoz-Enano, J.; Gil, M.; Mata-Contreras, J.; Martín, F. Differential microfluidic sensors based on dumbbell-shaped defect ground structures in microstrip technology: Analysis, optimisation, and applications. *Sensors* **2019**, *19*, 3189. [CrossRef]
76. Banna, M.H.; Najjaran, H.; Sadiq, R.; Imran, S.A.; Rodriguez, M.J.; Hoorfar, M. Miniaturized water quality monitoring pH and conductivity sensors. *Sens. Actuators. B Chem.* **2014**, *193*, 434–441. [CrossRef]
77. Sicard, C.; Glen, C.; Aubie, B.; Wallace, D.; Jahanshahi-Anbuhi, S.; Pennings, K.; Daigger, G.T.; Pelton, R.; Brennan, J.D.; Filipe, C.D.M. Tools for water quality monitoring and mapping using paper-based sensors and cell phones. *Water Res.* **2015**, *70*, 360–369. [CrossRef]
78. Belikova, V.; Panchuk, V.; Legin, E.; Melenteva, A.; Kirsanov, D.; Legin, A. Continuous monitoring of water quality at aeration plant with potentiometric sensor array. *Sens. Actuators. B Chem.* **2019**, *282*, 854–860. [CrossRef]
79. Legin, E.; Zadorozhnaya, O.; Khaydukova, M.; Kirsanov, D.; Rybakina, V.; Zagrebin, A.; Ignatyeva, N.; Ashina, J.; Sarkar, S.; Mukherjee, S.; et al. Rapid Evaluation of Integral Quality and Safety of Surface and Wastewater s by a Multisensor System (Electronic Tongue). *Sensors* **2019**, *19*, 2019. [CrossRef] [PubMed]
80. International Organization for Standardization. *Water Quality—Fresh Water Algal Growth Inhibition Test with Scenedesmus Subspicatus and Selenastrum Capricornutum*, ISO 8692; International Organization for Standardization: Geneva, Switzerland, 1989; p. 12.
81. International Organization for Standardization. *Water Quality—Determination of The Inhibitory Effect of Water Samples on The Light Emission of Vibrio Fischeri (Luminescent bacteria test)*. ISO 11348-3; International Organization for Standardization: Geneva, Switzerland, 1998; p. 13.
82. Zadorozhnaya, O.; Kirsanov, D.; Buzhinsky, I.; Tsarev, F.; Abramova, N.; Bratov, A.; Muñoz, F.J.; Ribó, J.; Bori, J.; Riva, M.C.; et al. Water pollution monitoring by an artificial sensory system performing in terms of *Vibrio fischeri* bacteria. *Sens. Actuators. B Chem.* **2015**, *207*, 1069–1075. [CrossRef]



© 2020 by the authors. Licensee MDPI, Basel, Switzerland. This article is an open access article distributed under the terms and conditions of the Creative Commons Attribution (CC BY) license (<http://creativecommons.org/licenses/by/4.0/>).



Letter

Body Condition Score Estimation Based on Regression Analysis Using a 3D Camera

Thi Thi Zin ^{1,*}, Pann Thinzar Seint ¹, Pyke Tin ¹, Yoichiro Horii ² and Ikuo Kobayashi ³

¹ Graduate School of Engineering, University of Miyazaki, 1 Chome-1 Gakuenkibanadainishi, Miyazaki 889-2192, Japan; pantenzasein.t9@cc.miyazaki-u.ac.jp (P.T.S.); pyketin11@gmail.com (P.T.)

² Center for Animal Disease Control, University of Miyazaki, 1 Chome-1 Gakuenkibanadainishi, Miyazaki 889-2192, Japan; horii@cc.miyazaki-u.ac.jp

³ Field Science Center, Faculty of Agriculture, University of Miyazaki, 1 Chome-1 Gakuenkibanadainishi, Miyazaki 889-2192, Japan; ikuokob@cc.miyazaki-u.ac.jp

* Correspondence: thithi@cc.miyazaki-u.ac.jp

Received: 29 May 2020; Accepted: 29 June 2020; Published: 2 July 2020

Abstract: The Body Condition Score (BCS) for cows indicates their energy reserves, the scoring for which ranges from very thin to overweight. These measurements are especially useful during calving, as well as early lactation. Achieving a correct BCS helps avoid calving difficulties, losses and other health problems. Although BCS can be rated by experts, it is time-consuming and often inconsistent when performed by different experts. Therefore, the aim of our system is to develop a computerized system to reduce inconsistencies and to provide a time-saving solution. In our proposed system, the automatic body condition scoring system is introduced by using a 3D camera, image processing techniques and regression models. The experimental data were collected on a rotary parlor milking station on a large-scale dairy farm in Japan. The system includes an application platform for automatic image selection as a primary step, which was developed for smart monitoring of individual cows on large-scale farms. Moreover, two analytical models are proposed in two regions of interest (ROI) by extracting 3D surface roughness parameters. By applying the extracted parameters in mathematical equations, the BCS is automatically evaluated based on measurements of model accuracy, with one of the two models achieving a mean absolute percentage error (MAPE) of 3.9%, and a mean absolute error (MAE) of 0.13.

Keywords: body condition score; 3D surface roughness parameters; rotary parlor; 3D camera; regression analysis

1. Introduction

Tracking body condition scores (BCS), and using them to avoid rapid fluctuations in body weight during the production cycle, has a positive impact on decision-making in dairy farm management, and makes economic sense. It is also useful for improving milk production, health, and reproduction (pregnancy rate) throughout the production cycle. The resulting improved monitoring provides an opportunity to fine-tune nutrition, and healthcare more generally. Although various methods are available for evaluating body condition, many producers use the BCS system, which ranks cattle using an arbitrary scale, and does not rely on body weight [1]. The BCS is assigned by scoring the amount of fat that is observed on several skeletal parts of the cow. Various scoring systems are used to arrive at the BCS, which are used to assign a number as the score. As the system most commonly used, the BCS ranges from 1 to 5, in increments of 0.5 or 0.25. Very thin cows are given a BCS of '1', and very obese cows are rated as '5'. The intermediate stages of BCS can be characterized as thin, ideal and obese. A 'very thin' cow has prominent hips and spine. The hips and spine of a 'thin' cow are easily felt without pressure, and those of an 'ideal' cow can be felt with firm pressure. A 'very obese' cow is

heavily covered by fat. BCS '3' is considered ideal. Cows can then be managed and fed according to the requirements for attaining an optimal BCS.

Research results indicate that optimizing BCS can positively influence the health and productivity of dairy cows. In addition, a rapid decrease in the BCS after calving closely correlates with metabolic disorders and other problems [2]. Current interpretations of available evidence indicate that metabolic disorders affect the immune system of dairy cows during the critical transition from calving [3]. BCS decreases during the approximate 100-day period from calving through early lactation to peak milk, and then increases through dry-off. Generally, maintaining an optimal BCS is needed to avoid extremes of too fat or too lean [4]. For a proper evaluation of BCS, the observer must be familiar with skeletal structures and fat reserves, as described in [5]. In the measurement of BCS using vision-based technology, tailhead and loin areas are of primary concern. Many researchers have evaluated BCS by manually checking off significant anatomical points on digital 2D images. Hook angles and tailhead depressions are formulated to estimate BCS, using a technique introduced in 2008 by Bewley et al. [6]. In this technique, the skeletal checkpoints associated with anatomical structures are used in the assessment of BCS. However, automating the identification of these checkpoints with 2D images is difficult. A new perspective for measuring fat levels in cows is proposed using ultrasonography in [7]. It shows that the larger the BCS, the more the increase in the fat reserves. In recent years, single 3D camera and multiple 3D cameras with multiple viewpoints have been introduced to evaluate the body condition score by using machine vision technology. In our system, we introduce the BCS automation system by using a single 3D camera that is mounted above the rotary parlor.

2. Related Work

To rate BCS, a technique was introduced by Edmonson et al. in [8], which consists of manually assessing the amount of body fat around the tailhead, as well as by palpation of the tailhead (the depression beneath the tail), and the pelvis (hook and pin bones). In an automated system, an image analysis technique was introduced to derive relevant characteristics from anatomical points, and from intensities or depth values in regions of interest and cow contours. By using a low-cost 3D camera, an automatic body condition scoring system was developed by implementing an image-processing technique and regression algorithms [9]. In this system, fourteen features correlated with BCS were used (such as age, weight, and height), including some features that were derived from video images, and automatically derived from farm records. The accuracy of the entire system was 0.26 of mean absolute error (MAE). In [10], an automated BCS rating system was introduced, which assesses scores from 1.5 to 4.5 by extracting multiple features related to body condition from three viewpoints. In this system, body images are recorded using 3-dimensional cameras positioned above, behind, and to the right. Anatomical landmarks are automatically identified, and then bony prominences and surface depressions are quantified to evaluate BCS and provide the result.

In our own previous work, we proposed a noninvasive method for automatically evaluating BCS [11]. This method starts with a 3D image, from which two analytical models are created, one using the root-mean-square deviation (RMSD), and the other using the convex hull volume parameter. This method resulted in a standard error of 0.35 using RMSD, and 0.19 using convex hull volume. We also noticed that convex hull volume has a strong correlation with BCS. The benefits of continuously monitoring BCS are intuitive to most dairy producers, nutritionists, and others involved in dairy farming. A few dairy farms have incorporated such monitoring as part of their management strategy, as described in [12]. In our previous paper of body condition indicators described in [13], we noted a strong link between BCS and parameters such as convex hull volume and mean height, with BCS ratings between 3.5 and 3.75. That system also introduced variations in BCS trends during the calving and lactation intervals using values for monthly mean height. In [14], a low-cost monitoring system was proposed for unobtrusively and regularly monitoring BCS, lameness, and weight using 3D imaging technology. In the paper described in [14], a new approach for assessing BCS based on a rolling ball algorithm was validated by achieving repeatability within ± 0.25 BCS. Our approach included

automatic image selection steps for each cow in the parlor that was targeted for a smart application of continuous monitoring. The approach also featured a newly developed BCS estimation model using two region of interests (ROI) visible from above. Finally, this approach also involves extracting 3D surface roughness features, and generalizing two linear regression models to estimate BCS by applying the proposed parameters.

3. Data Collection and Preprocessing

In our proposed system, a 3D camera is mounted 3.4 m above a rotary parlor. Data collection is done at a large-scale dairy farm in Oita Prefecture, Japan. The position of the 3D camera and an illustration of cows in the parlor are seen in Figure 1a,b. The 3D camera generates a resolution of 132×176 pixels in X, Y, and Z directions. X and Y are the x and y coordinates of the image and Z is the distance information (z or D_0) of the image.

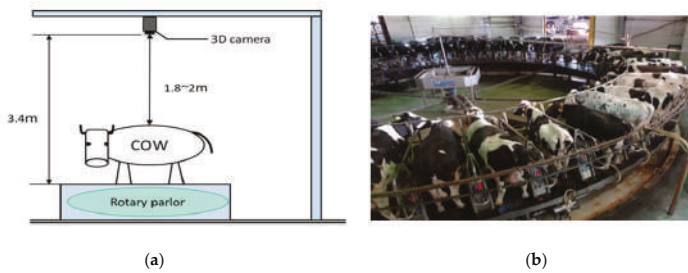


Figure 1. (a) Position of 3D camera; (b) image of cows in rotary parlor.

The proposed system uses a single 3D camera and generates data in csv format (comma-separated values). Each line of the csv data has 23,232 values for distance information, which is preprocessed into image dimensions of 132×176 pixels. The transformed image has a maximum of three cows. An original image obtained using this camera is shown in Figure 2a. The original image shows the distance data (D_0) from the camera center to the image plane. To obtain real-world data for the distance from the ground, the difference between D_0 and the camera height ($3.4 - D_0$) m is calculated. The distance range between 1.21 m and 2.1 m is considered to be the cow region, as shown in Figure 2b. Conversely, the background region is automatically removed by the extraction of the cow region. Each of the cows has their related ID number, using radio frequency identification (RFID). Therefore, we only extract the middle cow image as the desired ID number on the rotary parlor, as shown in Figure 3a,b. The sided images of other ID numbers are conversely removed. In Figure 3a, ROI 1 and ROI 2 are the two regions of interest used for BCS estimation, for which details are discussed in Section 4.

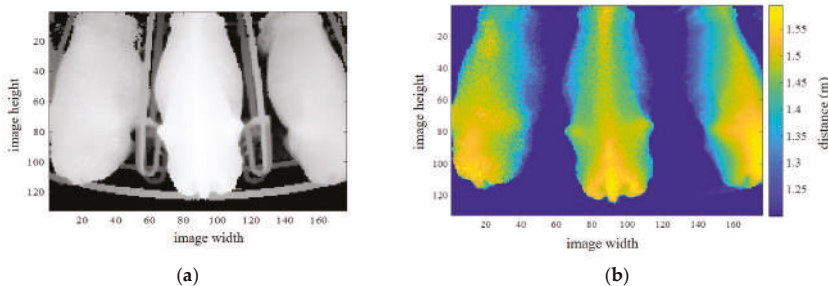


Figure 2. Cow region extraction from 3D camera. (a) Original image in rotary parlor from 3D camera; (b) Cow region extraction by distance information.

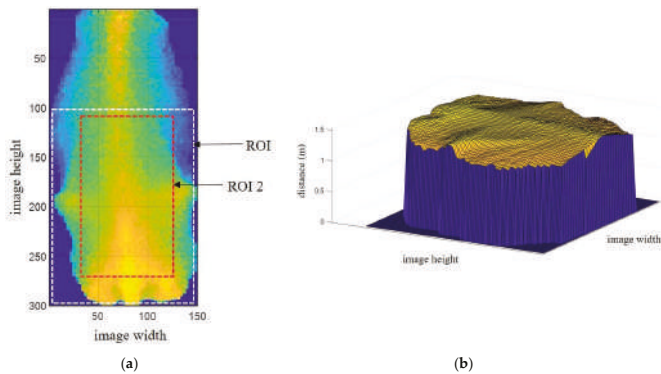


Figure 3. The processed cow image. (a) Distance image of cow (color expresses the distance); (b) The cow image in 3D space.

4. Automatic Image Selection Process by Filtering

Sometimes, the 3D camera returns distorted images. These bad images are removed using geometric and hole areas. A sample of images discarded due to distortion and touching between cows is shown in Figure 4a. The selected cow images are grouped by ID number. From all of the cow images recorded, filtering ensures that only one good position of cow image for the same ID number on the same day is selected by using the symmetry parameter, though the camera generally captures three images per day in the milking parlor. Filtering is performed by a comparison of symmetry. The filtering for cow ID “LA982123529378694” is shown in Figure 4b. This cow has camera capture times (at 04:57 a.m., 13:22 p.m., and 21:21 p.m. on 4th November 2019), and the selected filtered image is shown by a red marker. When the left and right sides of the image are symmetric, the difference between the two areas is nearly zero. The image with the least difference in value is selected as the most symmetric image, filtered from the images collected every day.

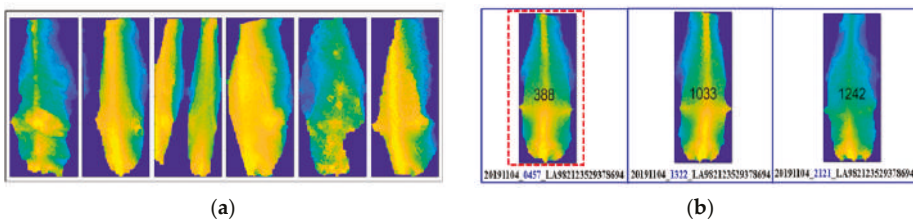


Figure 4. Sample discarded and filtered images. (a) Sample of discarded images; (b) Image selection by symmetry.

A detailed workflow for the automatic image selection process by filtering is shown in Figure 5. After making the cow extraction with the filtering step, each of the selected or filtered images is stored by its ID group in the database for further implementation of the smart system. In our system, approximately 20,000 images were automatically discarded by geometric area as bad images, and over 140,000 selected images were recorded from August 2018 to February 2020.

The proposed work is performed on Windows 10, an Intel[®] Core[™] i7-7700 CPU, @ 3.6 GHz. The processing time for the cow selection process from each set of csv data is approximately 0.2 s. BCS is a good management tool for developing nutrition and care programs for specific situations. This is the first step in improving the use of BCS. Follow-on steps include developing a BCS monitoring program for each individual cow, determining the BCS at calving, and then monitoring changes in BCS during lactation. Optimal scores can be devised for each cow at each stage of the production

cycle, i.e., the optimal score for calving is 3.25 and the optimal score at the start of breeding is 3, and so on. Therefore, we launched this study to automate an accurate assessment of BCS in the next step of BCS modeling.

This section includes a discussion of automatic collecting of cow images from a 3D camera. The remaining sections of the paper include a discussion of collecting cow images and their use in building models in Section 4, experimental use and performance evaluation of the two analytical models in Section 5, and a presentation of conclusions, as well as prospective work, in Section 6.

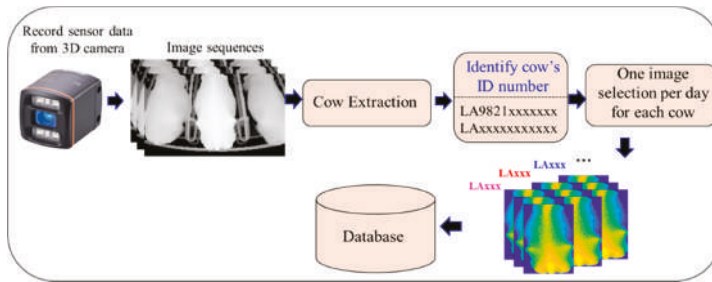


Figure 5. Detailed workflow for automatic image selection.

5. Proposed BCS Modeling

BCS is generally evaluated by experts who have been trained in its use. Though this conventional method is time- and labor-intensive, automation can ease the burden. Using manual measurements for BCS as a baseline or for referencing a model, a reliable automated system can be established. To confirm the performance of the proposed system, we used images of cows with manually measured BCS values in the range of 2.5 to 4. These cow images were collected from two different farms: (1) the Sumiyoshi Livestock Science Station, Field Science Center, University of Miyazaki, and (2) a large-scale dairy farm in Oita Prefecture, Japan. Two experts performed these initial manual measurements. Although the possible BCS scores range from 1 to 5 for very thin to very obese cows, respectively, BCS values between 2.5 and 4 are the most frequently seen. Our BCS dataset is shown in Table 1. In order to evaluate BCS values, two analytical models ($M1$ and $M2$) are proposed for the automated system. In total, 52 cows were used in the experiment, 32 for training, and an additional 20 for testing. $M1$ was applied to ROI 1, and $M2$ was applied to ROI 2, as seen in Figure 3a. The learning parameters were extracted for the two regions of interest (ROI 1 and ROI 2) using the concept of 3D roughness texture, which can be seen in surface texture analysis ASME-B46.1 (American Society of Mechanical Engineers 2002).

Table 1. BCS dataset taken by experts.

Body Condition Score (BCS)	2.5	2.75	3	3.25	3.5	3.75	4
No. of Cows	1	1	6	24	14	5	1

5.1. BCS Estimation Model 1

In the 3D image of a cow's backbone, BCS estimation model 1 was used for ROI 1, which is two-thirds of the whole cow body starting from the tailhead, as seen in Figure 3a. Variations in the amount of fat reserves or in the energy balance are apparent in that region. Moreover, the more that body fat covers the bones, the larger the BCS. Visually, we can clearly differentiate thin cows from fat ones by this coverage by fat. Therefore, roughness parameters are extracted to determine the BCS. Figure 6 shows images composed of cross-sectional slices in ROI 1 for each BCS value between 2.5 and 4 in increments of 0.25. In this proposed region, the following parameters were extracted:

- i. Arithmetic mean height (A_1);

- ii. Convex hull volume (A_2);
- iii. Difference between convex hull volume and 3D volume (A_3);
- iv. Difference between peak height and valley depth in fifteen maximums and minimums for all profiles (A_4).

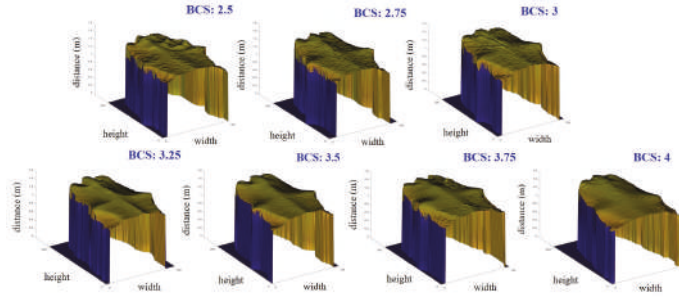


Figure 6. Images composed of cross-sectional slices for ROI 1 used in BCS estimation model 1.

Arithmetic mean height is calculated by following Equation (1):

$$\text{Arithmetic mean height} = \bar{z} = \frac{1}{N} \sum_{i=1}^N z_i \quad (1)$$

where z is the height or distance parameter on the roughness profile, and N is the total number of all height values in ROI 1.

Convex hull volume is calculated by [15]:

$$\text{Convex hull volume} = \frac{1}{3} \times \sum_F (\text{height} \times \text{area of face}) \quad (2)$$

where F represents the faces of the polyhedron.

The difference between peak height and valley depth in fifteen maximums and minimums is calculated by using Equation (3):

$$\text{Difference between peak and valley points} = \frac{1}{15} \sum_{i=1}^{15} z_i - \frac{1}{15} \sum_{j=1}^{15} z_j \quad (3)$$

By using A_1 , A_2 , A_3 , and A_4 features, a stepwise linear regression model ($M1$) is generated by the following Wilkinson notation:

$$M1 \sim 1 + A_3 + A_1 * A_2 + A_2 * A_4 + A_1^2 + A_4^2 \quad (4)$$

where $M1$ is the BCS obtained by proposed method 1.

5.2. BCS Estimation Model 2

To build BCS estimation model 2, ROI 2 in Figure 3a was used, for which an image composed of cross-sectional slices, is shown in Figure 7. In this region, the following features are extracted:

- i. Arithmetic mean height (B_1);
- ii. Difference between peak height and valley depth (B_2).

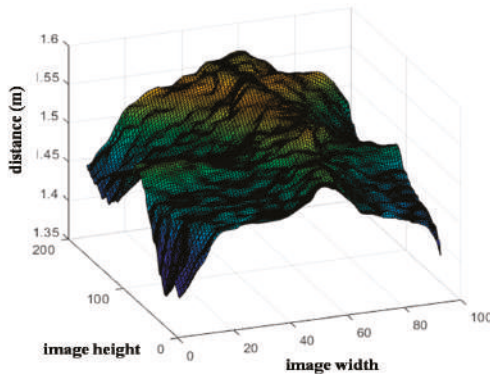


Figure 7. Image composed of cross-sectional slices for ROI 2 used in BCS estimation model 2.

The stepwise linear regression model (M_2) was generated using two learning parameters (B_1 and B_2). The output of the second proposed BCS model is defined using Wilkinson notation, as seen in Equation (5).

$$M_2 \sim 1 + B_1 * B_2 + B_2^2 \tag{5}$$

where M_2 is the BCS obtained by proposed method 2.

Stepwise linear regression is a semi-automated process used for building a model. It can be generated as a way of adding or removing predictor parameters. Parameters or features to be added or removed are picked up from statistics on the test of estimated coefficients used to reach the target output.

In the selected cow image, the BCS estimation model is established after the parameter extraction. The processing time to obtain the BCS output is about 0.13 s. The results for training and testing BCS measurements for the two proposed models are seen in Table 2.

Table 2. Comparison of BCS obtained manually by experts, and BCS obtained by proposed models 1 and 2.

Training with Two Proposed Methods by Regression Analysis				Testing with Two Proposed Methods by Regression Analysis			
Cow No.	BCS by Experts	BCS by Proposed Method (Model 1)	BCS by Proposed Method (Model 2)	Cow No.	BCS by Experts	BCS by Proposed Method (Model 1)	BCS by Proposed Method (Model 2)
1	3	3.39	3.32	1	3	3.29	3.27
2	3.5	3.31	3.35	2	3.25	3.34	3.35
3	3.25	3.35	3.64	3	3.25	3.14	3.29
4	3.25	3.28	3.56	4	3.25	3.39	3.28
5	3.25	3.29	3.30	5	3.25	2.79	3.36
6	3.25	3.54	3.29	6	3.5	3.47	3.53
7	3	3.21	3.12	7	3.25	3.40	3.24
8	3.25	3.20	3.07	8	3.5	3.77	3.36
9	3	3.09	3.34	9	3.5	3.40	3.43
10	3.25	3.10	3.29	10	3.5	3.37	3.31
11	3.5	3.52	3.42	11	3.25	3.28	3.25
12	3.5	3.18	3.06	12	3.5	3.34	3.18
13	3.5	3.59	3.28	13	3.25	3.44	3.28
14	3.25	3.10	3.17	14	3.5	3.27	3.50
15	3.25	3.48	3.21	15	3.75	3.59	3.20
16	3.5	3.38	3.51	16	3.75	3.52	3.53
17	3.25	3.05	3.12	17	3.25	3.25	3.21
18	3.75	3.73	3.53	18	3	3.04	3.16
19	3.25	3.29	3.30	19	3.25	3.41	3.43
20	3.25	3.20	3.40	20	3.25	3.08	3.38
21	3.25	3.40	3.26				
22	3.5	3.45	3.32				
23	3.5	3.48	3.18				
24	3.25	3.30	3.37				
25	3.75	3.67	3.67				
26	3.25	3.11	3.25				
27	2.5	2.62	2.89				
28	3.5	3.32	3.27				
29	2.75	2.88	3.21				
30	3.75	3.41	3.41				
31	4	3.81	3.61				
32	3	3.28	3.26				

6. Performance Evaluation

For automating BCS estimation, we proposed two analytical models, each used for a 3D image of the top view of the region of interest (ROI). The analytical parameters were extracted from pixel depth values. The training models were built using data collected on 32 cows, including one cow for each of the BCS scores of 2.5, 2.75, and 4, four cows for BCS 3, fourteen cows for BCS 3.25, eight cows for BCS 3.5, and three cows for BCS 3.75. In this experiment, training data were collected between BCS 2.5 and 4. A total of 20 cows were used to determine the accuracy of the models, including two cows for BCS 3, ten cows for BCS 3.25, six cows for BCS 3.5, and two cows for BCS 3.75. Manual assessments of BCS were performed by experts, and these assessments were compared with the results of using the proposed models. The measurable parameters were mean absolute error (*MAE*), and mean absolute percentage error (*MAPE*). Performance evaluations for models 1 and 2 are shown in Table 3. According to test results, the mean absolute error percentage for model 2 (*M2*) was less than that for model 1 (*M1*); i.e., small error values indicate good predictive capability. Calculations for *MAE* and *MAPE* were performed using Equations (6) and (7):

$$MAPE = \frac{100\%}{n} \sum \left| \frac{y - y_i}{y} \right| \quad (6)$$

$$MAE = \frac{1}{n} \sum |y - y_i| \quad (7)$$

where n = the number of cows tested, y = BCS by experts, y_i = BCS by the proposed method.

Table 3. Performance evaluation for models 1 and 2.

BCS Model	Training		Testing	
	MAE	MAPE	MAE	MAPE
Model 1 (<i>M1</i>)	0.14	4.31%	0.15	4.64%
Model 2 (<i>M2</i>)	0.19	5.89%	0.13	3.87%

7. Discussion and Conclusions

On large-scale dairy farms, management using manual labor is impractical for numerous reasons. Therefore, automated systems of farm management have been a big focus of dairy farmers. Automated milking robots have recently been introduced to replace manual labor, which is time-intensive and requires one-on-one attention to each cow. The nutritional status of each cow can affect milk production. As one of the most important tools for evaluating nutritional status, BCS is a frequent topic of research. Accurately assessing BCS and regularly monitoring BCS trends have become critical requirements. Our belief is that more and more dairy producers will implement automated BCS evaluation as an important part of smart dairy farming.

The initial step in the proposed system involves automatically selecting images for individual cows. We have tested this process by collecting images in various groups to implement in the advance application. The processing time for this proposed work is acceptable for large-scale data sources. In the next step, automated BCS estimation models are introduced by combining proposed parameter extraction and the two stepwise regression analysis to evaluate BCS. Since our dataset contains only one cow each for BCS of 2.5, 2.75, and 4, we could not test for these BCS in our testing process although they are used in the training for having a good estimation model. Our proposed regression models are tested on 20 cows of BCS (3, 3.25, 3.5, and 3.75). The first model obtains minimum and maximum errors of 0.0025 and 0.45, and the second model obtains minimum and maximum errors of 0.0024 and 0.55, respectively. To measure the proposed model accuracies, the mean absolute parameter (*MAE*) is used and the *MAE* for the first and second models was 0.15 and 0.13, respectively. Although the proposed stepwise regression worked reasonably well for developing useful models in this existing data, it cannot always work well for all new data. Therefore, our future work entails collecting more fruitful data of various BCS for the purpose of discerning variations in our proposed automated BCS evaluation process.

Author Contributions: The major portion of work presented in this paper was carried out by the first author T.T.Z. and P.T.S., supported the experimental work; P.T. and Y.H., provided valuable advice on statistical analysis and animal behavior theory respectively; I.K., cooperated on setting up video cameras in the farm. The first two authors analyzed the experimental results and discussed the preparation and revision of the paper. All authors read and approved the final manuscript.

Funding: This work is supported in part by SCOPE: Strategic Information and Communications R&D Promotion Program (Grant No. 172310006).

Acknowledgments: We would like to give our sincere thanks to Kodai ABE for providing cow image data.

Conflicts of Interest: The authors declare no conflict of interest.

References

1. Kellogg, W. Body Condition Scoring with Dairy Cattle. Available online: <https://www.uaex.edu/publications/pdf/FSA-4008.pdf> (accessed on 2 April 2020).
2. Gearhart, M.A.; Curtis, C.R.; Erb, H.N.; Smith, R.D.; Snien, C.J.; Chase, L.E.; Cooper, M.D. Relationship of changes in condition score to cow health in Holsteins. *J. Dairy Sci.* **1990**, *73*, 3132–3140. [CrossRef]
3. Roche, J.R.; Meier, S.; Heiser, A.; Mitchell, M.D.; Walker, C.G.; Crookenden, M.A.; Riboni, M.V.; Loor, J.J.; Kay, J.K. Effects of precalving body condition score and prepartum feeding level on production, reproduction, and health parameters in pasture-based transition dairy cows. *J. Dairy Sci.* **2015**, *98*, 7164–7182. [CrossRef] [PubMed]
4. Heinrichs, A.J. *Body-Condition Scoring as a Tool for Dairy Herd Management*; Cooperative Extension, College of Agriculture, Pennsylvania State University: University Park, PA, USA, 1980; Volume 363.
5. Rossi, J.; Wilson, T.W. Body Condition Scoring Beef Cows. Available online: https://secure.caes.uga.edu/extension/publications/files/pdf/B%201308_3.PDF (accessed on 23 April 2020).
6. Bewley, J.M.; Peacock, A.M.; Lewis, O.; Boyce, R.E.; Roberts, D.J.; Coffey, M.P.; Kenyon, S.J.; Schutz, M.M. Potential for Estimation of Body Condition Scores in Dairy Cattle from Digital Images. *J. Dairy Sci.* **2008**, *91*, 3439–3453. [CrossRef] [PubMed]
7. Alapati, A.; Kapa, S.R.; Jeepalyam, S.; Rangappa, S.M.P.; Yemireddy, K.R. Development of the body condition score system in Murrah buffaloes: Validation through ultrasonic assessment of body fat reserves. *J. Dairy Sci.* **2010**, *11*, 1–8. [CrossRef] [PubMed]
8. Edmonson, A.J.; Lean, I.J.; Weaver, L.D.; Farver, T.; Webster, G. A body condition scoring chart for Holstein dairy cows. *J. Dairy Sci.* **1989**, *72*, 68–78. [CrossRef]
9. Spoliansky, R.; Edan, Y.; Parmet, Y.; Halachmi, I. Development of automatic body condition scoring using a low-cost 3-dimensional Kinect camera. *J. Dairy Sci.* **2016**, *99*, 7714–7725. [CrossRef] [PubMed]
10. Song, X.; Bokkers, E.A.M.; van Mourik, S.; Koerkamp, P.G.; van der Tol, P.P.J. Automated body condition scoring of dairy cows using 3-dimensional feature extraction from multiple body regions. *J. Dairy Sci.* **2019**, *102*, 4294–4308. [CrossRef] [PubMed]
11. Imamura, S.; Zin, T.T.; Kobayashi, I.; Horii, Y. Automatic evaluation of cow's body-condition-score using 3D camera. In Proceedings of the 2017 IEEE 6th Global Conference on Consumer Electronics (GCCE), Nagoya, Japan, 24–27 October 2017; pp. 1–2.
12. Krukowski, M. Automatic Determination of Body Condition Score of Dairy Cows from 3D Images. Available online: <https://pdfs.semanticscholar.org/a9e1/bddb0fdc862859b90d03e20b34d4cfd4b93.pdf> (accessed on 23 April 2020).
13. Zin, T.T.; Seint, P.T.; Tin, P.; Horii, Y. The Body Condition Score Indicators for Dairy Cows Using 3D Camera. In Proceedings of the International Workshop on Frontiers of Computer Vision (IW-FCV), Ibusuki, Japan, 20–22 February 2020; pp. 1–8.
14. Hansen, M.F.; Smith, M.L.; Smith, L.N.; Jabbar, K.A.; Forbes, D. Automated monitoring of dairy cow body condition, mobility and weight using a single 3D video capture device. *Comput. Ind.* **2018**, *98*, 14–22. [CrossRef] [PubMed]
15. Polyhedron. Available online: <https://en.wikipedia.org/wiki/Polyhedron> (accessed on 20 April 2020).



© 2020 by the authors. Licensee MDPI, Basel, Switzerland. This article is an open access article distributed under the terms and conditions of the Creative Commons Attribution (CC BY) license (<http://creativecommons.org/licenses/by/4.0/>).

Article

Wireless Module for Nondestructive Testing/Structural Health Monitoring Applications Based on Solitary Waves

Ritesh Misra ¹, Hoda Jalali ², Samuel J. Dickerson ¹ and Piervincenzo Rizzo ^{2,*}

¹ Mixed-Signal Multi-Domain Systems Laboratory, Department of Electrical and Computer Engineering, University of Pittsburgh, 3700 O'Hara Street, 1206 Benedum Hall, Pittsburgh, PA 15261, USA; rim39@pitt.edu (R.M.); dickerson@pitt.edu (S.J.D.)

² Laboratory for Nondestructive Evaluation and Structural Health Monitoring Studies, Department of Civil and Environmental Engineering, University of Pittsburgh, 3700 O'Hara Street, 729 Benedum Hall, Pittsburgh, PA 15261, USA; HOJ14@pitt.edu

* Correspondence: pir3@pitt.edu; Tel.: +1-412-624-9575; Fax: +1-412-624-0135

Received: 12 May 2020; Accepted: 24 May 2020; Published: 26 May 2020

Abstract: In recent years, there has been an increasing interest in the use of highly nonlinear solitary waves (HNSWs) for nondestructive evaluation and structural health monitoring applications. HNSWs are mechanical waves that can form and travel in highly nonlinear systems, such as granular particles in Hertzian contact. The easiest setup consists of a built-in transducer in drypoint contact with the structure or material to be inspected/monitored. The transducer is made of a monophasic array of spherical particles that enables the excitation and detection of the solitary waves. The transducer is wired to a data acquisition system that controls the functionality of the transducer and stores the time series for post-processing. In this paper, the design and testing of a wireless unit that enables the remote control of a transducer without the need to connect it to sophisticated test equipment are presented. Comparative tests and analyses between the measurements obtained with the newly designed wireless unit and the conventional wired configuration are provided. The results are corroborated by an analytical model that predicts the dynamic interaction between solitary waves and materials with different modulus. The advantages and limitations of the proposed wireless platform are given along with some suggestions for future developments.

Keywords: highly nonlinear solitary waves; nondestructive evaluation; wireless sensing; Bluetooth technology

1. Introduction

Highly nonlinear solitary waves (HNSWs) are mechanical waves that can form and travel in highly nonlinear systems such as mono-periodic arrays of elastically interacting spherical particles, sometimes indicated as granular crystals [1–18]. One of the key features of HNSWs is that properties like duration, amplitude, and speed can be tuned without electronic equipment by simply adding static precompression on the array or varying the particles' material and geometry. This tunability makes the use of HNSWs appealing in some engineering applications such as nondestructive testing (NDE), structural health monitoring (SHM) [19–22] or acoustics [23–28].

The scheme of an HNSW-based NDE/SHM is shown in Figure 1. One end of an array of identical spheres is in dry contact with the structure to be inspected/monitored. The top particle of the chain is lifted and released to create a mechanical impact that triggers the formation of a solitary wave, hereinafter referred to as the incident solitary wave (ISW). When the mass of the striker is equal to the mass of the other particles composing the chain, a single pulse is generated. The ISW propagates

through the array, is detected by a sensing system embedded in the chain, and then reaches the surface of the structure to be inspected/monitored. At the the interface between the chain and the structure, most of the acoustic energy carried by the ISW is reflected back, giving rise to one or two reflected solitary waves, typically referred to as the primary and the secondary reflected solitary waves (PSW and SSW). These reflected waves are then detected by the same sensing system embedded in the array.

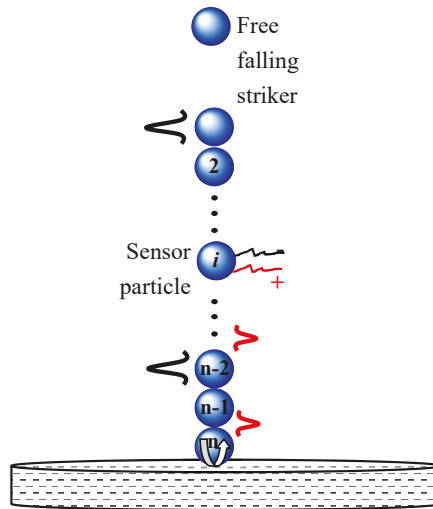


Figure 1. General scheme of nondestructive evaluation/structural health monitoring paradigm using highly nonlinear with different modulus. The advantages and limitations of the proposed wireless platform are given along with some suggestions for future developments.

Many researchers proved that the amplitude and the arrival time of the reflected solitary waves depend on key properties of the adjacent structure/material [19–22,29–38]. For example, Yang et al. studied numerically, analytically, and experimentally the reflection of HSNWs at the interface of a large thin plate, and found that the amplitude and the arrival time of the reflected waves are affected by the plate thickness, the particles size, and the boundary conditions at a critical distance from the plate edges [39]. Kim et al. indicated experimentally and numerically that solitary waves can be used to detect delamination in carbon fiber reinforced polymer plates [31]. A numerical study on the interaction of HNSWs with composite beams showed that solitary waves are helpful to evaluate the directional elastic parameters of the composites [40]. Others reported that the method is effective at detecting subsurface voids [38], assessing the quality of adhesive joints [22,30], composites [31,34,40,41], orthopedic and dental implants [32,42], and at measuring internal pressure [43–46] and axial stress [47,48].

In all the studies cited above, the array of particles is coaxially wired to electronic equipment that controlled the striker and digitized the time-waveforms for post-processing analysis. Although this is acceptable for periodic inspections, i.e., NDE applications, it may be detrimental when continuous monitoring, i.e., SHM protocol, is preferred or necessary. SHM systems, however, can become expensive in large structures or high-dense sensor systems due in part to cabling networks. SHM using wireless sensors can overcome the limitations of traditional wired methods with many attractive advantages such as wireless communication, onboard computing, battery power, ease of installation, and so on. Platforms for SHM containing wireless smart sensing (WSS) have been developed during the past years. WSSs are devices that have a sensor, microprocessor, radio frequency transceiver, memory, and power source integrated into one small size unit and are characterized by their capabilities of sensing, computation, data transmission, and storage, all achieved by a single device. WSS represents an attractive alternative to their wired counterparts because of the lower cost achieved by

removing the need for cables (including cost labor reduction), and by the widespread production of micro-electro-mechanical sensors. The wireless communication capability allows flexible network topology and hence enables a decentralized monitoring scheme, which adds robustness to the SHM system compared with the centralized approach in wired systems [49]. For these reasons, in the last two decades there has been a great deal of research and development of wireless sensors for SHM applications that were summarized in a few excellent reviews [50–53]. However, as the NDE/SHM method based on HNSW has been developed only recently, there is no wireless sensing technology available in support of nonlinear solitary wave propagation and detection.

To fill this gap, a wireless sensor system to support the generation and detection of HNSWs for NDE or SHM applications was designed, assembled, and tested. The system is not a sensor per se, but rather an autonomous data acquisition node to which a traditional HNSW transducer, designed and developed in our lab, can be attached. The new device can be best viewed as a platform in which mobile computing and wireless communication elements converge with the transducer. This capability is particularly advantageous in the context of SHM, in which several HNSW transducers can be deployed on the structure of interest to perform structure interrogation and remote communication to a remote repository. Other advantages of this newly designed system are cost reduction in the installation phase, autonomous data processing, denser sensing capability in large structural systems, just to mention a few.

The paper is organized as follows: Section 2 provides an overview of the designed wireless platform and is divided into sub-sections that describe the single components. Section 3 presents the experimental results in which the wireless platform is compared to the performance of conventional sensing with the use of a data acquisition system. Section 4 supplements the experimental finding with the outcomes of a numerical analysis that models the dynamic interaction of the solitary waves with different materials. Lastly, Section 5 provides some concluding analyses and remarks about the study presented here.

2. Wireless HNSW Sensor System Overview

The new wireless sensor network is comprised by three components, the HNSW transducer, a custom printed circuit board (PCB), and a mobile computing device. A schematic of the overall platform is shown in Figure 2.

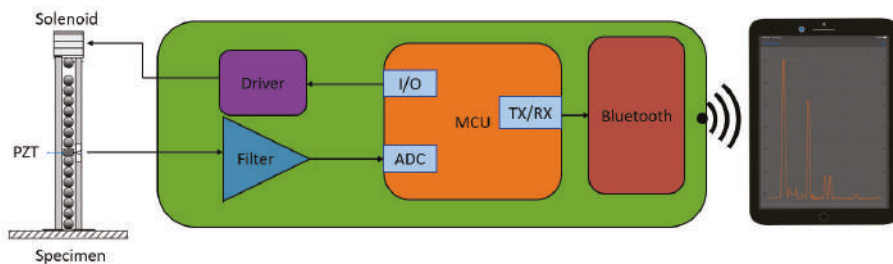


Figure 2. Schematics of the overall HNSW wireless sensor node. The “specimen” in the figure represents any material/structure to be monitored using the solitary waves.

2.1. HNSW Transducer: Conventional Design

The HNSW transducer, hereinafter simply referred to as the *transducer*, contains eight 19.05 mm spheres, a commercial electromagnet (Uxcell 12 V DC) able to lift and release the striker, a sensor, and a frame. All the particles except the striker were made of a non-ferromagnetic material. The current flowing through the solenoid generates a magnetic field strong enough to lift the first particle of the array, whereas flow interruption causes the striker to impact the chain and generate the ISW. The sensing system consists of a lead zirconate titanate ($\text{Pb}[\text{Zr}_x\text{Ti}_{1-x}]\text{O}_3$) wafer transducer (PZT),

embedded between two 6.05 mm thick, 19.05 mm diameter disks. Kapton tape insulated the PZT from the metal. In the conventional (wired) configuration, the transducer is connected to and driven by a National Instruments PXI running in LabVIEW using a graphical user interface created ad hoc for the experiments. The hardware generates the signal to open/close the electrical current to feed the solenoid, while the user interface allows for the selection of the repetition rate of the striker (by controlling the output signal), the number of measurements, the sampling frequency of the digitized waveforms, and the storage of the waveforms for post-processing analysis. The *transducers* used in this study were also successfully used elsewhere [19,43–45,54] and were, therefore, the starting point to develop the proposed wireless platform. However, it is emphasized here that the proposed platform can be adopted and adapted to a chain of any size, length, and particle materials.

2.2. Circuit Board

In the proposed wireless sensor node, the role of the data acquisition system used in the conventional configuration is replaced by a PCB, which is the centerpiece of the schematics of Figure 2. The PCB includes the driver to provide the current for the solenoid, a filter to remove white noise and provide anti-aliasing, and a protocol for the remote communication to and from mobile devices.

Figure 3 shows a photo of the PCB with color-coded sections corresponding to the individual components. The driver allows the microcontroller (MCU) to deliver the DC current to the solenoid with an input/output (I/O) pin on-demand (GPIO). Although the term “GPIO” suggests that both an output and an input are necessary to interface with the driver, the latter is designed such that the movement of the striker onto the array can be controlled through a single digital output. The waves, sensed by the PZT, are filtered by an analog filter and subsequently sampled by the analog to digital converter (ADC) within the MCU. The MCU then sends the data samples to an integrated circuit (IC) enabled for Bluetooth Low Energy (BLE) communication using the Universal Asynchronous Receiver/Transmitter (UART) protocol. The protocol allows for the transmission of the data to any mobile device capable of BLE communication.

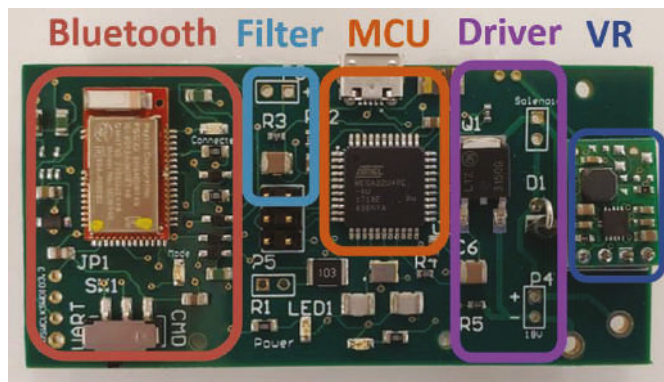


Figure 3. Photo of the final printed circuit board (PCB), which includes a Bluetooth transceiver, filter, microcontroller (MCU), transducer driver, and a voltage regulator (VR). The board is 76.2 mm wide and 36.8 mm high.

The final PCB ($76.2 \times 36.8 \text{ mm}^2$) was designed to optimize space and therefore enhance portability. The MCU was an ATmega32u4 with 32 kB of flash memory for storing embedded programs, 2 kB of SRAM for storing measurement data, all of the peripherals required to induce and measure the signal, and libraries that allowed for easy communication with the Bluefruit LE module. The MCU has also its own USB controller, making local data collection possible without adding an IC to do FTDI to UART conversion. Overall, the created design fares better than the conventional design because the

new system is more compact, is dedicated to the specific application with HNSWs, and can be driven by smart devices such as tablets or even smartphones.

2.3. Actuation: Wireless Configuration

In the wired configuration, the DC current used to drive the electromagnet is delivered by a power supply external to or embedded to a data acquisition system. In the proposed wireless node, the DC current is provided by the PCB. Following the protocol implemented in the PXI in previous studies [19,43–45,54], the solenoid is energized for 250 ms, an interval sufficiently long to lift the striker until it touches the electromagnet before falling freely onto the array. The energy necessary to deliver the current necessary to operate the electromagnet is significant with respect to the other electronic components and is directly proportional to the weight and the falling height of the striker. To supply the necessary energy, a custom power source for the solenoid and driver circuit was chosen to allow the control of the striker while maintaining portability. A 14.8 V rechargeable LiPo battery with a maximum discharge rate of 47 A and a capacity of 1050 mAh was chosen. For the 250 ms interval, 675 mA is consumed. In future, the duration and/or the energy consumption can be reduced by shortening the falling height of the striker, by making the striker lighter (in order to be able to use smaller solenoids), or by minimizing the friction between the striker and the inner wall of the guide.

Under this design, the battery can continuously drive the striker for 93 minutes, which means that the battery can theoretically power $22,390 = (93 \times 60 \times 4)$ impacts. This value was obtained by multiplying the capacity of the battery by the inverse of the current consumption. The number of strikes can be also increased using a battery with higher capacity within the limit of size and weight constraints necessary to make the whole node practical. In the present study, the 1050 mAh battery was chosen because it was sufficient to complete a full round of experiments (see Section 3).

Figure 4 shows the control circuit for the actuation. A 1N4003 diode was added in parallel to the solenoid; this flyback diode prevents voltage spike that results from turning off the solenoid from damaging the metal–oxide–semiconductor field-effect transistor (MOSFET), which would, in turn, shorten the life of the overall system [55]. The MOSFET itself acts as an open circuit if the GPIO pin is off, and acts as a closed circuit if the GPIO pin is on, allowing for the control of the current through the solenoid via software. The MOSFET NTD3055-150 from ON Semiconductor was chosen. According to the manufacturer, this specific MOSFET is designed for low voltage, high-speed switching applications in power supplies, converters and power motor controls and bridge circuits, and dissipates 28.8 W continuously, which provides a threefold factor of safety compared to the 9.45W ($14 \text{ V} \times 0.675 \text{ A}$) required to lift the striker. The calculation for the required wattage was based on experiments done with a power supply that justified the choice of a 14.8 V battery in the first place. An RC circuit at the gate of the transistor provides a slight delay between turning the GPIO pin off in software and the moment at which the magnetic ball on top of the chain drops. The specific resistor and capacitor values used are not critical, what is most important is that the time constant of the RC circuit is three times larger than the minimum delay that the MCU can produce. This prevents the worst-case scenario of the MCU sampling the ADC after the incident waves passed the sensor disk. The delay that the RC circuit introduces safeguards against mechanical adjustments to the transducer that can reduce the amount of time it takes for the striker to fall. The RC circuit consisted of a 10 k Ω resistor and a 33 nF capacitor, resulting in a time constant of 333 μs .

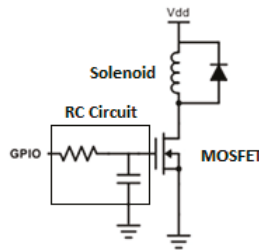


Figure 4. Schematic of the control circuit used to drive the direct current through the solenoid. V_{dd} represents the 14.8 V power source while the coil directly below V_{dd} represents the electromagnet used to lift the topmost ball.

2.4. Filter Design

A passive low-pass filter was added to remove white noise and provide anti-aliasing. The cutoff frequency was determined by examining the frequency spectrum of solitary waves recorded conventionally at a sampling rate of 2 MHz by placing a *transducer* above a 12.7 mm thick steel plate. Figure 5 shows one of the time waveforms and the corresponding Fourier transform associated with this control test. The 99% bandwidth of this signal (the frequency range across which 99% of the power in the signal is contained) is 13.93 kHz. Our initial approach was to place the cutoff frequency somewhere between 50 and 100 kHz so as to eliminate white noise and also have at least a 4x factor of safety from losing any important information. This would also have served to provide anti-aliasing. However, setting the cutoff frequency to a point within that range would introduce a significant amount of phase lag in the relevant frequencies, which could distort the measurements of the arrival time of the pulses of interest. The phase response of a filter is the radiant phase shift added to the phase of each sinusoidal component of the input signal, and the term “phase lag” is used when these phase shifts cause delays in time. In the case that the primary wave and secondary wave have the exact same frequency content, both waves would experience the same amount of delay. However, if the reflected waves are different in terms of the frequency content, a narrow low-pass filter may cause artifacts. Based on the above, a cutoff frequency of 2.4 MHz was chosen in order to minimize the phase lag across the frequencies with relevant information.

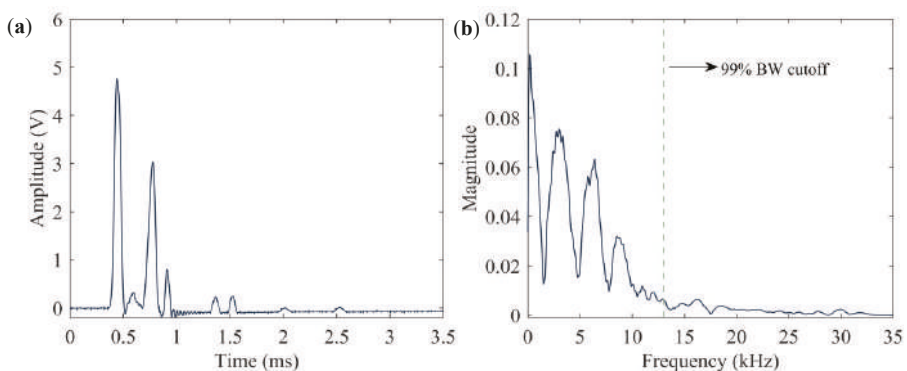


Figure 5. (a) Time waveform and (b) corresponding Fast-Fourier transform (FFT) measured during a control test to design a low-pass filter.

Figure 6 compares two cutoff frequencies, namely 100 kHz and 2.4 MHz, and their effects on the phase response of the low pass filter. The phase lag in the 10–100 kHz range associated with the 2.4 MHz cutoff is essentially flat. At 50 kHz, the phase lag is 0.2 degrees which corresponds to a 0.01

μs delay, well below the sampling period typically used in HNSW tests. However, for the cutoff at 100 kHz, the phase lag at 50 kHz is equal to 4.8 degrees, which yields a 0.26 μs delay. A delay of 0.26 μs is negligible at a sampling period of 13.3 μs , which is the sampling period of the current design. However, as discussed within Section 6, we plan on increasing the sampling frequency in future iterations of this circuit board to at least 1 MHz. In that context, the usage of a lower cutoff frequency could distort the HNSW measurements. The components of the filter's final design have values equal to 2 Ω and 33 nF, resulting in a cutoff frequency of 2.411 MHz. It is noted here that the design of the filter can be modified based upon the specific application of the transducers as the characteristics of the particles in the array and/or the properties of the structure to be monitored, modify the duration of the incident and reflected waves.

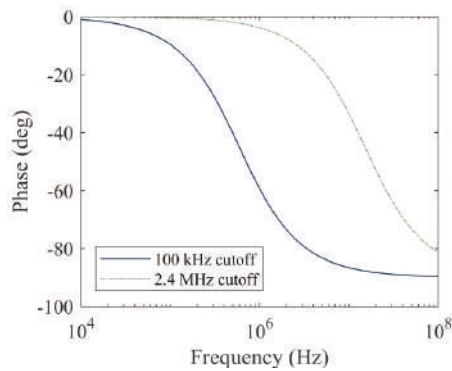


Figure 6. Phase lag as a function of frequency, induced by low pass filters with cutoffs at 100 kHz and 2.4 MHz.

2.5. Wireless Communication

Bluetooth technology was chosen as the communication protocol between the newly proposed wireless device and laptops, tablets, or phones. For short-distance communication, Bluetooth technology is appealing owing to its compatibility with the majority of smartphones, tablets, and laptops. Additionally, Bluetooth communication does not rely on any external network. The Bluetooth LE UART module we used relies on the general-purpose, ultra-low power System-on-Chip nrF51822 to provide wireless communication with any BLE-compatible device. The term “System-on-Chip” means that the nrF51822 is a complete computer system within a single chip that can act independently from the MCU. This could be essential for improvements to future iterations of the PCB as discussed in the Discussion and Conclusions section. The nrF51822 has the ability to choose between UART and SPI communication with external devices, and sleep modes for power preservation. According to the manufacturer, the range of the module is approximately 60 m in an indoor environment, assuming a lack of obstacles. The module was flashed with the firmware provided by the manufacturer [56].

2.6. Mobile Application

An app (Figure 7) was designed to communicate with the *transducer* via the PCB from a smart device. The app was adapted from a general app framework provided by the manufacturer [57]. The custom adaptation added a data streaming mode capable of compartmenting the data it received from different runs into separate graphs. These plots can also be exported as data files for further processing. The data streaming was designed to work with the messaging protocol programmed into the MCU, as discussed later in Section 2.7. First, the app provides a list of Bluetooth devices within the vicinity. After the user selects the appropriate device (Figure 7a), the “Data Stream” menu option allows the user to remotely drive the striker and collect data from the embedded sensor disk (Figure 7b). As shown in Figure 7c, selecting “Data Stream” prompts the user to select the number

of strikes and the length (data points) of the signal. Once the PCB receives the command, it actuates the *transducer*, collects samples of the time waveform from the ADC, sends the data to the mobile device, and iterates the process as many times as the number of strikes chosen by the user. During the process, the waveforms are displayed in real-time on the smart device (Figure 7d). The app and the PCB together make a self-contained system that only requires a basic knowledge of smart mobile devices to operate.

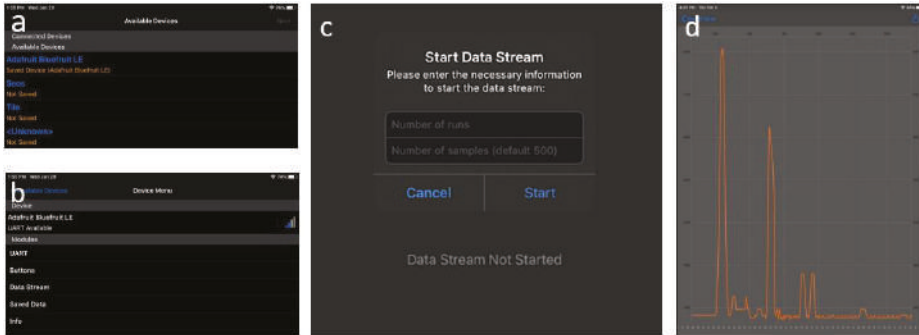


Figure 7. Screenshots of the custom application for mobile devices such as tablets and phones. (a) Panel to select the appropriate module from a list of devices. (b) Panel to select a data stream from a device menu. (c) Panel to enable the user to select the desired number of samples and runs. (d) Display of a single measurement from a sheet of aluminum plotted on the mobile device.

2.7. Implementation

The ADC within the AtMega32u4 was used to digitize the signals detected by the embedded sensor disk. The ADC clock was set equal to 1 MHz, as setting the clock to a higher frequency would reduce the resolution for this particular device. A single conversion takes 13 clock cycles, and the clock frequency was set to 16 MHz, so the highest sampling frequency we could theoretically achieve was $1 \text{ (MHz)}/13 = 77 \text{ kHz}$. The ADC uses a sample-hold capacitor, which is first charged by the signal and then closed-off from the input signal so that the voltage of the signal at that time can be indirectly read through the voltage on the capacitor at that moment. A 5 V power supply for the ATMega32u4 and the Bluetooth module was generated with a 3.7 V single-cell LiPo and a Pololu 5 V Step-Up Voltage Regulator U1V11F5. The U1V11F5 can handle input voltages in a range of 1 to 5.5 V, so it is robust to small voltage drops caused by the discharging of the single-cell LiPo. The PCB follows a protocol for collecting data and sending it to a mobile app. After the first time the PCB is turned on, it waits for a mobile device to connect to it. After a device has connected, the PCB turns the solenoid on and off again, starts a timer, and then collects ADC samples until the ADC reading passes a certain threshold. This allows it to learn the timing between it dropping the ball and observing a HNSW. It then allows the app to send it the desired number of samples and runs and then executes the appropriate number of runs while recording the desired number of samples in time for each run.

Figure 8 shows the final prototype used in the experiments presented in the next section. The PCB is connected to both batteries it needs for all of its functionalities and is in a state where it could be connected to any Bluetooth-compatible mobile device.

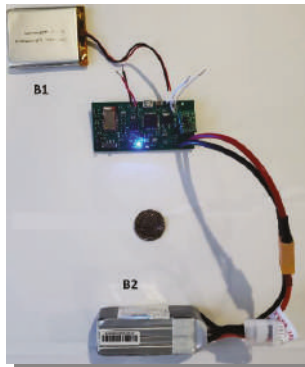


Figure 8. Photo of the final PCB with two batteries, B1 and B2. The 3.7 V battery (B1) powers the microcontroller and Bluetooth module. The 14.8 V battery (B2) powers the solenoid.

3. Experimental Setup and Procedure

To compare the performance of the proposed wireless module to a conventional configuration, two identical *transducers* like those illustrated in Section 2.1 were used. Figure 9 shows part of the setup. *Transducer* T1 was wired to the PCB whereas *transducer* T2 was cabled to a National Instruments —PXI. The latter controlled an external DC power supply to energize the electromagnet.

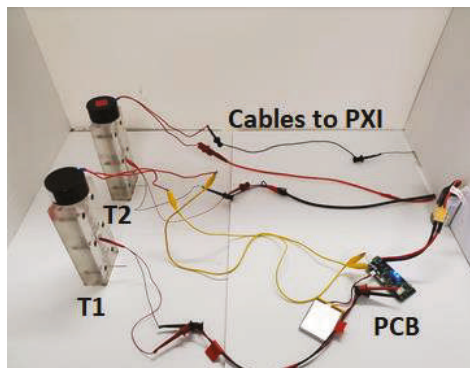


Figure 9. Photo of the two identical *transducers* used in this study. *Transducer* T1 was wired to the PCB. *Transducer* T2 was wired to a National Instruments PXI.

Three sets of experiments were conducted. In the first two, both *transducers* were placed above a steel thick plate and then above a foam board. The latter was laying above an optical table. Then, one *transducer* only was placed above a granite block and connected to the wireless node first and then to the PXI. The steel specimen was $304.8 \times 152.4 \times 76.2 \text{ mm}^3$, the foam board was $604.5 \times 457.2 \times 6.35 \text{ mm}^3$, and the granite block was $152.4 \times 152.4 \times 304.8 \text{ mm}^3$. For each experiment, 100 impacts were triggered in order to collect a statistically significant amount of data. For the steel plate, one *transducer* at the time was placed at the center of the $304.8 \times 152.4 \text{ mm}^2$ area. For the foam test, the two *transducers* were placed symmetrically, 101.6 mm away from the center of the board and 228.6 mm from the sides in order to secure identical boundary conditions. The three materials were chosen as representatives of different Young moduli. For the steel plate test, the sampling frequency was equal to 61 kHz and then raised to 75 kHz for the other two tests for both the wireless node and the PXI. Based on the discussion of Section 2.4, when the sampling frequency was 61 kHz, the filter used a 51Ω resistor and a 330 nF

capacitor, whereas when the sampling frequency was 75 kHz, a 2 Ω resistor and a 330 nF capacitor were used.

4. Experimental Results

4.1. Steel Plate: Control Test

The first round of experiments was conducted on the thick steel plate and served as a control test to troubleshoot any possible problems associated with the wireless module. Figure 10 shows one of the time waveforms collected by *transducer* T1. The first peak is the ISW whereas the second peak around 550 μ sec is the PSW. Both the ISW and the PSW were tailed by small humps. The origin of these small pulses is described in Section 5. It is anticipated here that these pulses are not detrimental to the successful implementation of NDE/SHM strategies with HNSWs. As conventionally done in HNSW-based NDE/SHM, the time-of-flight (ToF) of the PSW was calculated, as the difference between the arrival time of the PSW with respect to the ISW at the sensing disk. This wave feature is significant for NDE-based or SHM-based applications, as it has been demonstrated that the ToF is sensitive to the presence of damage and/or variation in local stiffness, etc.

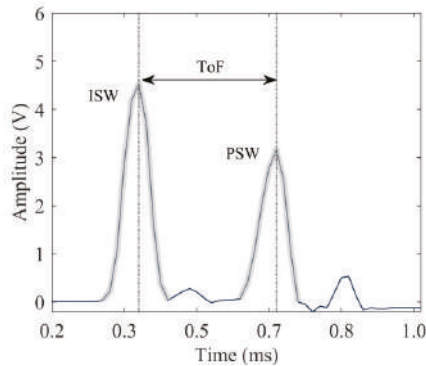


Figure 10. Steel plate test. Example of one of the hundred-time waveforms recorded during the experiment.

To compare the results from both the wired and the wireless systems, the time-series obtained by averaging the one hundred waveforms from both (wired and wireless) systems are displayed in Figure 11a. As the trigger for the two systems was different, the graphs in Figure 11a were shifted horizontally in order to overlap the arrival time of the ISW. Figure 11a proves that the two time-waveforms are remarkably similar to each other, in terms of pulse amplitude and corresponding ToF. The slight differences can be attributable to manual *transducer-to-transducer* differences associated with fabrication and assembly. To identify differences at each measurement, Figure 11b shows the number of occurrences for a given ToF for both setups. Three values, namely 295, 311, and 328 μ s were measured. It is noted here that the width of each bar is equal to the sampling period, which, for the steel plate test, was equal to 16.4 μ s.

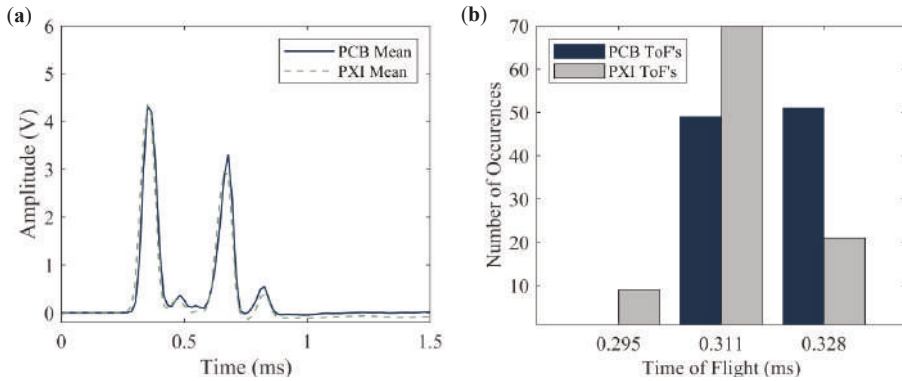


Figure 11. Steel plate test. (a) Time-series obtained by averaging the 100-time waveforms measured with the sensor disks. (b) Number of occurrences of a given ToF. For each color, the total number of occurrences is 100.

4.2. Foam Specimen

Similar to Figures 11 and 12 presents the results associated with the foam board that was probed with both *transducers* acting sequentially. For this material, the amplitude of the ISW measured with the PXI is larger than the corresponding amplitude measured with the wireless platform. This trend confirms what seen in Figure 11a but for the latter case the difference was smaller. The origin of such difference is discussed in Section 4.3. Nonetheless, it is important to emphasize that for NDE/SHM applications, the trends of interests are those associated with variations from baseline data when material degradation or damage occurs. As such any *transducer* to *transducer* difference in the amplitude of the ISW is not detrimental to prove the main hypothesis of the present research, i.e., that the wireless platform can be used for HNSW measurements in lieu of sophisticated electronics. Another distinctive feature of the wireless platform is that it was able to detect a twin peak associated with the dynamic interaction of the waves with the foam. The origin of these twin-peaks, originally identified and detailed in [58] and elaborated further in [43], was found in several HNSW-based NDE related to soft materials including rubber [44]. For the sake of completeness, the dynamic interaction among the particles that induce the “twin-peaks” is discussed in Section 5.

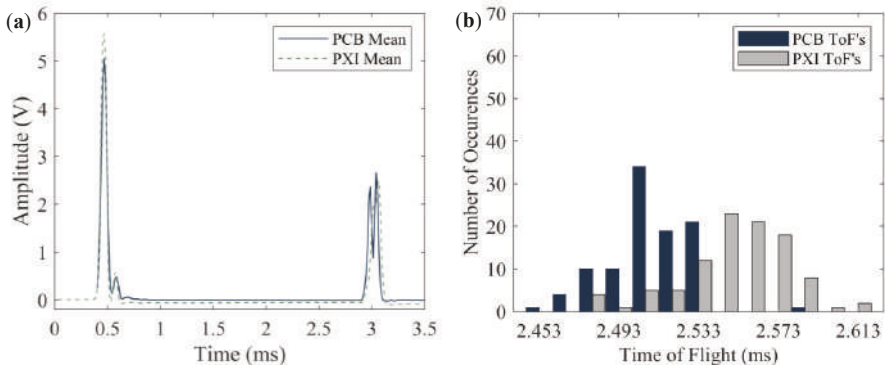


Figure 12. Foam board test. (a) time-series obtained by averaging the 100-time waveforms measured with the sensor disks. (b) Number of occurrences of a given ToF. For each color, the total number of occurrences is 100.

Figure 12b shows that the number of occurrences of the ToF is more spread with respect to the steel test. This is attributable to the soft nature of the foam specimen. Additionally, the occurrences of the ToF measured with the wireless platform are skewed to the left, i.e., the PSW traveling along *transducer* T1 seems faster than in *transducer* T2. While the origin of such skew is not clear, and more insights could have been gained by inverting the terminals of the *transducers*, it is believed that what was observed is more related to the dynamic interaction of the waves with the foam rather than a variability associated with the *transducers*. In the future, the experiments will be repeated by connecting the terminals of the solenoid and the sensor disk to the PCB first and then to the PXI.

4.3. Granite Specimen

To investigate the origin of the small discrepancies observed for the foam board, one transducer only was used above the granite block and connected to the PCB first and then to the PXI. The results are presented in Figure 13. The time-waveforms (Figure 13a) confirms the trend observed for the foam (Figure 12a). The amplitude of the ISW measured with the PXI is about 20% higher than the corresponding amplitude measured with the wireless node. As such, it can be concluded that differences in the impedance between the two devices result in differences in the amplitude of the detected incident wave. Figure 13b shows the number of occurrences associated with the granite test. The distribution of the ToF is in between the foam and the steel specimen. This confirms that the scattering of the results (i.e., the number of histograms plotted in each figure) is related to Young's modulus of the material. Contrary to what is observed in Figure 12b or Figure 13b shows that the ToF measured with the PCB is higher than the ToF measured with the PXI.

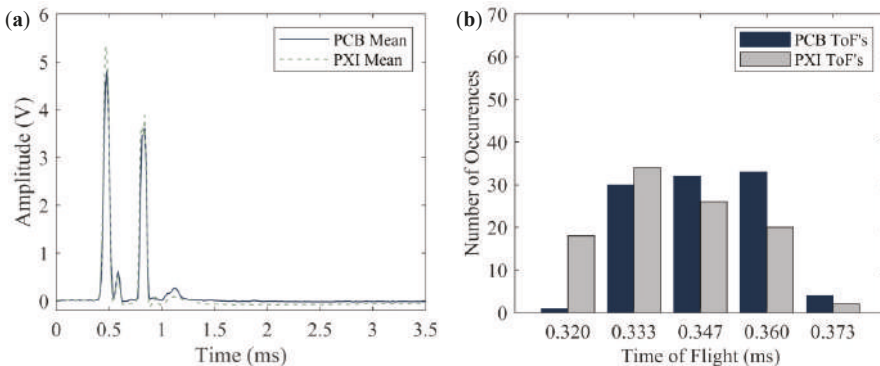


Figure 13. Granite test. (a) time-series obtained by averaging the 100-time waveforms measured with the sensor disks. (b) Number of occurrences of a given ToF. For each color, the total number of occurrences is 100.

5. Numerical Results

To interpret the experimental results presented in Section 4, an analytical study was performed about the dynamic interaction of solitary waves with the test specimens, using a model that simulates the propagation of solitary waves along the granular array using a series of point masses interacting via nonlinear Hertzian contact forces (Figure 14). Furthermore, the test specimen in contact with the granular chain was modeled as a linear elastic media using a finite element model. The two models were integrated at the interaction point between the granular chain and the test specimen based on the Hertzian contact law. Owing to the scope of this paper, the numerical formulation and the analytical equations used for the simulation are not presented here and interested readers are referred to [27,43–48,54] in order to gain more insight on the subject.

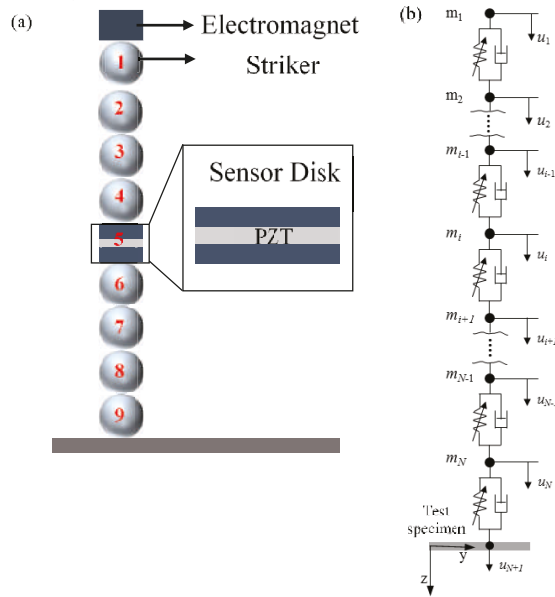


Figure 14. Modeling the interaction between the granular chain and the test specimen. (a) Schematics of the HNSW transducer with particle site number. (b) Schematic of the mono-periodic array as a series of point masses interacting via nonlinear Hertzian contact (In this figure, $N = 9$).

For the models, the properties listed in Table 1 were used for the three materials, namely steel, granite, and foam considered in this study.

Table 1. Mechanical properties, specimen thickness, and the predicted ToFs of the steel, granite, and foam specimens in the numerical study.

Material	Material Properties			Specimen Thickness (mm)	Numerical Time of Flight (ms)
	Density (kg/m ³)	Modulus of Elasticity (GPa)	Poisson's Ratio		
Steel	7800	200	0.3	6.35	0.333
Granite	2700	70	0.25	304.8	0.359
Foam	60	0.03	0.3	6.35	2.494

Figure 15 shows the amplitude of the dynamic force measured at the sensor disk (site #5 in Figure 14a). The waveforms represent the average interaction force between the sensor particle and the adjacent particles (sites #4 and #6). As observed in the experiments (Figure 11a, Figure 12a or Figure 13a), Figure 15 shows that the ISW (highlighted in light blue background) is trailed by a small pulse emphasized with red circles. This pulse is the result of a rebound between the sensor disk and particle #6, caused by the local increase of contact stiffness between the disk and the sphere. The higher (with respect to the contact between two spheres) contact stiffness at the sensor particle results in the increase of its maximum particle velocity. As the ISW passes through the sensor and arrives at bead #6, the disk and the particle #6 separate. This yields a momentary zero interaction force at the sensor particle (Figure 15). Then, owing to its higher momentum, the sensor particle strikes particle #6 again, yielding to the small hump circled in Figure 15. The same mechanism causes the small pulses trailing the PSW in the steel and granite tests.

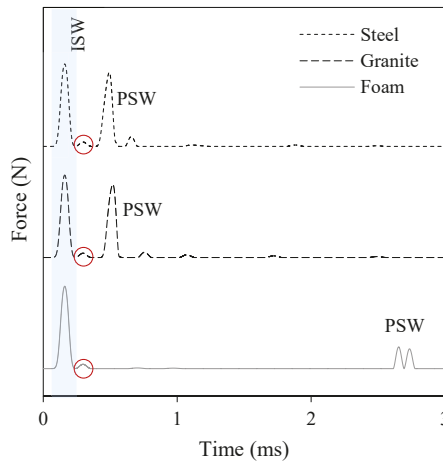


Figure 15. Solitary wave force profiles obtained from the numerical modeling of the interaction of solitary waves and steel, granite, and foam specimens.

When the *transducer* was used above the foam board, both the experimental (Figure 12a) and the numerical (Figure 15) results show a twin PSW. Owing to its soft nature, the acoustic energy carried by the ISW causes a relatively large deformation chain/foam interface. This deformation induces separation between particles that are much larger than the separation that occurs when the chain is above stiff materials. When the reflected wave propagates back to the chain, the separation between bead #6 and the sensor particle and the separation of the sensor particle and bead #4 is large enough that two distinct impacts, i.e., peaks, are seen. The first peak is therefore the upward impact of particle #6 onto the sensor disk, and the second peak is the upward impact of the disk onto particle #4.

Figure 15 also confirms what was observed experimentally (Figure 11b, Figure 12b, or Figure 13b) about the ToF that is inversely proportional to the stiffness of the interface material. The results of the numerical study are summarized in Table 1. The numerical ToF predictions are in very good agreement with the experimental results displayed in Figure 11b, Figure 12b or Figure 13b. At most, the discrepancy between the numerical and the experimental values is within 2–3 data samples. As the thin foam board was placed on a rigid optical table, it is believed that the mechanical properties of foam only material were not representative of the real test object. As such, Young’s modulus foam listed in Table 1 was calibrated to match the numerical and the experimental results.

6. Discussion and Conclusions

In statistics, the Pearson’s correlation coefficient is generally used to measure the linear correlation between two variables. The coefficient can be comprised between +1 and −1, where 1 is the total positive linear correlation, 0 is no linear correlation, and −1 is the total negative linear correlation. Following past studies [59,60], Pearson’s correlation coefficient was used in the work presented in this article to measure the similarity between the waveforms collected with the PXI and the wireless platform. The values of the coefficients for the steel, foam, and granite were 0.975, 0.878, and 0.957, respectively. Although this observation needs data from more materials and a greater number of tests in order to be definitive, the trend of the coefficients seems to be related to Young’s modulus of the test specimen. In general, a coefficient greater than 0.8 is considered to be strong evidence of a linear relationship [61]. In this context, it means that it is very likely that the mean waveforms from the PXI and PCB are simply scaled versions of each other. The Pearson coefficients confirm the research hypothesis that the proposed wireless module can replace the wired configuration to perform NDE/SHM using HNSWs.

The quantitative results relative to the ToF are summarized in Table 2, which presents the average value of the ToF, and the corresponding standard deviation and coefficient of variation (CoV) for all the experiments conducted in this study. Additionally, the difference in percent between the numerical and the PCB-measured ToF is reported. Overall, it can be said that the experimental results are in very good agreement with the numerical values and the difference is within the margin associated with the sampling period of the instrumentation, i.e., related to the accuracy provided by the sampling frequency adopted in the experiments. By observing the standard deviations, they are within 1–2 data samples. In addition, the coefficient of variation is quite small proving the repeatability of the experiments.

Table 2. Summary of the experimental and numerical results relative to the time-of-flight of the primary reflected solitary wave. The CoV represents the coefficient of variation, i.e., the ration of the standard deviation to the mean value.

Parameter	Material		
	Steel	Granite	Foam
ToF numerical (μsec)	333	359	2494
ToF experim.: PCB mean (μsec)	320	347	2510
ToF experim.: PCB Standard deviation (μsec)	8.20	12.1	20.5
ToF experim.: PCB CoV (%)	2.56	3.47	0.82
ToF experim.: PXI mean (μsec)	313	341	2551
ToF experim.: PXI Standard deviation (μsec)	8.76	14.2	27.1
ToF experim.: PXI CoV (%)	2.79	4.16	1.06
Numerical/PCB difference (%)	3.90	3.34	0.64

In conclusion, in the study presented in this article, a wireless node was designed, assembled, and tested to support the generation, propagation, and detection of highly nonlinear solitary waves. The aim was to develop the components of a custom system that allows for structural health monitoring applications based on solitary waves. The development of the wireless sensor node included the design of a filter, a driver, and a mobile application. To prove the feasibility of the first prototype, three different interface materials were tested using two HNSW transducers. One transducer was conventionally wired to a National Instruments PXI running under LabView and one transducer was connected to a wireless node and driven with a mobile App using a tablet. The experimental results showed an excellent agreement with respect to each other and with respect to an analytical model that described the dynamic interaction between the waves and the material in dry contact with the chain. This is proof of the reliability of our wireless platform.

In the future, the wireless system needs to be improved over a few fronts. The sampling frequency should be increased to at least 1 or 2 MHz in order to reduce the sampling period and to make the system more sensitive to variations within the material being probed. The power necessary to drive the solenoid needs to be reduced in order to increase the battery life and allow the system to last longer before calling upon battery replacement. The development of a power solar cell to harvest energy would allow the wireless node to operate indefinitely. The latter would also be a suitable solution to power low voltage electronics. With the current design, the 3.7 V, 2500 mAh battery can power the low voltage electronics for 14 h. Besides harvesting energy with a solar module, another remedy could be adding both a separate smaller battery to power the Bluetooth module while it sleeps in a low power mode and hardware to allow the Bluetooth module to turn on the rest of the board once it receives a wake-up signal.

Author Contributions: Conceptualization, P.R. and S.J.D.; methodology, P.R. and S.J.D.; software, R.M. and H.J.; validation, R.M. and H.J.; formal analysis, R.M. and H.J.; investigation, R.M. and H.J.; resources, P.R.; data curation, R.M. and H.J.; writing—original draft preparation, R.M. and H.J.; writing—review and editing, P.R. and S.J.D.;

visualization, P.R.; supervision, P.R. and S.J.D.; project administration, P.R.; funding acquisition, P.R. All authors have read and agreed to the published version of the manuscript.

Funding: This research was funded by the U.S. National Science Foundation, grant number 1809932. The second author acknowledges the 2019 Fellowship Research Award from the American Society for Nondestructive Testing. The authors acknowledge the contribution of Samuel Peterson in the initial design of the mobile application.

Conflicts of Interest: The authors declare no conflict of interest.

References

- Nesterenko, V. Propagation of nonlinear compression pulses in granular media. *J. Appl. Mech. Tech. Phys.* **1984**, *24*, 733–743. [[CrossRef](#)]
- Nesterenko, V. *Dynamics of Heterogeneous Materials*; Springer Science & Business Media: New York, NY, USA, 2013.
- Coste, C.; Falcon, E.; Fauve, S. Solitary waves in a chain of beads under Hertz contact. *Phys. Rev. E* **1997**, *56*, 6104. [[CrossRef](#)]
- Coste, C.; Gilles, B. On the validity of Hertz contact law for granular material acoustics. *Eur. Phys. J. B* **1999**, *7*, 155–168. [[CrossRef](#)]
- Manciu, M.; Sen, S.; Hurd, A.J. The propagation and backscattering of soliton-like pulses in a chain of quartz beads and related problems.(I). Propagation. *Physica A* **1999**, *274*, 588–606. [[CrossRef](#)]
- Manciu, M.; Sen, S.; Hurd, A.J. The propagation and backscattering of soliton-like pulses in a chain of quartz beads and related problems.(II). Backscattering. *Physica A* **1999**, *274*, 607–618. [[CrossRef](#)]
- Daraio, C.; Nesterenko, V.; Herbold, E.; Jin, S. Strongly nonlinear waves in a chain of Teflon beads. *Phys. Rev. E* **2005**, *72*, 016603. [[CrossRef](#)] [[PubMed](#)]
- Daraio, C.; Nesterenko, V. Strongly nonlinear wave dynamics in a chain of polymer coated beads. *Phys. Rev. E* **2006**, *73*, 026612. [[CrossRef](#)]
- Daraio, C.; Nesterenko, V.; Herbold, E.; Jin, S. Tunability of solitary wave properties in one-dimensional strongly nonlinear phononic crystals. *Phys. Rev. E* **2006**, *73*, 026610. [[CrossRef](#)]
- Porter, M.A.; Daraio, C.; Szelengowicz, I.; Herbold, E.B.; Kevrekidis, P. Highly nonlinear solitary waves in heterogeneous periodic granular media. *Physica D* **2009**, *238*, 666–676. [[CrossRef](#)]
- Nesterenko, V.; Daraio, C.; Herbold, E.; Jin, S. Anomalous wave reflection at the interface of two strongly nonlinear granular media. *Phys. Rev. Lett.* **2005**, *95*, 158702. [[CrossRef](#)]
- Khatri, D.; Daraio, C.; Rizzo, P. Coupling of highly nonlinear waves with linear elastic media. In Proceedings of the Sensors and Smart Structures Technologies for Civil, Mechanical, and Aerospace Systems 2009, San Diego, CA, USA, 9–12 March 2009; p. 72920P.
- Hong, J.; Ji, J.-Y.; Kim, H. Power laws in nonlinear granular chain under gravity. *Phys. Rev. Lett.* **1999**, *82*, 3058. [[CrossRef](#)]
- Hong, J. Universal power-law decay of the impulse energy in granular protectors. *Phys. Rev. Lett.* **2005**, *94*, 108001. [[CrossRef](#)] [[PubMed](#)]
- Job, S.; Melo, F.; Sokolow, A.; Sen, S. How Hertzian solitary waves interact with boundaries in a 1D granular medium. *Phys. Rev. Lett.* **2005**, *94*, 178002. [[CrossRef](#)] [[PubMed](#)]
- Vergara, L. Scattering of solitary waves from interfaces in granular media. *Phys. Rev. Lett.* **2005**, *95*, 108002. [[CrossRef](#)] [[PubMed](#)]
- Fraternali, F.; Porter, M.A.; Daraio, C. Optimal design of composite granular protectors. *Mech. Adv. Matter Struct.* **2009**, *17*, 1–19. [[CrossRef](#)]
- Ni, X.; Rizzo, P.; Daraio, C. Laser-based excitation of nonlinear solitary waves in a chain of particles. *Phys. Rev. E* **2011**, *84*, 026601. [[CrossRef](#)] [[PubMed](#)]
- Zheng, B.; Rizzo, P.; Nasrollahi, A. Outlier analysis of nonlinear solitary waves for health monitoring applications. *Struct. Health Monit.* **2019**, 1475921719876089. [[CrossRef](#)]
- Cai, L.; Rizzo, P.; Al-Nazer, L. On the coupling mechanism between nonlinear solitary waves and slender beams. *Int. J. Solids Struct.* **2013**, *50*, 4173–4183. [[CrossRef](#)]
- Rizzo, P.; Nasrollahi, A.; Deng, W.; Vandebossche, J.M. Detecting the presence of high water-to-cement ratio in concrete surfaces using highly nonlinear solitary waves. *Appl. Sci.* **2016**, *6*, 104. [[CrossRef](#)]

22. Ni, X.; Rizzo, P. Use of highly nonlinear solitary waves in nondestructive testing. *Mater. Eval.* **2012**, *70*, 561–569.
23. Spadoni, A.; Daraio, C. Generation and control of sound bullets with a nonlinear acoustic lens. *Proc. Natl. Acad. Sci. USA* **2010**, *107*, 7230–7234. [[CrossRef](#)] [[PubMed](#)]
24. Carretero-González, R.; Khatri, D.; Porter, M.A.; Kevrekidis, P.; Daraio, C. Dissipative solitary waves in granular crystals. *Phys. Rev. Lett.* **2009**, *102*, 024102. [[CrossRef](#)] [[PubMed](#)]
25. Daraio, C.; Ngo, D.; Nesterenko, V.; Fraternali, F. Highly nonlinear pulse splitting and recombination in a two-dimensional granular network. *Phys. Rev. E* **2010**, *82*, 036603. [[CrossRef](#)] [[PubMed](#)]
26. Karanjgaokar, N.; Kocharyan, H. Influence of Lateral Constraints on Wave Propagation in Finite Granular Crystals. *J. Appl. Mech.* **2020**, *87*, 071011.
27. Jalali, H.; Rizzo, P.; Nasrollahi, A. Asymmetric propagation of low-frequency acoustic waves in a granular chain using asymmetric intruders. *J. Appl. Phys.* **2019**, *126*, 075116. [[CrossRef](#)]
28. Porter, M.A.; Daraio, C.; Herbold, E.B.; Szelengowicz, I.; Kevrekidis, P. Highly nonlinear solitary waves in periodic dimer granular chains. *Phys. Rev. E* **2008**, *77*, 015601. [[CrossRef](#)]
29. Yang, J.; Silvestro, C.; Khatri, D.; De Nardo, L.; Daraio, C. Interaction of highly nonlinear solitary waves with linear elastic media. *Phys. Rev. E* **2011**, *83*, 046606. [[CrossRef](#)]
30. Ni, X.; Rizzo, P. Highly Nonlinear Solitary Waves for the Inspection of Adhesive Joints. *Exp. Mech.* **2012**, *52*, 1493–1501. [[CrossRef](#)]
31. Kim, E.; Restuccia, F.; Yang, J.; Daraio, C. Solitary wave-based delamination detection in composite plates using a combined granular crystal sensor and actuator. *Smart Mater. Struct.* **2015**, *24*, 125004. [[CrossRef](#)]
32. Yang, J.; Silvestro, C.; Sangiorgio, S.N.; Borkowski, S.L.; Ebramzadeh, E.; De Nardo, L.; Daraio, C. Nondestructive evaluation of orthopaedic implant stability in THA using highly nonlinear solitary waves. *Smart Mater. Struct.* **2011**, *21*, 012002. [[CrossRef](#)]
33. Yang, J.; Sangiorgio, S.N.; Borkowski, S.L.; Silvestro, C.; De Nardo, L.; Daraio, C.; Ebramzadeh, E. Site-specific quantification of bone quality using highly nonlinear solitary waves. *J. Biomech. Eng.* **2012**, *134*, 101001. [[CrossRef](#)] [[PubMed](#)]
34. Yang, J.; Restuccia, F.; Daraio, C. Highly nonlinear granular crystal sensor and actuator for delamination detection in composite structures. In *International Workshop on Structural Health Monitoring, Stanford, CA*; 2011; pp. 123–134.
35. Nasrollahi, A.; Deng, W.; Rizzo, P.; Vuotto, A.; Vandenbossche, J.M. Nondestructive testing of concrete using highly nonlinear solitary waves. *Nondestruct. Test. Eval.* **2017**, *32*, 381–399. [[CrossRef](#)]
36. Li, F.; Zhao, L.; Tian, Z.; Yu, L.; Yang, J. Visualization of solitary waves via laser Doppler vibrometry for heavy impurity identification in a granular chain. *Smart Mater. Struct.* **2013**, *22*, 035016. [[CrossRef](#)]
37. Shelke, A.; Uddin, A.; Yang, J. Impact identification in sandwich structures using solitary wave-supporting granular crystal sensors. *AIAA J.* **2014**, *52*, 2283–2290. [[CrossRef](#)]
38. Schiffer, A.; Alkhaja, A.; Yang, J.; Esfahani, E.; Kim, T.-Y. Interaction of highly nonlinear solitary waves with elastic solids containing a spherical void. *Int. J. Solids Struct.* **2017**, *118*, 204–212. [[CrossRef](#)]
39. Yang, J.; Khatri, D.; Anzel, P.; Daraio, C. Interaction of highly nonlinear solitary waves with thin plates. *Int. J. Solids Struct.* **2012**, *49*, 1463–1471. [[CrossRef](#)]
40. Schiffer, A.; Kim, T.-Y. Modelling of the interaction between nonlinear solitary waves and composite beams. *Int. J. Mech. Sci.* **2019**, *151*, 181–191. [[CrossRef](#)]
41. Singhal, T.; Kim, E.; Kim, T.-Y.; Yang, J. Weak bond detection in composites using highly nonlinear solitary waves. *Smart Mater Struct.* **2017**, *26*, 055011. [[CrossRef](#)]
42. Berhanu, B.; Rizzo, P.; Ochs, M. Highly nonlinear solitary waves for the assessment of dental implant mobility. *J. Appl. Mech.* **2013**, *80*, 0110281–0110288. [[CrossRef](#)]
43. Nasrollahi, A.; Rizzo, P.; Orak, M.S. Numerical and experimental study on the dynamic interaction between highly nonlinear solitary waves and pressurized balls. *J. Appl. Mech.* **2018**, *85*, 031007. [[CrossRef](#)]
44. Nasrollahi, A.; Lucht, R.; Rizzo, P. Solitary Waves to Assess the Internal Pressure and the Rubber Degradation of Tennis Balls. *Exp. Mech.* **2019**, *59*, 65–77. [[CrossRef](#)]
45. Nasrollahi, A.; Orak, M.S.; James, A.; Weighardt, L.; Rizzo, P. A Nondestructive Evaluation Approach to Characterize Tennis Balls. *ASME J. Nondestruct. Eval.* **2019**, *2*, 011004. [[CrossRef](#)]
46. Nasrollahi, A.; Rizzo, P. Modeling a new dynamic approach to measure intraocular pressure with solitary waves. *J. Mech. Behav. Biomed.* **2020**, *103*, 103534. [[CrossRef](#)]

47. Nasrollahi, A.; Rizzo, P. Axial stress determination using highly nonlinear solitary waves. *J. Acoust. Soc. Am.* **2018**, *144*, 2201–2212. [[CrossRef](#)]
48. Nasrollahi, A.; Rizzo, P. Numerical Analysis and Experimental Validation of a Nondestructive Evaluation Method to Measure Stress in Rails. *ASME J. Nondestruct. Eval.* **2019**, *2*, 031002. [[CrossRef](#)]
49. Li, J.; Mechtov, K.A.; Kim, R.E.; Spencer, B.F., Jr. Efficient time synchronization for structural health monitoring using wireless smart sensor networks. *Struct. Control. Health Monit.* **2016**, *23*, 470–486. [[CrossRef](#)]
50. Lynch, J.P.; Loh, K.J. A summary review of wireless sensors and sensor networks for structural health monitoring. *Shock. Vib.* **2006**, *38*, 91–130. [[CrossRef](#)]
51. Noel, A.B.; Abdou, A.; Elfouly, T.; Ahmed, M.H.; Badawy, A.; Shehata, M.S. Structural health monitoring using wireless sensor networks: A comprehensive survey. *IEEE Commun. Surv. Tutor.* **2017**, *19*, 1403–1423. [[CrossRef](#)]
52. Aygün, B.; Gungor, V.C. Wireless sensor networks for structure health monitoring: Recent advances and future research directions. *Sens. Rev.* **2011**, *31*, 261–276. [[CrossRef](#)]
53. Abdulkarem, M.; Samsudin, K.; Rokhani, F.Z.; A Rasid, M.F. Wireless sensor network for structural health monitoring: A contemporary review of technologies, challenges, and future direction. *Struct. Health Monit.* **2019**. [[CrossRef](#)]
54. Jalali, H.; Rizzo, P. Highly nonlinear solitary waves for the detection of localized corrosion. *Smart Mater. Struct.* **2020**. accepted for publication.
55. Easwaran, S.N.; Weigel, R. 1.3 A_v-2V Tolerant Solenoid Drivers for Pedestrian Protection in Active Hood Lift Systems. In Proceedings of the 2018 IEEE International Symposium on Circuits and Systems (ISCAS), Florence, Italy, 27–30 May 2018.
56. Thach, H.; Townsend, K. Adafruit_BluefruitLE_Firmware, GitHub repository. Available online: https://github.com/adafruit/Adafruit_BluefruitLE_Firmware (accessed on 1 May 2020).
57. García, A. Bluefruit LE Connect v2, GitHub repository. Available online: https://github.com/adafruit/Bluefruit_LE_Connect_v2 (accessed on 1 May 2020).
58. Herbold, E.B. Optimization of the Dynamic Behavior of Strongly Nonlinear Heterogeneous Materials. Ph.D. Thesis, University of California, San Diego, CA, USA, 2008.
59. Rebonatto, M.T.; Schmitz, M.A.; Spalding, L.E.S. Methods of comparison and similarity scoring for electrical current waveforms. In Proceedings of the 12th Iberian Conference on Information Systems and Technologies (CISTI), Lisbon, Portugal, 14–17 June 2017; pp. 1–6.
60. Di Lena, P.; Margara, L. Optimal global alignment of signals by maximization of Pearson correlation. *Inform. Process. Lett.* **2010**, *110*, 679–686. [[CrossRef](#)]
61. Akoglu, H. User's guide to correlation coefficients. *Turk. J. Emerg. Med.* **2018**, *18*, 91–93. [[CrossRef](#)] [[PubMed](#)]



© 2020 by the authors. Licensee MDPI, Basel, Switzerland. This article is an open access article distributed under the terms and conditions of the Creative Commons Attribution (CC BY) license (<http://creativecommons.org/licenses/by/4.0/>).

Article

Quantified Activity Measurement for Medical Use in Movement Disorders through IR-UWB Radar Sensor †

Daehyeon Yim ^{1,‡}, Won Hyuk Lee ^{1,‡}, Johanna Inhyang Kim ^{2,7}, Kangryul Kim ²,
Dong Hyun Ahn ^{3,7}, Young-Hyo Lim ⁴, Seok Hyun Cho ⁵, Hyun-Kyung Park ^{6,7,*} and
Sung Ho Cho ^{1,*}

¹ Department of Electronics and Computer Engineering, Hanyang University, 222 Wangsimni-ro, Seongdong-gu, Seoul 04763, Korea; ldh166@hanyang.ac.kr (D.Y.); lwh9886@gmail.com (W.H.L.)

² Department of Psychiatry, Hanyang University Medical Center, 222-1 Wangsimni-ro, Seongdong-gu, Seoul 04763, Korea; iambabyvox@hanmail.net (J.I.K.); kangryul@naver.com (K.K)

³ Department of Psychiatry, Hanyang University College of Medicine, 222 Wangsimni-ro, Seongdong-gu, Seoul 04763, Korea; ahndh@hanyang.ac.kr

⁴ Division of Cardiology, Department of Internal medicine, Hanyang University College of Medicine, 222 Wangsimni-ro, Seongdong-gu, Seoul 04763, Korea; mdoim@hanyang.ac.kr

⁵ Department of Otorhinolaryngology-Head and Neck Surgery, Hanyang University College of Medicine, 222 Wangsimni-ro, Seongdong-gu, Seoul 04763, Korea; shcho@hanyang.ac.kr

⁶ Department of Pediatrics, Hanyang University College of Medicine, 222 Wangsimni-ro, Seongdong-gu, Seoul 04763, Korea

⁷ Hanyang Inclusive Clinic for Developmental Disorders, Hanyang University Medical Center, 222-1 Wangsimni-ro, Seongdong-gu, Seoul 04763, Korea

* Correspondence: neopark@hanyang.ac.kr (H.-K.P.); dragon@hanyang.ac.kr (S.H.C.); Tel.: +82-2-2220-0390 (H.-K.P.); +82-2-2290-8397 (S.H.C.)

† This paper is an extended version of our paper published in Lee, W.H., Cho, S.H., Park, H.K., Cho, S.H., Lim, Y.H., Kim, K.R. Movement Measurement of Attention-Deficit/Hyperactivity Disorder (ADHD) Patients Using IR-UWB Radar Sensor. In Proceedings of the 2018 International Conference on Network Infrastructure and Digital Content (IC-NIDC), 2018.

‡ These authors contributed equally to this work.

Received: 31 December 2018; Accepted: 4 February 2019; Published: 8 February 2019

Abstract: Movement disorders, such as Parkinson’s disease, dystonia, tic disorder, and attention-deficit/hyperactivity disorder (ADHD) are clinical syndromes with either an excess of movement or a paucity of voluntary and involuntary movements. As the assessment of most movement disorders depends on subjective rating scales and clinical observations, the objective quantification of activity remains a challenging area. The purpose of our study was to verify whether an impulse radio ultra-wideband (IR-UWB) radar sensor technique is useful for an objective measurement of activity. Thus, we proposed an activity measurement algorithm and quantitative activity indicators for clinical assistance, based on IR-UWB radar sensors. The received signals of the sensor are sufficiently sensitive to measure heart rate, and multiple sensors can be used together to track the positions of people. To measure activity using these two features, we divided movement into two categories. For verification, we divided these into several scenarios, depending on the amount of activity, and compared with an actigraphy sensor to confirm the clinical feasibility of the proposed indicators. The experimental environment is similar to the environment of the comprehensive attention test (CAT), but with the inclusion of the IR-UWB radar. The experiment was carried out, according to a predefined scenario. Experiments demonstrate that the proposed indicators can measure movement quantitatively, and can be used as a quantified index to clinically record and compare patient activity. Therefore, this study suggests the possibility of clinical application of radar sensors for standardized diagnosis.

Keywords: IR-UWB radar sensor; movement disorder; hyperactivity; actigraphy

1. Introduction

Movement disorders, such as Parkinson's disease, dystonia, tic/Tourette's disorder, and attention-deficit/hyperactivity disorder (ADHD), are clinical syndromes with either an excess of movement or a paucity of voluntary and involuntary movements. The assessment of many movement disorders has heavily relied on clinical observation and rating scales, which are inherently subjective, and results vary according to the informant [1]. There is an increasing need for tools that objectively evaluate the level of activity. We focused on ADHD, among various movement disorders, to explore the possibility of a new evaluation method. ADHD is a common neurodevelopmental disorder characterized by inattention, impulsivity, and hyperactivity [2]. In contrast to the research on objective measurements of inattention, such as the continuous performance test (CPT), the assessment of hyperactivity in clinical settings is based on subjective reports from caregivers and from the observations of clinicians [3]. As hyperactivity is influenced by environmental factors and cognitive demands, discrepancy regarding the description of hyperactivity often occurs, thereby making the diagnosis of ADHD challenging [4].

Studies have been conducted, using infrared cameras (QbTest; Qb Tech, Stockholm, Sweden), 3D cameras (Microsoft Kinect, Redmond, US), or actigraphy (ActiGraph, Florida, US), to measure the objective level of activity in young people having ADHD [5]. However, these sensors have not been applied widely in clinical settings due to several limitations. A recent study reported that the QbTest is insufficient as a diagnostic test for ADHD, as it is unable to differentiate ADHD from other neurodevelopmental disorders [6]. Examination methods using infrared cameras, such as QbTest, are not perfectly non-contact, and measure the patient's concentration, but do not measure activity [7]. It can be difficult to judge exact whole-body motions, as these methods reflect only the movement of a specific part of the body. In the case of a depth camera or a 3D camera, the angle of view is limited to about 60 degrees, the performance varies depending on the indoor lighting environment, and the maximum measurable distance is as short as several meters [8]. Actigraphy has been the most commonly used device in measuring hyperactivity in ADHD [9]. Its primary use is measuring sleep and wakefulness, but it can also measure the movement of the subject in the x , y , and z axes, through an acceleration sensor [10]. It is not only possible to measure the amount of activity by obtaining the number of steps and the vector magnitude with this acceleration data, but the position can be estimated (even though the error is cumulative). However, as the device is worn on a certain part of the body, such as ankles and wrists, activity measurement does not reflect the movements of the whole body. The device is attached to the skin, and it may cause inconvenience for the user. Currently, actigraphy is considered to be useful in monitoring motor activity during treatment, but there is little evidence supporting the use of actigraphy in the diagnosis or as a screening tool for ADHD [11].

Impulse radio ultra-wideband (IR-UWB) radar sensors are capable of detecting objects without interference from other sensors through the use of ultra-wideband frequencies. Despite sending and receiving signals with very low power to comply with Federal Communications Commission (FCC) standards, they have enough range and resolution to observe the indoor environment. The primary advantages for clinical application of an IR-UWB radar sensor are its very low power and high spatial resolution. IR-UWB radar signals typically have a high resolution, so it can be used to detect the fine motion of objects [12]. Moreover, it is harmless to the human body and enables the diagnosis of the subject by a non-contact method, causing no inconvenience for the patient. The radar sensor is in a sustainable form and has no contact or requirement for the patient. As it has excellent penetrability, it can be installed on the wall invisibly, and so it is able to observe the target without attracting any attention from the target. Due to these characteristics, the measurement and quantification of activity in clinical movement disorders using an IR-UWB radar sensor is very promising. The IR-UWB radar sensor is capable of detecting not only large movements of the human body but also small movements, such as breathing. Recently, communications, localization, positioning, and tracking using the IR-UWB

radar sensor have been studied. Most applications can be performed simultaneously using the same hardware [13–15].

The purpose of this study was to calculate the objective quantity of movement by using four radar sensors to find the position of the subject, and to calculate the amount of body movement in a testing room, during an attention task called the comprehensive attention test (CAT), which is a computerized CPT widely used for ADHD patients [16]. Through this study, we will quantify the movement of subjects and present new indicators that can potentially be applied in the measurement of activity in movement disorders, such as ADHD. All of the different radar functions have one thing in common: The information is based on human movement. Therefore, movement information was obtained from radar signals and two types of movements were defined which could be measured by radar, based on changes in position. In regard to spatial movement (which refers to the movement of the subject accompanied with position change), the degree of movement can be calculated by replacing the position change amount with a vector by tracking. In regards to sedentary movement (which refers to the movement of the subject accompanied by little or no position change), the degree of movement was calculated by continuously measuring the amount of change in the magnitude of the reflected signal from the target.

The following sections introduce the signal model of the IR-UWB radar and the basic concept of the algorithm for the activity measurement. Then, a detailed description of the algorithm, based on the tracking and signal magnitude, is presented. Finally, after introducing the experimental environment and methods, experimental results are presented and analyzed.

2. Problem Statement

2.1. Signal Model and Basic Signal Processing

The impulse signal $s[k]$, emitted by the radar to observe the target area, is delayed and scaled while being reflected from the surrounding environment. The received signal of the radar is generated by the reflected $s[k]$ through N_{path} paths from the surrounding environment. The signal received by the i -th radar can be represented by the sampled signal $x_i[k]$, including the environment noise $\mathcal{N}[k]$, as follows

$$x_i[k] = \sum_{m=1}^{N_{path}} a_{m,i} s[k - \tau_{m,i}] + \mathcal{N}[k]. \quad (1)$$

The sampled time index k can be called a distance index, and is represented by a natural number from 0 to L_{signal} , which is the distance index of the maximum observable distance. When $s[k]$ is reflected on the m -th path of the i -th radar, $a_{m,i}$ and $\tau_{m,i}$ are the scale values and delays, respectively [15].

In an indoor environment, there are a lot of objects and walls and so there are various signals received, in addition to people. Reflected signals from the background are called clutter signals, and usually have a large and constant magnitude. Removing the clutter signals is necessary to observe only the reflected signal from the target, and requires a detection algorithm to detect people while excluding noise. Hence, we can only obtain signals for the target in the indoor environment. The basic signal processing procedure for detecting people is shown in Figure 1.

Background removal algorithms are used frequently in indoor environments to observe only the desired targets. A signal $y_i[k]$ with background removed from the received signal $x_i[k]$ can be obtained. The purpose of the initialization phase is to create a threshold. This threshold should reflect the characteristics of the experimental environment, so the initialization should proceed without any humans in the observation area of the IR-UWB radar. The environment-adapted threshold $T_i[k]$ is, then, used for detection in the real-time process.

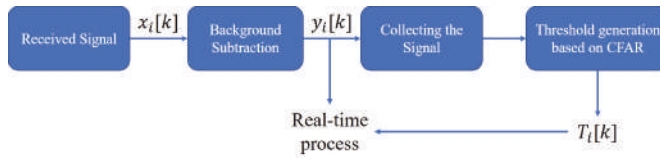


Figure 1. Basic signal processing.

Background subtraction is a technique for separating the foreground from the background, where walls or static objects correspond with the background, while the observed target corresponds with the foreground [17]. With this algorithm, background signals can be removed, and only the signal components of a moving target can be detected. The background clutter signal $C_{i,n}[k]$ is continually updated from the previous clutter signal $C_{i,n-1}[k]$ and $x_{i,n}[k]$, where n is the sequence number of the received signal in each radar, and $C_{i,n}[k]$ is subtracted from the radar signal $x_{i,n}[k]$ to obtain the background subtraction signal $y_{i,n}[k]$, which is expressed as

$$\begin{aligned} y_{i,n}[k] &= x_{i,n}[k] - C_{i,n}[k], \\ C_{i,n}[k] &= \alpha C_{i,n-1}[k] + (1 - \alpha)x_{i,n}[k]. \end{aligned} \quad (2)$$

To more accurately detect the signal of the target, the distance between the subject and the radar can be calculated from the background subtraction signal using the Constant False Alarm Rate (CFAR) algorithm [18]. Generally, it is common to detect using the cell-averaging (CA-CFAR) method with a certain window size in one-frame data received from the radar. However, the $y_i[k]$ collected by observing the environment without a target for a certain duration is represented as $\mathbf{Y}_i[k] = [y_{i,0}[k], y_{i,1}[k], y_{i,2}[k], \dots, y_{i,N_c}[k]]^T$, and is used for threshold value-generation, based on the CFAR method, where N_c is the number of collected $y_i[k]$. This allows the probability of false alarms to be set to a certain value by comparing the received signal from the target with the threshold level $T_i[k]$, expressed as

$$T_i[k] = \beta \sigma_i[k] + \mu_i[k], \quad (3)$$

where the subscript i points to the i -th radar, β is a parameter to adjust the false alarm rate, and $\mu_i[k]$ and $\sigma_i[k]$ are the mean and standard deviation of $\mathbf{Y}_i[k]$, respectively. When the background signal is removed, only the target signal and the noise remain, and the $y_i[k]$, applied with the background subtraction algorithm, can be expressed as

$$y_i[k] = \hat{r}_i[k] + \mathcal{N}_i[k], \quad (4)$$

where $\hat{r}_i[k]$ is the target signal estimated by the clutter removal in i -th radar and $\mathcal{N}_i[k]$ is the noise [15]. Therefore, if there is no target, such as when collecting a signal for a threshold, $y_i[k]$ only has noise. To detect the target separately from the noise, we can obtain the mean and variance of $\mathbf{Y}_i[k]$, and create a threshold as shown in Equation (3).

2.2. Basic Concept of Activity Measurement

Generally, because the reflection coefficient of the electromagnetic wave to the target does not change, there is no change in $x_i[k]$ if there is no movement. Conversely, when there is movement, the value of $x_i[k]$ changes because some paths differ from those of the previous environment. Additionally, the distance measurement to the target is calculated as k , where $x_i[k]$ is largely changed. The distance resolution of the UWB radar has units of a few millimeters, which can detect very small changes within the range of the radar. Therefore, it is impossible for a radar to miss even the very small movements of a human, and the amount of activity of the target can be measured by the change

of the magnitude of the radar signal and the moving distance information. However, because the radar can measure only one-dimensional distance data, it is limited to observing the target with one radar. Thus, multiple radars were used to measure the position of the target while simultaneously measuring the change in the magnitude of the signal, which was represented as activity.

In this paper, human movement is divided into two types: A type with a change in position, and a type with no change in position (such as sitting). The former is defined as spatial movement, and the latter is defined as sedentary movement. In the past, these two movements have been measured in different ways. One way is to measure the target's motion intensity (e.g., actigraphy sensor [19]), and the other is to track the target [5]. These two modes of motion are independent of each other, and have different characteristics. Spatial movements are observable movements from a macroscopic point of view, and sedentary movements are observable movements from a microscopic point of view. If the position of the target does not change, the measured distance of the radar does not change significantly, so the positioning information will not reflect sedentary movements well [20]. Conversely, if there is a change the position, the positioning information may reflect this movement, but it is difficult for the received signal magnitude to reflect the movement state, such as the position change or movement speed. Therefore, because it is difficult to confirm the amount of activity in all cases with one measurement method, an algorithm is proposed in this paper that can numerically compare the amount of activity through two indicators.

2.3. Experiment Scenario

We designed several scenarios to check our proposed indicators. The criteria for dividing the scenario first broadly, based upon whether there is any spatial movement, divides scenarios into two groups. These groups are then divided into several scenarios, depending on the degree of movement. This study is not intended to recognize specific actions, because it is aimed at measuring movement by projecting human motion using one-dimensional data. Therefore, each scenario was designed to include random behavior with minimal limitations. The list of scenarios is as follows:

1. When a person sits and concentrates on one thing;
2. When a person has a relatively small motion in a sitting position;
3. When a person has a relatively large motion in a sitting position;
4. When a person walks slowly in the room in a narrow radius;
5. When a person walks slowly in the room in a large radius;
6. When a person walks quickly in the room in a narrow radius;
7. When a person walks quickly in the room in a large radius.

The scenarios were designed to account for situations including movement during the test, and were only for reproducing other test environments. The proposed indicators have no particular dependency on CAT. Scenario 1 is a situation in which the target is focused on the test and does not move. In this scenario, the subject should minimize any actions other than the restricted, small movements required for the test. Scenarios 2 and 3 assumed that the target was seated for CAT, but cared about other things. Scenario 2 is a situation in which the limbs and the head move while the torso is fixed (such as looking around or touching something else). Scenario 3 is a situation in which the entire body moves in a sitting position, such as sitting with the chair tilted back. Scenarios 4–7 are four scenarios created using two opposing features. Scenarios 4 and 6 include walking near the center of the room, while Scenarios 5 and 7 include roaming the entire room. While Scenarios 4 and 5 are relatively slow walking scenarios, Scenarios 6 and 7 are relatively fast walking scenarios.

The greater the torso movement, the greater the sedentary movement index. This is because the torso takes up most of the human body. Thus, for our scenarios, the size of the sedentary movement index can be expected to decrease in order of Scenarios 3, 2, and 1. In Scenarios 4–7, it was expected that walking around a wide area or moving quickly would be observed as a larger movement than walking around a narrow area or moving slowly.

3. Algorithm for Measuring Activity

3.1. Measuring the Sedentary Movement

If there is a person with any movement, the corresponding $y_i[k]$ deviates greatly from the probability characteristics of the vacant state, so a person can be easily detected by comparing $y_i[k]$ with the threshold $T_i[k]$. If there is no person at the position of the k -th sample for i -th radar, $\hat{r}_i[k]$ is estimated to be zero in Equation (4), and $y_i[k]$ is not helpful in measuring activity. Previously, movement was simply represented as the sum of the differences in signal amplitude [21,22]. In this case, however, even when the difference between two consecutive frames is obtained, noise cannot be reduced. In cases where the motion is small, the amplitude of the target signal can be reduced. Therefore, to make only the signals from the target into activity indicators, we only used the samples for k where $y_i[k]$ exceeds the threshold $T_i[k]$, which can be expressed as

$$E_i[n] = \sum_{k=0}^{L_{signal}} g_{i,n}[k], \quad g_{i,n}[k] = \begin{cases} |y_{i,n}[k] - y_{i,n-1}[k]|^2 & \text{if } y_{i,n}[k] > T_i[k] \\ 0 & \text{if } y_{i,n}[k] \leq T_i[k] \end{cases}. \quad (5)$$

Of course, the received signal of a radar differs greatly, according to the distance to the target, and so, for a single radar, the degree of movement will vary greatly depending on the position. However, to compensate for this difference, it is necessary to consider not only the attenuation compensation along the distance, but also the compensation according to the antenna pattern in three dimensions. Further studies are needed to consider the relationship between position dependent signal attenuation and the clutter cancelling signal. We used the median of the data obtained by installing four radars at each corner of the four directions to apply the minimum compensation. If the target is too close to (or far from) any radar, it will be measured as too large (or too small), so the maximum and minimum values of E_i are excluded. Therefore, the proposed indicator to observe the sedentary movement can be expressed as

$$M_{sedentary}[n] = \text{Median}(E_0[n], E_1[n], E_2[n], \dots, E_{N_r}[n]), \quad (6)$$

where N_r is the number of radars for measurement and $\text{Median}(\cdot)$ is the function that returns the median value of the input value.

3.2. Measuring the Spatial Movement

There are not many people who move at a constant speed or only perform one action. Human behavior varies, and human movement is closely related to many forces; examples include friction forces and reaction forces from the earth. Due to these forces, the human movement state is constantly changing. However, for people who are not moving, the only movement is due to breathing. This means that there is almost no change in force. Because the force that moves a target is represented by the acceleration of the target, a person with active motion will have a greater acceleration than a person with slight motion. For this reason, it is possible to measure the amount of activity of an object through actigraphy [9]. As we cannot mathematically model the random movements of a person, we can use numerical differentiation to obtain the acceleration value from the data measured. Although the accuracy of the calculated acceleration may be low, we do not need the exact value [23].

The process of obtaining the acceleration begins by obtaining the distance value from each radar signal $y_i[k]$, obtained in Section 2.1. Methods for distance measurement in radar are already well known [24]. When the target exists in the observation region, multipath causes the signal magnitude to change at the distance index behind the target signal [15]. This magnitude change can be sufficiently above the threshold. Hence, in the signal $y_i[k]$, the shortest distance from the radar to the target can be obtained by using the minimum value of k satisfying $y_i[k] > T_i[k]$. Using the sampling frequency of the radar to convert from k to the actual distance unit, calculated as $d_i = c/f_s \times k$, d_{i_s} gives the distance from the i -th radar to the target measured.

The position of the target can be obtained by using the obtained d_i and the least-squares (LS) method. To apply LS, it is necessary to change the equation to be more simple. The circle equation, with radius d_i centered on the location of the i -th radar, (x_i, y_i, z_i) is represented by

$$(x - x_i)^2 + (y - y_i)^2 + (z - z_i)^2 = d_i^2. \quad (7)$$

Equation (7) for the l -th radar and the m -th radar can be rearranged, as Equation (8), to convert the quadratic equation into a linear equation:

$$2x(x_m - x_l) + 2y(y_m - y_l) + 2z(z_m - z_l) = d_l^2 - d_m^2 - x_l^2 + x_m^2 - y_l^2 + y_m^2 - z_l^2 + z_m^2. \quad (8)$$

To obtain the solution in the LS scheme, we can convert Equation (8) to matrix equation form, $Ax = b$, where A and b can be expressed as

$$A = 2 \begin{bmatrix} x_1 - x_0 & y_1 - y_0 & z_1 - z_0 \\ x_2 - x_1 & y_1 - y_0 & z_1 - z_0 \\ \dots & \dots & \dots \\ x_{N_r} - x_{N_r-1} & y_{N_r} - y_{N_r-1} & z_{N_r} - z_{N_r-1} \end{bmatrix}, \quad b = \begin{bmatrix} C_1 \\ C_2 \\ \dots \\ C_{N_r} \end{bmatrix}. \quad (9)$$

C_i replaces the right side of Equation (8) as $d_i^2 - d_{i-1}^2 - x_i^2 + x_{i-1}^2 - y_i^2 + y_{i-1}^2 - z_i^2 + z_{i-1}^2$. As the solution of LS is well known as the right side of Equation (10), we can obtain the position $p = [x_t, y_t, z_t]^T$ of the target:

$$p = (A^T A)^{-1} A^T b. \quad (10)$$

Position data can be obtained in real-time using the positioning method mentioned above. The position data for time n can be represented as $p[n] = [x_t[n], y_t[n], z_t[n]]^T$, where $x_t[n]$, $y_t[n]$, and $z_t[n]$ are the three-dimensional coordinates of the target. Using numerical differentiation, the velocity and acceleration of the target can be expressed as:

$$\begin{aligned} v[n] &= (p[n] - p[n-1])/t_r \\ a[n] &= (v[n] - v[n-1])/t_r. \end{aligned} \quad (11)$$

The observation period t_r of the radar is the sampling period for the target position data. The initial value can be specified by $v[0] = v[1] = a[0] = \mathbf{0}$. However, $a[n]$ will be closer to the acceleration at $n-1$, and not exactly at n . If the t_r is sufficiently small, there will be little time difference between n and $n-1$, and delay by one sample will not have a large impact. Therefore, even if the acceleration is not accurate, the acceleration and speed are calculated with Equation (11) to maintain real-time processing. As a result, the activity indicator for the spatial movement can be represented as:

$$M_{spatial}[n] = \beta \cdot a[n] = \gamma(p[n] - 2p[n-1] + p[n-2]). \quad (12)$$

As the amount of activity is not mathematically defined, the goal is not to create an accurate mathematical model in this paper. In other words, our goal is not to prove the exact relationship between acceleration and activity, but rather to suggest an indicator for objectively comparing activity. Therefore, we modeled the amount of activity and acceleration as a linearly proportional relationship.

4. Experiment Results

The XK300-MVI (Xandar Kardian, Toronto, ON, Canada) radar was used to verify the above algorithm. The X4M03 can select various center frequencies, from 7.29 GHz to 8.748 GHz, by adjusting various parameters according to local regulations. In these experiments, we selected the parameter

with a center frequency of 8.748 GHz and a bandwidth of 1.5 GHz as -10 dB concept. The radiation power of the radar was $68.85 \mu\text{W}$. The radar receiver can sample at 23.328 GS/s. The four radars were installed in each ceiling corner of the experimental room, as shown in Figure 2; which was 2.4 m in width, 3.0 m in length, and 2.4 m in height. In the indoor space, a distance error may occur due to the volume of a person; the radars were installed radially to minimize this error. The signal from the radars can be disturbed by movement of the arms or legs of the target. Hence, in order to reduce the effect of limbs as much as possible, radars were installed on the ceiling to observe the target. All of these radars were connected to the PC through the USB interface. The signal frames received from the radar were converted into digital values and transmitted to the PC by USB. These data were processed in MATLAB 2018b using the signal processing algorithm. The operating system of the PC was Windows 10. The frame-per-second (FPS) value of the signal received by the radar was 30.

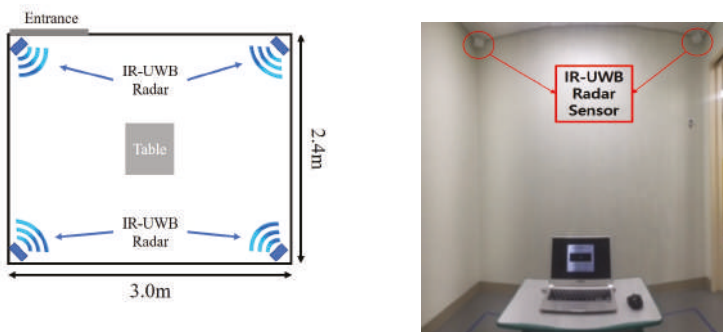


Figure 2. Experimental environment.

A table and a laptop were placed in the middle of the room for the experiment. In Scenario 1, the tester focused on the notebook. Scenarios 2 and 3 were also measured for sedentary movement situations, sitting in front of the table. From the center table, a space of approximately 1.2 m by 1.2 m was designated as a narrow area for Scenarios 4 and 6, and the entire room area was designated as a wide area for Scenarios 5 and 7. All of the experimenters performed scenarios consecutively, and they acted in a condition for about three minutes per scenario. Additionally, the empty room was used to generate the threshold value by measuring data for about three minutes.

The actigraphy data was measured, for comparison with the proposed IR-UWB radar base. Actigraphy sensors wGT3X-BT (ActiGraph, Florida, US) were worn on the right wrist and right ankle. In each actigraphy sensor, there is an accelerometer for measuring the movement of the body part. With a dedicated-license software called ActiLife (Actigraph, Florida, US), vector magnitude values were extracted to the PC at a sampling rate of 1 s. The data of the actigraphy sensors were scaled to compare the trends.

4.1. Experiment Results for Each Scenario

During the experiment, it was possible to check the data in real time. However, the distribution of results is more useful to characterize each scenario. Five researchers participated in the experiment, and were assigned three minutes per scenario. The results of applying the algorithm for sedentary movement are shown in Figure 3. The experimental results of $M_{sedentary}$ for Scenarios 1–3 are shown, with a significant difference, in Figure 3a. The experimental results show that $M_{sedentary}$ values increased in the order of Scenarios 1–3. Individual behaviors may vary in the same scenario, so the outcome varied slightly for each person. However, the trends in the results were all similar. As the scenario progressed from 1 to 3, the value of $M_{sedentary}$ increased, which indicates that the results of each scenario were consistent and relevant. Conversely, in Scenarios 4 to 7, the results for spatial

movement showed no significant difference in histogram and real-time measurement, and the values tended to be similar. This is effective for distinguishing the degree of sedentary movement with the algorithm used in Section 3.1, but it is insufficient for judging the degree of spatial movement around the room.

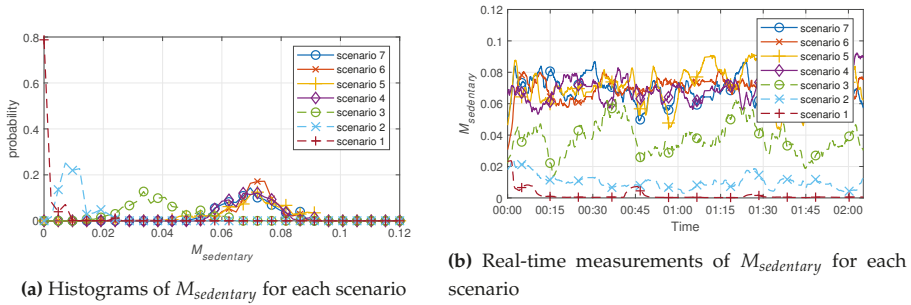


Figure 3. Experimental results of the sedentary movement index, $M_{sedentary}$, for each scenario.

In Section 3.2, the algorithm to find the position and acceleration of the subject was applied to the seven scenarios. As a result, the algorithm was made based on changes in the target’s position, so Scenarios 1 to 3 were smaller than Scenarios 4 to 7, and were not well distinguished. As the motions corresponding to Scenarios 4 to 7 consisted of traveling around the inside of the experimental room, the velocity was not constant, and the acceleration varied instantaneously. Therefore, the variation of the $M_{spatial}$ value for Scenarios 4 to 7 was larger than that of Scenarios 1 to 3. Additionally, Scenarios 5 and 7 consisted of traveling around the lab within a large radius, and are generally larger than Scenarios 4 and 6, which consisted of traveling within a small radius, as can be identified in Figure 4. Scenario 7, which involved moving quickly within a large radius, had the highest value in most real-time measurement areas. Each scenario can be distinguished by the $M_{spatial}$ value derived from the algorithm used, and it was shown that the degree of movement can be presented by measuring the spatial movement using the suggested indicator.

The mean values of each scenario obtained from the sedentary movement indicator, $M_{sedentary}$, and spatial movement indicator, $M_{spatial}$, are shown in Tables 1 and 2. It is difficult to compare the values of $M_{sedentary}$ and $M_{spatial}$ by themselves, because the algorithms used were different, and there are no units.

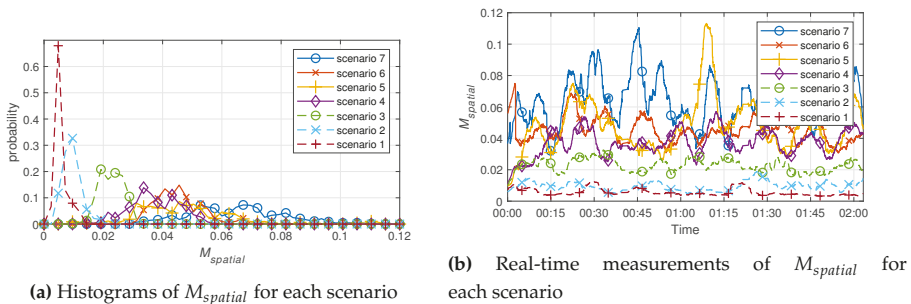


Figure 4. Experiment results of the spatial movement index, $M_{spatial}$, for each scenario.

Table 1. Numerical results are shown for each target. The results for the $M_{sedentary}$ indicator are summarized (no unit).

Scenario	Mean of $M_{sedentary}$					Total
	A	B	C	D	E	
1	0.16	0.16	0.14	0.30	0.19	0.19
2	1.01	1.77	0.76	0.73	0.85	1.02
3	3.81	4.27	2.30	2.20	2.01	2.92
4	6.99	5.10	2.78	5.72	4.74	5.07
5	7.11	5.04	4.64	5.11	4.43	5.27
6	7.15	6.60	3.06	5.04	7.02	5.77
7	6.94	5.39	4.57	3.85	6.25	5.40

Table 2. Numerical results are shown for each target. The results for the $M_{spatial}$ indicator are summarized (no unit).

Scenario	Mean of $M_{spatial}$					Total
	A	B	C	D	E	
1	0.55	0.68	0.56	0.54	0.47	0.56
2	0.95	1.25	1.20	1.72	1.56	1.34
3	2.28	2.65	2.89	2.53	3.46	2.76
4	3.71	2.52	2.75	3.75	2.91	3.13
5	4.77	4.27	4.56	5.37	3.40	4.47
6	4.54	3.21	4.15	5.82	3.44	4.23
7	6.46	6.16	5.45	7.55	5.60	6.24

Looking at the results in Tables 1 and 2, it can be seen that, for the same target scenario, the other targets were measured to be similar. Under similar circumstances, the measurement results are expected to be obtained at constant values. In the case of the $M_{spatial}$ of Scenarios 2 and 3, we can see that there is a significantly greater difference than for Scenarios 1 and 2. Scenarios 1–3 are all cases of sedentary movement, but position change was observed as much as torso shaking in Scenario 3. Nonetheless, the sedentary movement indicator is better discriminated in Scenarios 1–3. On the other hand, the spatial movement indicator is unlikely to have a sense of value in real-time, though it statistically has a significant difference in all scenarios. Sedentary movement indicators in Scenario 7 were measured to be lower than in Scenario 6, but more than or similar to those in Scenario 4. This clearly shows that a sedentary movement indicator cannot distinguish a change in position. However, from a different point of view, it can be seen that all walking scenarios show a certain value. In other words, we can see that Scenarios 4–7 can be classified as similar situations, because they do not observe a change in position from the point of view of the sedentary movement indicator. This confirms that similar behavior is measured at similar values.

Table 3. Physical condition of the participants.

Participants	A	B	C	D	E
Gender (M/F)	M	M	M	F	M
Height (cm)	174	176	167	171	177
Weight (kg)	75	67	65	63	90

The physical conditions of the researchers participating in the measurement are shown in Table 3. Although physical conditions did not differ greatly from each other, they do not seem to have a significant effect on the results. However, it is expected that $M_{sedentary}$ will be measured as small for small children. Because their size is small, their motion is also small. Conversely, it is expected that there will be no significant difference because $M_{spatial}$ depends on position changes.

4.2. Comparison with Actigraphy

The proposed index was verified using an actigraphy sensor, which is actually used for clinical activity measurement. Similarly, we proceeded with seven scenarios, with a graph comparing the changes in real time to confirm the similarity of the data, as shown in Figure 5. Both sedentary and spatial movements can be seen to fit well with the actigraphy data. However, Figure 5b shows that, for the last 3 min, only the sedentary movement indicator is different. This is explained in Section 4.1—because the actigraphy sensor is similar to the acceleration for spatial movement index calculation, it can be seen that $M_{\text{sedentary}}$ and actigraphy are very similar.

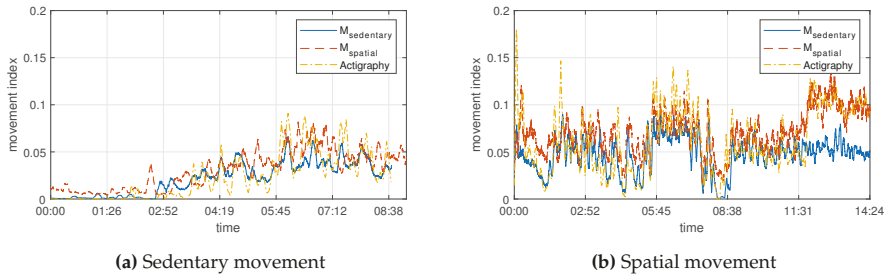


Figure 5. Graph of results when measured simultaneously with actigraphy. (a) and (b) are the results for sedentary and spatial movement, respectively. Actigraphy was scaled because the unit of the result data was not an actual physical quantity.

The limitations of the actigraphy sensor, compared with the radar sensor, can be seen in Figure 6, through an experiment of two extreme cases. In the previous 50 s, there was motion in the opposite hand and foot with the actigraphy sensor and, for the 50 s thereafter, there was movement of the hands and feet wearing the actigraphy sensor. The amount of movement measured from the radar during the entire section is largely constant, but the first 50 s has little movement measured from the actigraphy sensor. This result shows that the actigraphy sensor can only detect movement of a specific body part, but the radar sensor can detect movement of the entire body, even though it cannot distinguish each body part.

The actigraphy sensor is a contact-type sensor that should be worn on the wrists and ankles of the subject, and this can cause some pressure or stress for the subject during the experiment. In contrast, radar sensors are able to observe the patient's movements in a non-contact manner and so do not disturb the subject. It can be said that a radar sensor, which is a non-contact sensor, is effective for obtaining more detailed and reliable data in the diagnosis of movement disorders. In addition, the actigraphy sensor informs the activity amount of the subject, but it does not provide the direction of that amount of activity, the location of the actual subject, or the movement route. The position of the subject, obtained from multiple radar sensors, can provide more information than the actigraphy sensor in diagnosing a subject's specific habits, abrupt behavior, or hyperactivity. To date, there has been no index that can objectively express hyperactivity or specific movements in patients with movement disorders. However, it is possible to determine the position of the subject using the proposed algorithm and the radar sensor, and to measure the subject's degree of movement from the objectively quantified indicator.

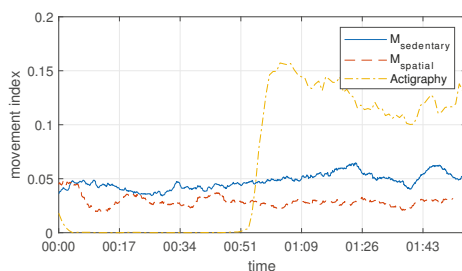


Figure 6. An extreme example of the proposed method and the use of actigraphy sensor. The actigraphy sensor is worn on a specific part of the body, so it may not reflect the whole movement (the first 50 s) or over-reflected (the last 50 s).

5. Conclusions

This paper proposed an algorithm and indicators to measure the amount of activity of people observed within certain constraints. Specifically, human activity was categorized into two types—without and with location movement—and two measurement indicators were proposed, that are specific to each activity with the signal strength and distance value data, measured by the radar sensor. Several scenarios and commercial products were used to confirm the reliability of the proposed indicators. Measurement can be performed simultaneously with the existing inspection to identify the actual activity amount, and this will be helpful in comparing the activity amount because the activity is quantified and more objective data is obtained. The IR-UWB radar sensors can measure heart rate and breathing while also recognizing gestures, making it a more practical solution in the medical field as it can be extended for additional functions in the future. Therefore, this quantitative technology for activity measurement may be useful in clinical applications as an assistive (complimentary tool) to diagnose movement disorders and to evaluate the efficacy of treatment based on direct observation by psychiatrists. It can additionally be used to overcome the limitations of conventional questionnaires by providing objective kinematic information about patients with movement disorders. Further, we can select indicators that are appropriate for our purpose because we can derive additional indicators (distance measurement, classification of standing and standing conditions, measuring activity area, among others) from our proposed algorithm.

Author Contributions: Conceptualization, D.Y. and W.H.L.; Data curation, D.Y. and W.H.L.; Formal analysis, D.Y. and W.H.L.; Investigation, D.Y. and W.H.L.; Methodology, D.Y. and W.H.L.; Resources, D.Y. and W.H.L.; Software, D.Y. and W.H.L.; Supervision, H.-K.P. and S.H.C.; Validation, J.I.K.; Writing—original draft, D.Y. and W.H.L.; Writing—review & editing, J.I.K., K.K., D.H.A., Y.-H.L., S.H.C., H.-K.P. and S.H.C.

Funding: This research was supported by Bio & Medical Technology Development Program (Next Generation Biotechnology) through the National Research Foundation of Korea (NRF) funded by the Ministry of Science, ICT, & Future Planning (2017M3A9E2064735)

Conflicts of Interest: The authors declare no conflict of interest.

References

1. FitzGerald, J.J.; Lu, Z.; Jareonsetasin, P.; Antoniadis, C.A. Quantifying motor impairment in movement disorders. *Front. Neurosci.* **2018**, *12*, 202. [[CrossRef](#)]
2. American Psychiatric Association. *Diagnostic and Statistical Manual of Mental Disorders (DSM-5®)*; American Psychiatric Publishing: Washington, DC, USA, 2013.
3. Valo, S.; Tannock, R. Diagnostic instability of DSM-IV ADHD subtypes: Effects of informant source, instrumentation, and methods for combining symptom reports. *J. Clin. Child Adolescent Psychol.* **2010**, *39*, 749–760. [[CrossRef](#)]

4. Kofler, M.J.; Raiker, J.S.; Sarver, D.E.; Wells, E.L.; Soto, E.F. Is hyperactivity ubiquitous in ADHD or dependent on environmental demands? Evidence from meta-analysis. *Clin. Psychol. Rev.* **2016**, *46*, 12–24. [[CrossRef](#)] [[PubMed](#)]
5. Hult, N.; Kadesjö, J.; Kadesjö, B.; Gillberg, C.; Billstedt, E. ADHD and the QbTest: diagnostic validity of QbTest. *J. Atten. Disord.* **2015**. [[CrossRef](#)]
6. Johansson, V.; Norén Selinus, E.; Kuja-Halkola, R.; Lundström, S.; Durbeej, N.; Anckarsäter, H.; Lichtenstein, P.; Hellner, C. The Quantified Behavioral Test Failed to Differentiate ADHD in Adolescents With Neurodevelopmental Problems. *J. Atten. Disord.* **2018**. [[CrossRef](#)]
7. Hall, C.L.; Valentine, A.Z.; Walker, G.M.; Ball, H.M.; Cogger, H.; Daley, D.; Groom, M.J.; Sayal, K.; Hollis, C. Study of user experience of an objective test (QbTest) to aid ADHD assessment and medication management: a multi-methods approach. *BMC Psychiatry* **2017**, *17*, 66. [[CrossRef](#)]
8. Du, H.; Henry, P.; Ren, X.; Cheng, M.; Goldman, D.B.; Seitz, S.M.; Fox, D. Interactive 3D modeling of indoor environments with a consumer depth camera. In Proceedings of the 13th international Conference on Ubiquitous Computing, Beijing, China, 17–21 September 2011; pp. 75–84.
9. De Crescenzo, F.; Licchelli, S.; Ciabattini, M.; Menghini, D.; Armando, M.; Alfieri, P.; Mazzone, L.; Pontrelli, G.; Livadiotti, S.; Foti, F.; et al. The use of actigraphy in the monitoring of sleep and activity in ADHD: A meta-analysis. *Sleep Med. Rev.* **2016**, *26*, 9–20. [[CrossRef](#)] [[PubMed](#)]
10. Robusto, K.M.; Trost, S.G. Comparison of three generations of ActiGraph™ activity monitors in children and adolescents. *J. Sports Sci.* **2012**, *30*, 1429–1435. [[CrossRef](#)] [[PubMed](#)]
11. Kam, H.; Shin, Y.; Cho, S.; Kim, S.; Kim, K.; Park, R. Development of a decision support model for screening attention-deficit hyperactivity disorder with actigraph-based measurements of classroom activity. *Appl. Clin. Inf.* **2010**, *1*, 377–393. [[CrossRef](#)] [[PubMed](#)]
12. Schleicher, B.; Nasr, I.; Trasser, A.; Schumacher, H. IR-UWB radar demonstrator for ultra-fine movement detection and vital-sign monitoring. *IEEE Trans. Micro. Theory Tech.* **2013**, *61*, 2076–2085. [[CrossRef](#)]
13. Nguyen, V.H.; Pyun, J.Y. Location detection and tracking of moving targets by a 2D IR-UWB radar system. *Sensors* **2015**, *15*, 6740–6762. [[CrossRef](#)] [[PubMed](#)]
14. Pallesen, S.; Grønli, J.; Myhre, K.; Moen, F.; Bjorvatn, B.; Hanssen, I.; Heglum, H.S.A. A pilot study of impulse radio ultra wideband radar technology as a new tool for sleep assessment. *J. Clin. Sleep Med.* **2018**, *14*, 1249–1254. [[CrossRef](#)] [[PubMed](#)]
15. Choi, J.W.; Yim, D.H.; Cho, S.H. People counting based on an IR-UWB radar sensor. *IEEE Sens. J.* **2017**, *17*, 5717–5727. [[CrossRef](#)]
16. Lee, J.S.; Kang, S.H.; Park, E.H.; Jung, J.S.; Kim, B.N.; Son, J.W.; Park, T.W.; Kim, B.S.; Lee, Y.S.; et al. Standardization of the comprehensive attention test for the Korean children and adolescents. *J. Korean Acad. Child Adolesc. Psychiatry* **2009**, *20*, 68–75.
17. Rakibe, R.S.; Patil, B.D. Background subtraction algorithm based human motion detection. *Int. J. Sci. Res. Publ.* **2013**, *3*, 2250–3153.
18. Maali, A.; Mesloub, A.; Djeddou, M.; Baudoin, G.; Mimoun, H.; Ouldali, A. CA-CFAR threshold selection for IR-UWB TOA estimation. In Proceedings of the International Workshop on Systems, Signal Processing and their Applications, WOSSPA, Tipaza, Algeria, 9–11 May 2011; pp. 279–282.
19. Grap, M.J.; Hamilton, V.A.; McNallen, A.; Ketchum, J.M.; Best, A.M.; Arief, N.Y.I.; Wetzel, P.A. Actigraphy: analyzing patient movement. *Heart Lung J. Acute Crit. Care* **2011**, *40*, e52–e59. [[CrossRef](#)] [[PubMed](#)]
20. Yim, D.; Cho, S.H. Indoor Positioning and Body Direction Measurement System Using IR-UWB Radar. In Proceedings of the 2018 19th International Radar Symposium (IRS), Bonn, Germany, 20–22 June 2018; pp. 1–9.
21. Lee, J.M.; Choi, J.W.; Cho, S.H. Movement analysis during sleep using an IR-UWB radar sensor. In Proceedings of the 2016 IEEE International Conference on Network Infrastructure and Digital Content (IC-NIDC), Beijing, China, 23–25 September 2016; pp. 486–490.
22. Lee, W.H.; Cho, S.H.; Park, H.K.; Cho, S.H.; Lim, Y.H.; Kim, K.R. Movement Measurement of Attention-Deficit/Hyperactivity Disorder (ADHD) Patients Using IR-UWB Radar Sensor. In Proceedings of the 2018 International Conference on Network Infrastructure and Digital Content (IC-NIDC), Guiyang, China, 22–24 August 2018; pp. 214–217.

23. Merry, R.; Van de Molengraft, M.; Steinbuch, M. Velocity and acceleration estimation for optical incremental encoders. *Mechatronics* **2010**, *20*, 20–26. [[CrossRef](#)]
24. Gezici, S.; Tian, Z.; Giannakis, G.B.; Kobayashi, H.; Molisch, A.F.; Poor, H.V.; Sahinoglu, Z. Localization via ultra-wideband radios: a look at positioning aspects for future sensor networks. *IEEE Signal Process. Mag.* **2005**, *22*, 70–84. [[CrossRef](#)]



© 2019 by the authors. Licensee MDPI, Basel, Switzerland. This article is an open access article distributed under the terms and conditions of the Creative Commons Attribution (CC BY) license (<http://creativecommons.org/licenses/by/4.0/>).

Article

Pre-Pressure Optimization for Ultrasonic Motors Based on Multi-Sensor Fusion

Ning Chen *, Jieji Zheng and Dapeng Fan

National University of Defense Technology, Deya Road No. 109, Kaifu District, Changsha 410073, China; 1024451173@126.com (J.Z.); fdp@nudt.edu.cn (D.F.)

* Correspondence: chenning007xm@126.com

Received: 5 February 2020; Accepted: 3 April 2020; Published: 8 April 2020

Abstract: This paper investigates the pre-pressure's influence on the key performance of a traveling wave ultrasonic motor (TRUM) using simulations and experimental tests. An analytical model accompanied with power dissipation is built, and an electric cylinder is first adopted in regulating the pre-pressure rapidly, flexibly and accurately. Both results provide several new features for exploring the function of pre-pressure. It turns out that the proportion of driving zone within the contact region declines as the pre-pressure increases, while a lower power dissipation and slower temperature rise can be achieved when the driving zones and the braking zones are in balance. Moreover, the shrinking speed fluctuations with the increasing pre-pressures are verified by the periodic-varying axial pressure. Finally, stalling torque, maximum efficiency, temperature rise and speed variance are all integrated to form a novel optimization criterion, which achieves a slower temperature rise and lower stationary error between 260 and 320 N. The practical speed control errors demonstrate that the proportion of residual error declines from 2.88% to 0.75% when the pre-pressure is changed from 150 to 300 N, which serves as one of the pieces of evidence of the criterion's effectiveness.

Keywords: traveling wave ultrasonic motor; pre-pressure; contact state; power dissipation; optimization criterion

1. Introduction

Ultrasonic motors, which work based on the converse piezoelectric effect and friction drive, tend to be the choice for precise actuators in diverse areas such as aerospace robots, manufacturing facilities, and especially for biomedical devices. Ultrasonic motors show their prominent advantages in biomedical devices like cell manipulation actuators [1], ear surgical devices [2], magnetic resonance imaging systems [3] and magnetic-compatible haptic interfaces [4,5]. This is due to ultrasonic motors' features, which include excellent properties like high torque at low speed, high torque to weight ratio and no electromagnetic noise [6–8]. Pre-pressure is a non-negligible factor in all types of ultrasonic motors, for example traveling wave ultrasonic motors (TRUMs) [9], linear ultrasonic motors [10], 2-DOF ultrasonic motors [11], hybrid DOF ultrasonic motors [12] and so on. Among them, the studies of TRUMs are most representative. In TRUMs, piezoelectric ceramics are actuated by two-phase alternating voltages, the elliptical trajectories of stator particles form the traveling wave impelling the rotor revolve. Pre-pressure is applied from the rotor against the stator to assure the interface contact and friction drive.

In processor studies, the performance sensitivities to the pre-pressure are mainly analyzed from the following three aspects. The first is the frequency characteristics. The first-order resonance frequency was investigated by the distributed numerical model and finite element model by Pirrotta [13]. His work found that the first-order resonance frequency was not sensitive to the preload force until the pre-pressure reaches a considerable value. However, these results were not verified by any further

experimental results. Afterwards, both the resonant frequency and anti-resonant frequency under diverse pre-pressures were tested in Oh's experiments [9]. He proved that the resonant frequency and anti-resonant frequency have a positive correlation with the preload force no matter whether the pressure is larger or smaller. Li [14] discovered that both frequencies do not increase monotonically with the pre-pressure. However, his data were collected from an impedance analyzer which only affords small-amplitude voltages (0–10 V). The second item is the contact properties. The contact state is the crucial contribution of pre-pressure for producing friction force and output torque. On this topic, Chen [15,16] developed a contact model via a semi-analytical model considering the radial slippage. The simulation results interpreted that the contact region and the driving zone become wider simultaneously when the pre-pressure increases, and the radial sliding inside the obstruction zone is also intensified. This useful yet incomplete analysis lacks any investigation on the contact state under load conditions. A contact model, which involves the distorted wave shape and standard stiffness of the contact layer, is built in [17]. This work also proves that the contact region becomes wider and the pressure at each contact point is raised with the increasing pre-pressure. Last but not least are the mechanical characteristics. Indeed, the mechanical characteristics integrate the results from the impedance characteristics and contact properties because the former determine the input power, and the latter affect the output power and torque. The most significant achievement in this aspect corresponds to Bullo [18]. He drew several three-dimension diagrams including speed, efficiency, output power both from simulations and experimental tests. However, the stator vibration amplitude was prescribed rather than adjusted by the differential functions, and the amplitude value is connected with voltage amplitude, driving frequency, applied load, and the initial pressure. His results also indicate that the incremental pre-pressure leads to a decreasing rotor speed under empty load conditions, but results in an increase of stalling torque.

Besides the above three performances concerning the preload force, this paper also proposes two new perspectives from the application viewpoint. One is the temperature rise arising from the power dissipation. As is well-known, TRUMs generate two energy conversion links, one is from electric energy to vibration energy based on the converse piezoelectric effect [19], and the other is from the vibration energy to the rotational energy via the friction between the stator and the rotor [20]. The energy losses occurring in the two processes not only reduce energy utilization but also significantly increase the internal temperature, which deteriorates TRUMs' performances. Previous authors have made several contributions [19,21] to compensate for the temperature rise to obtain a better speed control performance. However, few researchers have paid attention to the role of pre-pressure in the temperature variation. The other is the speed stability. It is known that there exist speed fluctuations due to the discontinuities in the contact distribution on stator teeth and manufacturing errors. Similarly, the role of pre-pressure in velocity stability regulation has not been explored. Besides, the sources and associated factors of fluctuation need to be better quantified. The sensitive relationships between pre-pressure and motor performances spread all over the motor, which brings difficulties in deriving a uniform optimization criterion, so a relatively effective candidate scheme for the optimization region should be assured through the joint analysis of multiple performance examples from sufficient experimental tests. Hence, accurate and digital-controllable pre-pressure adjustment devices are needed. Nonetheless, changing of the preload forces is mostly accomplished by manual feeding through a screw [14,22], which lacks guidance accuracy and regulatory flexibility. Even worse, the motor shell has been modified in some preload-adjusting apparatus [14,23], which adds the extra workloads.

In all, evaluation and optimization are the two main targets in this paper. In the evaluation process, modeling and experiment tests are synthetically implemented to evaluate the above performances under variable pre-pressure conditions. A hybrid model with the near-interface temperature rise is adopted to illustrate the frequency characteristics, contact properties, and temperature rise. A novel preload-control experimental apparatus is constructed from electric cylinder components, and a thin-film sensor is embedded inside a TRUM. In terms of the optimization process, the criterion considers the principles covering the lower temperature rise, the smaller speed stability, and the

moderate mechanical properties. Finally, the optimization region of the preload force in a prototype motor is determined.

This paper is organized as follows: Section 2 focuses on the simulation model combined with power dissipation. Section 3 introduces the test bench with an electric cylinder and the thin-film temperature sensor for measuring the near-interface temperature. Section 4 analyzes the sensitivities of the main performance features in function of the preload forces from simulation and experimental tests. Section 5 proposes an optimization criterion according to the integrated results. Finally, conclusions and outlook are given in Section 6.

2. A Simulation Model with Power Dissipation

Preload force, which is imposed between motor stator and friction material, impels the motor to move. It is closely related to the performances of all motor components. Therefore a comprehensive model is required to account for the internal mechanisms in detail. In this work a TRUM60A ultrasonic motor (Chunsheng Ultrasonic Motor Co, Ltd, Nanjing, China) was investigated. Its stator operates in the B_{09} mode. In other words, the number (N) of traveling waves is equal to 9.

2.1. The Electromechanical Model

A TRUM is a typical electromechanical coupling system combining piezoelectric actuation with friction drive [24]. As shown in Figure 1a, two-phase piezoelectric ceramics are bonded symmetrically below the ring-shaped stator made of phosphor bronze material. When two-phase AC voltages are applied to the piezoelectric ceramics, the traveling wave impels the stator particles to vibrate with elliptic trajectories. Finally, the movements and accumulated energy are transferred to the rotor through a friction interaction for driving the terminate load. The friction layer of TRUM60A is polytetrafluoroethylene (PTFE), which has excellent time-varying stability [25]. What should be emphasized is that there is a gasket or disc spring between the bearing and the rotor. The component serves as the elastic element for withstanding the deformation caused by pre-pressure during assembly.

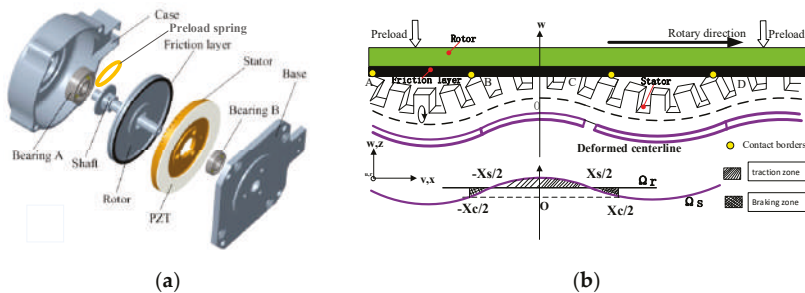


Figure 1. The mechanism of TRUM: (a) the motor structure [26]; (b) the traveling wave and contact state.

An electromechanical coupling TRUM model coalesces the models of both the driver and the motor itself. In this paper, a linear amplifying circuit is employed. After reproducing the actual circuit, the equivalent circuit model of piezoelectric ceramics is adopted. The ontology model originates from similar work by Kai [27], and the model equations and parameters are presented in Appendix A. Here, the critical parameters connected with the pre-pressure are mainly discussed and analyzed next. As shown in Figure 1b, due to the contact status and speed of the stator and the rotor, two feature points are generated on the stator teeth. One is the contact point used to distinguish whether the stator particles are embedded into the friction interface. The other is the sticking point, which is positioned at the point where the stator speed equals the rotor velocity. The stick points are applied to distinguish the driving zone and braking zone within the contact area. Usually, the contact length is defined as

X_c , and the length of the driving area is defined as X_s . Since the TRUM60A has nine traveling waves, each wave occupies 40° of circumferential space along the whole circle of the stator ring. Therefore the above two parameters yield $0 \leq X_s \leq X_c \leq 40^\circ$. Moreover, their values can be expressed as:

$$\begin{aligned} X_c &= \frac{20}{\pi} \arccos\left(\frac{h-z(t)}{R_{sc}\xi}\right) \\ X_s &= \frac{20}{\pi} \arccos\left(\frac{\Omega_r R_0^2}{\lambda h R_{sc} \xi f_s}\right) \end{aligned} \quad (1)$$

where ξ represents the vibration amplitude, h denotes the half-thickness of the piezoelectric laminated board, λ represents the wavelength of the traveling wave, f_s is the driving frequency and Ω_r is the angular velocity of the rotor. $R(r)$ is defined as the transverse displacement distribution function along the radial direction. The value on the middle radius at the contact surface R_0 is denoted as R_{sc} . Different from the model discussed in [27], the modal amplitude is corrected by the method proposed by Li [14], which takes the preload effect into account. When defining $k = N/R_0$, the contact parameters can be transformed into:

$$x_0 = \frac{\pi X_c}{40k} \quad x_1 = \frac{\pi X_s}{40k} \quad (2)$$

Thus, the overlap between the stator and the rotor defines the compression of the springs along the circumferential direction, thereby the pressure distribution function of the contact interface can be given by:

$$p(x) = K_f R_{sc} \xi [\cos(kx) - \cos(kx_0)] \quad (3)$$

where K_f represents the equivalent stiffness of the contact area. The output friction can be calculated by the surface integral of the forces within the contact area [25]. If the friction coefficient is defined as μ , ε means the width of the contact surface. Thus, the driving friction force can be read as:

$$\begin{aligned} F_R &= \mu \int_{R_0-\varepsilon/2}^{R_0+\varepsilon/2} \int_{-x_0}^{x_0} \text{sgn}(|\Omega_s(x)| - |\Omega_r(x)|) p(x) dx dy \\ &= \mu \int_{R_0-\varepsilon/2}^{R_0+\varepsilon/2} \int_{-x_0}^{-x_1} p(x) dx dy + \mu \int_{R_0-\varepsilon/2}^{R_0+\varepsilon/2} \int_{-x_1}^{x_1} p(x) dx dy + \mu \int_{R_0-\varepsilon/2}^{R_0+\varepsilon/2} \int_{x_1}^{x_0} p(x) dx dy \\ &= 2\mu K_f R_{sc} \xi \varepsilon \left\{ 2 \left[\frac{1}{k} \sin(kx_1) - x_1 \cos(kx_0) \right] - \left[\frac{1}{k} \sin(kx_0) - x_0 \cos(kx_0) \right] \right\} \end{aligned} \quad (4)$$

Obviously, the driving torque is derived from the multiplication between the average radius and the driving force. The summarizing result is depicted as:

$$T_R = N F_R R_0 = 2\mu \varepsilon K_f R_{sc} R_0^2 \xi \left\{ 2 [\sin(kx_1) - kx_1 \cos(kx_0)] - [\sin(kx_0) - kx_0 \cos(kx_0)] \right\} \quad (5)$$

Besides, the axial force, as well as the dynamic pressure on the stator surface, can be depicted as:

$$F_z = N \int_{R_0-\varepsilon/2}^{R_0+\varepsilon/2} \int_{-x_0}^{x_0} p(x) dx dy = 2N K_f R_{sc} \varepsilon \xi \left[\frac{1}{k} \sin(kx_0) - x_0 \cos(kx_0) \right] \quad (6)$$

2.2. The Power Dissipation Model

The traveling wave motor operates with several energy conversion processes from the power source to the rotor rotation. Indeed, there are three main power dissipations which are the dielectric dissipation of the piezoelectric ceramics, the vibration dissipation of the stator, and the heat dissipation of the contact interface, respectively.

At first, the dielectric dissipation of the piezoelectric ceramics yields Equation (7). Here ε_p means the dielectric constant of piezoelectric ceramic, $\tan \delta$ denotes the dielectric loss coefficient, and V_{piezo} represents the volume of the piezoelectric wafer:

$$Q_1 = 2\pi f_s \varepsilon_p \frac{U_m^2}{h_p^2} V_{\text{piezo}} \tan \delta \quad (7)$$

Secondly, quoting from the study of Lu [28], the mechanical damping dissipation can be displayed as:

$$Q_2 = f_{n1} \int_{V_{piezo}} \delta \bar{W}_{s1} dV = 4\pi^4 \xi^2 N^4 w (E_s I_s \eta_s + E_p I_p \eta_p) / (\lambda^3) \quad (8)$$

where E_s and E_p represent the equivalent elastic modulus of the stator and the piezoelectric strip, I_s and I_p denote their inertia moment, η_s and η_p are their mechanical damping coefficient, respectively.

Last but not least is the power dissipation of the friction interface. The friction interface serves as the medium which accomplishes the transformation from the stator's vibration to the rotor's rotation. The friction drive gives rise to the radial friction losses and tangential ones between the stator and the rotor. The power losses stemming from the friction interaction can be determined by:

$$Q_3 = N \frac{\lambda}{2\pi} \int_{kx_0}^{\pi-kx_0} \mu \Delta F (v_s - v_r) (v_s - v_r) d\theta = N \xi K_f \mu [M_1 v_{sm} v_r + M_2 (v_{sm}^2) / 2 + M_3 (v_r^2)] \quad (9)$$

where v_s , v_r are the linear velocity of the stator and the rotor, respectively, the v_{sm} denotes the peak stator speed of the traveling wave, and the remaining coefficients can be depicted as:

$$\begin{aligned} M_1 &= \pi - 2kx_0 + \sin(2kx_0) \\ M_2 &= -0.33 \cos(3kx_0) + 3 \cos(kx_0) - M_1 \sin(kx_0) \\ M_3 &= 2 \cos(3kx_0) - \pi \sin(kx_0) + 2\varphi \sin(kx_0) \end{aligned} \quad (10)$$

Among the three power losses, it is verified that the power dissipation of the friction interface is the largest. Therefore the friction interface becomes the primary heat field which has been proved by Finite Element Analysis [28], which serves as a fundament for the placement of the temperature sensor discussed in Section 3. Finally, the shell temperature function, which derives from the thermodynamics transmission processes between the air and the motor, yields:

$$T = T_{air} + \frac{Q_1 + Q_2 + Q_3}{\alpha S} (1 - e^{-\frac{\alpha S t}{C_{usm}}}) \quad (11)$$

where S is the contact surface area, α represents the convective heat transfer coefficient, C_{usm} is the heat capacity of the TRUM60A device. Moreover, it is worth noting that the near-interface temperature may be larger than T owing to the weak heat transfer capacity of the friction material. The rising temperature will lead to a speed decline and motor performance deterioration.

3. Experimental Setup

Figure 2a displays the mechanical test bench which is composed of an ultrasonic motor (TRUM60A), an incremental encoder (AFS60A, 65536 lines, SICK Corp., Waldkirch, Germany), an electric cylinder (EA0400, Huitong Corp., Nanjing, China), a torque sensor (9349A, Kistler, Sindelfingen, Germany) and a DC motor (55LYX04, YGGT Corp., Beijing, China) which is capable of generating any load profile in the current closed-loop mode. The electric cylinder is first employed to regulate the preload of the TRUM. As shown in Figure 2b, the axial force generated by the cylinder is transmitted from the piston rod to the motor shell. There is a force sensor (VC20A050, Vistle Corp., Guangzhou, China) which detects the real-time pressure. The pressure value can be displayed on a monitor or transmitted through a DA channel. Besides, the piston rod, the pressure sensor, and the pressboard were all limited inside a sleeve, which can assure the guidance accuracy of the axial movement. The design not only does not modify the TRUM's structure but also assures the accurate and digital control of the pre-pressure. Moreover, an NTC film sensor (FWBM-337G104F, Fu Wen Corp., Shenzhen, China) is selected for satisfying the space restraint and response bandwidth of the temperature characteristics. The sensor measures the heating body through the polyimide whose thickness is only 15 μm , and its response time is only 0.1 s. As shown in Figure 2d, the sensor is placed against the stator's teeth

gap and near the interface where the heat is most concentrated. The signal is processed through a Wheatstone bridge which has been embedded into the circuit.

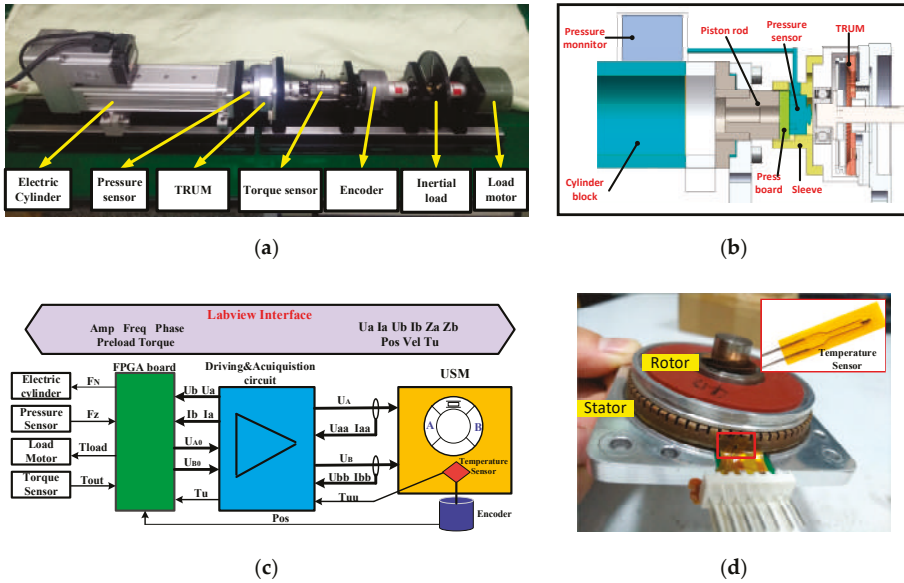


Figure 2. The integrated test system: (a) mechanical test bench; (b) structure scheme of the preload force regulating device; (c) framework and signal flow of the system; (d) the thin-temperature sensor placed near the interface.

Figure 2c introduces the framework of hardware and software. A driving & measurement circuit undertakes the function of amplifying the input signals. (U_{A0}, U_{B0}) and (U_A, U_B) are two pairs of voltages before and after amplifying, respectively. Meanwhile, the input voltages and currents are collected by voltage sensors and current sensors, respectively [29]. These channels are displayed from the signal group $(U_{aa}, I_{aa}, U_{bb}, I_{bb})$ to (U_a, U_b, I_a, I_b) . The generation of (U_{A0}, U_{B0}) and the acquisition of (U_A, I_A, U_B, I_B) are all conducted by a Field Programmable Gate Array (FPGA) control board (PXIE 7854R, NI Corp., Los Angeles, CA, USA). The FPGA programs can be transferred from the LABVIEW software, which provides abundant interfaces for algorithm generation and data acquisition [29]. The main parameters of the LABVIEW interface are all shown on the top of Figure 2c, where the left is the input parameters, and the output ones are listed in the right. In conclusion, a test system combining the flexible control of driving parameters and the accurate collection of the key parameters is built, which builds a foundation for exploring the sensitivities of motor performances under diverse pre-pressures.

4. Simulation and Experimental Results by Varying the Preload Force

The simulation model, as well as the measurement system, are used to comprehensively analyze the pre-pressure’s influences on several key performances including frequency characteristics, the stator/rotor contact states, the speed fluctuation, the temperature rise and the mechanical performance. Comparison and analysis are implemented for exploring the in-depth mechanism on how the preload force affects motion transfer and energy conversion.

4.1. The Stator/Rotor Contact

The stator/rotor contact is the premise that guarantees rotor rotation and torque output. If the driving parameters are unchanged, the contact status is mainly affected by the pre-pressure and the

imposed load. Therefore, Figure 3a displays the contact length and the driving length for different cases of pre-stressing forces when the amplitude is 200 V and the frequency is 43 kHz. At first, the contact length generates a profound change when the preload force jumps away from zero value. Then the contact zone becomes more extensive with the slope $0.033^\circ/\text{N}$ when the pre-pressure is increased from 100 to 570 N. Finally, the contact length increases with a higher slope until the contact area stretches over all the stator teeth. From the other curve, the length of the driving zone is equal to 40° when the stator is free from any pre-pressure. After that, the value gradually increases at a stable rate. However, it is always smaller than the contact length. This indicates that there exist driving areas and obstruction ones in the whole contact region. To be further, the proportion of the drive zone gradually decreases, which can also be verified from the proportion of the driving area in Figure 3b. These phenomena indicate that the stick-slip points gradually move toward the troughs of traveling waves, and the blocking effect is reinforced with the increasing pre-pressure, which induces more severe friction loss.

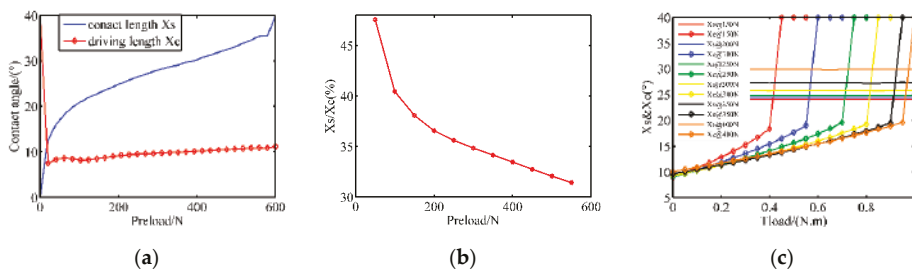


Figure 3. The contact parameters under diverse pre-pressures (simulation): (a) the contact angle and driving angle in no-load condition; (b) the proportion of driving zone in no-load condition; (c) the contact angle and driving angle with external load.

Once the motor operates with load, more output torque is needed to overcome the external torque, which causes the decline of rotor speed and the change of contact parameters. Figure 3c shows the contact parameters with respect to different loads from 0 to 0.9 N·m in function of pre-stressing forces. It is evident that the load has little effect on the contact length, which can also be verified by Equation (2). However, the driving length maintains a positive correlation with the load until the motor is blocked. In the blocking stage, the driving length returns to 40° again, which can be observed from the abrupt changes of the curves. In conclusion, if the preload is constant, the load torque does not affect the distribution of contact particles. And when the torque is constant, the contact area and the driving area gradually expand with the increase of the pre-pressures.

4.2. The Power Dissipation of the Motor

As discussed in Section 2, there are three main types of power dissipation inside the motor, and the temperature rise under different pre-pressures can be deduced. Figure 4 displays the respective time-variant energy loss in function of the preload forces when the amplitude and frequency are 200 V and 43 kHz, respectively. When the preload force is smaller than 460 N, the energy consumption increases as the preload force rises, which results from the gradually-widening contact area. By comparing the results of Figure 4a–c, it can be found that the dielectric loss maintains constant because the value is only related to the exciting voltage amplitude and the dielectric constant, which are both the intrinsic properties of piezoceramics. Furthermore, the stator damping loss and the friction loss follow similar positive-correlation laws until 460 N.

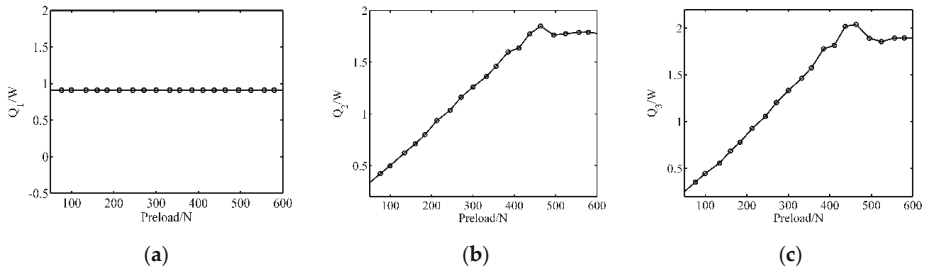


Figure 4. The respective power dissipation for the preload forces(Simulation): (a) Dielectric loss; (b) stator damping loss; (c) friction loss.

In order to exclude any additional factors, the starting temperature of every test should always be the same (28 °C), and the motor is turned off after the same time of operation (10 s). The results showing the motor speed and the near-interface temperature are displayed in Figure 5. The temperature rises immediately at the startup moment and drops rapidly once the driving voltages are withdrawn, which indicates that the accumulation and release of heat can be completed in a short time. Figure 5c demonstrates that the temperature rise achieves the highest value at 400 N, while the minimum temperature rise occurs when the preload is 300 N. With different temperature rise curves, the revolving speeds present different decline laws. It is evident that too fast speed decline is unfavorable for control and analysis.

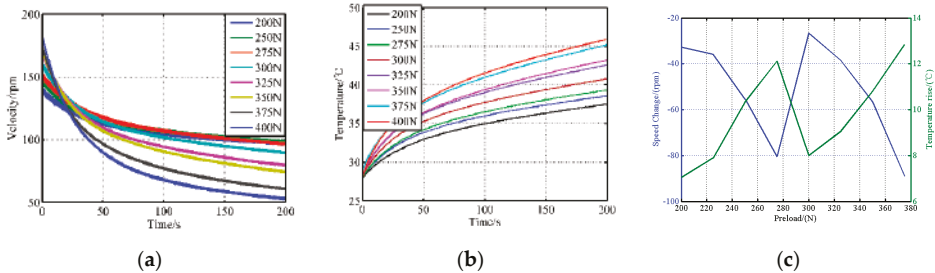


Figure 5. The startup-shutdown response under different pre-stressing forces (experimental): (a) the velocity response; (b) the temperature change; (c) temperature rise and speed decline.

4.3. The Speed Fluctuations

The speed fluctuations can be attributed to the errors of the shaft system during manufacturing or assembly. Whether the pre-stressing force compensates or deteriorates, the speed fluctuations should be investigated. Figure 6 displays the real-time speed with the preload force varying from 150 to 500 N in steps of 20 N. The rotor speed is recorded when the frequency is 43 kHz, and the amplitudes are 200 and 240 V, respectively. To facilitate the quantitative evaluation of the fluctuation, the standard deviation is adopted, as shown in Figure 6. The results indicate that the motor speed fluctuation becomes smaller and smaller due to the increasing embedment degree between the stator and the friction layer. It can be attributed to sufficient contact with the larger preload force. However, when the preload reaches 475 N, the reinforced radial slipping deteriorates the velocity stability. Since the simulation state ignores the machining and assembly problems, such as uneven axis alignment and surface roughness in the stator and the rotor, it is difficult to simulate the fluctuations effectively. Furthermore, the dynamic pressure applied to the rotor may be the origin of speed fluctuations. The pressure also has an impact on the

contact state. Here, the fluctuations are analyzed by the measurement of the speed and axial pressure in the subsequent experiments.

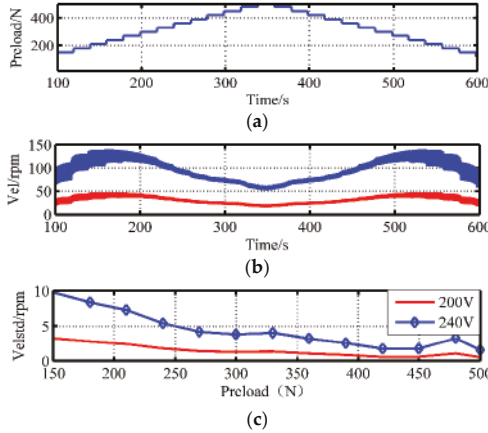


Figure 6. The speed stability under different preload forces: (a) staircase preloads; (b) output speed; (c) speed variance.

Based on the pressure F_z and the contact length x_0 in Equation (1) polynomial fitting is implemented to derive the mapping relationship from the axial pressure to the contact length, as shown in Equation (12). When the pre-pressure is 150 and 200 N, Figure 7 displays the real-time speed, the angular position, the corresponding pressure and the calculated contact length, respectively. We can observe that the velocity fluctuation satisfies a stretch of the 360° cycle, which demonstrates that the fluctuation mostly comes from the un-centered assembly error of the rotor shaft. The wave cycle elongates with declining speed. When the preload is 150 N, the ratio of the maximum fluctuant zone (1.01°) inside the contact zone (24.15°) is 2.53%. If the pre-tightening force is 200 N, the proportion becomes 3.11% as the fluctuation range and the contact angle are respectively 0.9° and 28.94° . In conclusion, the speed fluctuation comes from both the pressure change and the axial assembly error. The change of contact parameters is also accompanied by a pressure change:

$$X_c = 2.7 \times 10^{-16} F_z^7 - 6 \times 10^{-13} F_z^6 + 5.4 \times 10^{-10} F_z^5 - 2.5 \times 10^{-7} F_z^4 + 6.4 \times 10^{-5} F_z^3 - 0.0088 F_z^2 + 0.65 F_z + 0.72 \tag{12}$$

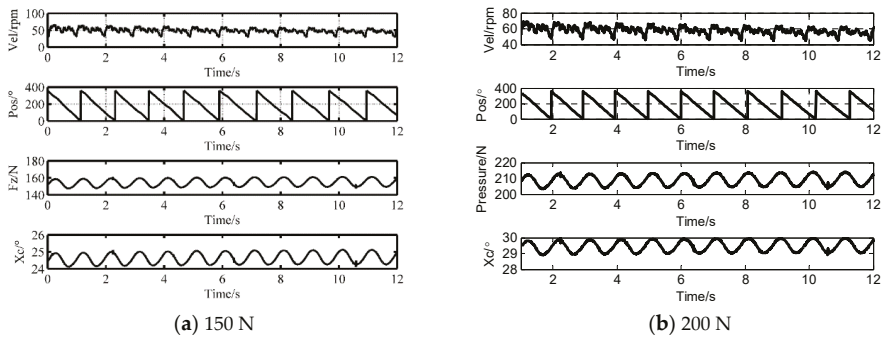


Figure 7. Time-domain analysis of dynamic pressure fluctuations and calculated contact angle.

4.4. The Mechanical Characteristics

With the aid of the electric cylinder and current sensors, a three-dimensional representation of the speed and the efficiency in function of the torque is shown in Figure 8 within the preload ranging from 150 to 400 N. The curves are obtained when the amplitude is 200 V and the frequency is 42 kHz. The dark blue areas are the stalling-torque areas, while the dark red ones are the maximum value zones of the respective curves. There exists a limit of the pre-stressing forces from which the motor performances fall. Figure 8b indicates the peak efficiency moves towards the larger-torque direction with the change of the preload forces. Deriving from the pictures, the blocking torque and maximum efficiency in function of the pre-pressures are displayed in Figure 8c. The blocking torque achieves the peak value in the moderate pre-pressure (260 N), so does the mechanical efficiency. The pre-pressure at the maximum efficiency point is 320 N. This is because the motor is close to the rotor-locked state when the pre-pressure is substantial, therefore the energy utilization is lower.

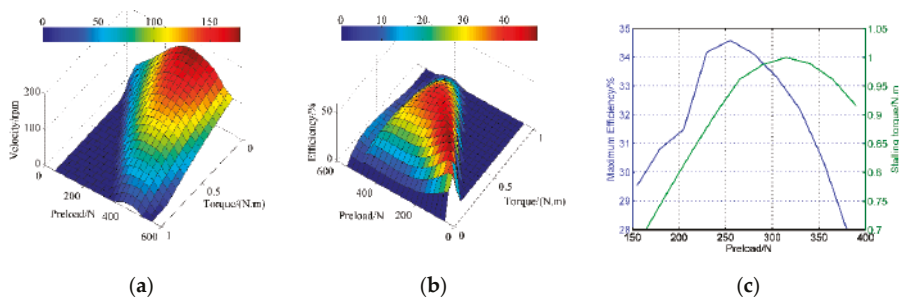


Figure 8. Simulation results of mechanical characteristics for different cases of pre-stressing forces: (a) revolving speed versus torque; (b) efficiency versus torque; (c) the calculated maximum efficiency and stalling torque.

5. Discussion and Verification of the Optimal Preload Force

The above simulation and experimental results reveal how the performances are sensitive to the pre-stressing force. In this section, these key performances are reviewed, and an optimal criterion is proposed.

5.1. Optimization Criterion

Some conclusions can be obtained from the above test results:

- (1) The velocity increases first and then decreases as the pre-pressure increases, and a low pre-pressure cannot provide sufficient friction force while a higher one causes more tangential friction zones;
- (2) When the pre-stressing force is lower, the velocity stability deteriorates because of the weakened constraints applied on the stator and the stability improves as the preload force gradually increases;
- (3) With the increase of the pre-pressure, the points both from the resonant frequency and the anti-resonant frequency gradually shift to the right due to the increasing stiffness;
- (4) The blocking torque achieves the peak value in the moderate pre-pressure, like the mechanical efficiency, however, the apexes are different from each other.

When limiting the pre-pressure range between 200 and 400 N, the key performances are summarized and arranged in Figure 9. Aiming at the lower open-loop speed stability, the preload force is supposed to be large enough for minimizing the dynamic fluctuations across the stator/rotor contact interface. Nonetheless, the moderate pressure is chosen based on the minimum temperature rise, which can decrease the undesirable changes in the tracking performances in the servo-control scheme. Based on the above analysis, the selected region is the yellow rectangle drawn in Figure 9.

The region can not only meet the requirements of low-speed stability and small temperature rise but also the blocking torque and mechanical efficiency are in an ideal range. This method is different from others in that it gives priority to speed smoothness and temperature rise as reference points for pre-pressure assessments.

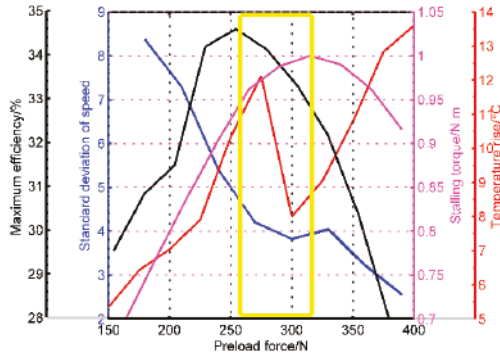


Figure 9. The diagram which interprets the optimization rule of the preload force.

5.2. Speed Control Performances

The validity of the optimization criterion is proved by the speed control performance, which not only stems from speed fluctuations but also reflects the effect of temperature rise. The speed closed-loop control with the target 72°/s is implemented under different preloads from 200 to 400 N. Considering the control target is located in the low-speed section, we select the voltage amplitude as the control parameter, the PID control method is adopted for every control process. Figure 10 displays the respective controlling results. It can be seen that residual control error decreases with the increasing preload forces when the preload force is less than 300 N and the error begins to rise once the pre-pressure exceeds 300 N. These results verify the effectiveness of pre-pressure optimization from one aspect, while other aspects will be further investigated.

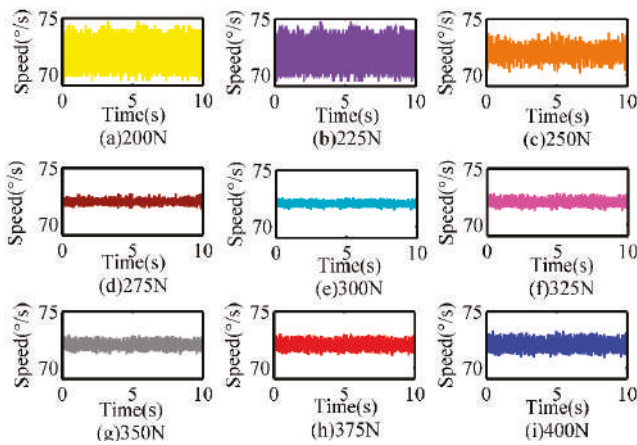


Figure 10. Comparison of the speed control performance under different pre-pressures.

6. Conclusions

Pre-pressure is one of the critical parameters that restrict the performance of an ultrasonic motor. The target of this paper is to comprehensively analyze the sensitivities of motor performances on the pre-pressure and to put forward a targeted optimization method. A simulation model with power dissipation and an integrated experimental facility with the preload adjustment device is adopted to analyze the laws from multiple perspectives. The preload adjustment is mainly designed by an electric cylinder and a pressure sensor, which is first employed in the preload change of the TRUM. Besides the stator/rotor contact state, the inspected properties cover rotor speed stability, near-interface temperature rise and mechanical properties. From these indicators, the speed stability, the temperature rise, the stalling torque, and the maximum efficiency are derived from the test results and drawn in a picture together. The operation makes these four indicators in function of the pre-pressure easy to distinguish in the candidate region according to different application targets. The optimization criterion in this paper contains three principles, which are the lower temperature rise, the smaller speed stability, and the moderate mechanical properties, respectively. Finally, the optimization region of the preload force is determined as [260, 320], and the smaller speed stability error in the optimization area verifies the criterion's validity.

Besides, the contact state under different preloads is interpreted in simulation and experimental tests. This paper first proposes a polynomial formula for transferring the pressure into the contact angle, which helps us measure the interface contact properties indirectly. Therefore the speed fluctuations can be attributed to the contact variation. What should be mentioned that slight fluctuations of the compression preload force will occur during a TRUM's physical life, especially in the application combining high speed with high load. The traditional preload component is a disc spring or thin-copper sheet, which cannot assure the correct imposing pressure in the total life-cycle. Luckily, the zero-stiffness structure similar to that of a PCB motor [30] can be used to ensure the pre-pressure, which will be the future optimization direction for all types of ultrasonic motors.

Author Contributions: N.C. contributed to this work by building the integrated measurement system and the analysis from simulation and experiment; J.Z. contributed to this work with the performance tests of the motor, D.F. contributed to the guidance of the research and the revision of the manuscript. All authors have read and agree to the published version of the manuscript.

Funding: The authors acknowledge the financial supports from the National Basic Research Program of China (973 Program, Grant No.2015CB057503).

Conflicts of Interest: The authors declare no conflict of interest.

Appendix A

The simulation model displayed as a state-space function:

$$\dot{x} = Ax + Bu \quad (\text{A1})$$

In this function:

$$A = \begin{bmatrix} O_{2 \times 2} & I_{2 \times 2} & O_{2 \times 2} & O_{2 \times 2} \\ -k_o/m_o & 0 & -d_o/m_o & 0 \\ 0 & -k_o/m_o & 0 & -d_o/m_o \\ O_{2 \times 2} & O_{2 \times 2} & 0 & 1 \\ O_{2 \times 2} & O_{2 \times 2} & 0 & -d_r/J_r \\ O_{2 \times 2} & O_{2 \times 2} & O_{2 \times 2} & 0 \\ & & & 0 & 0 \\ & & & 0 & -d_z/m_r \end{bmatrix} \quad (\text{A2})$$

$$B^T = \begin{bmatrix} O_{2 \times 2} & 1/m_o & 0 & O_{2 \times 2} & O_{2 \times 2} \\ & 0 & 1/m_o & 0 & 0 \\ O_{2 \times 2} & O_{2 \times 2} & & 1/J_r & 0 \\ & & & 0 & 0 \\ & & & 0 & 1/m_r \end{bmatrix} \quad (A3)$$

$$u = \begin{bmatrix} k_c U_A + \varepsilon k_c U_B + F d n_1 + F d t_1 \\ \varepsilon k_c U_A + k_c U_B + F d n_2 + F d t_2 \\ T_R - T_{load} \\ F_Z - F_N \end{bmatrix} \quad (A4)$$

The critical simulation parameters are listed in the following table.

Table A1. The TRUM60A simulation parameters.

	Description	Value (Units)
N	Number of wavelengths	9
Ro	The average radius of the stator ring	0.02625 (m)
λ	Traveling wavelength	0.0187 (m)
mo	Modal mass of stator elastic body	0.005 (kg)
ko	Modal stiffness of stator elastic body	4.56×10^9 (kg/m ²)
do	Modal damping of stator elastic body	0.05 (N-s/m)
dz	Damping in the axial direction of the rotor	1.5×10^4 (N-s/m)
dr	Damping in the tangential direction of the rotor	5×10^{-4} (N-m-s)
kc	Force factor of piezoelectric ceramics	0.4147 (N/V)
ε	Unbalance coefficient between two-phase voltage	0.02
mr	Rotor mass	0.03 (kg)
Jr	Rotor inertia	7.2×10^{-6} (kg/m ²)
μ	Friction coefficient	0.3
Cp	Capacitance	5.41 (nF)
Rm	Dynamic resistor	149.82 (Ω)
Lm	Dynamic inductance	0.102 (H)
Cm	Dynamic capacitance	16.63 (pF)
Rd	Resumption resistor	31.15 (K Ω)
σ	Speed drop coefficient with the decreasing torque	9.9484 (rad/(N-m-s))
h	The thickness of the friction layer	0.5 (mm)
S	Motor surface area	0.02366 (m ²)
α	Coefficient of heat transfer	10

References

1. Qiu, Y.Q.; Wang, H.; Demore, C.E.M.; Hughes, D.A.; Glynn-Jones, P.; Gebhardt, S.; Bolhovitins, A.; Poltarjonoks, B.; Weijer, K.; Schönecker, A.; et al. Acoustic Devices for Particle and Cell Manipulation and Sensing. *Sensors* **2014**, *14*, 14806–14838. [[CrossRef](#)] [[PubMed](#)]
2. Liang, W.; Ma, J.; Tan, K.K. Contact force control on soft membrane for an ear surgical device. *IEEE Trans. Ind. Electron.* **2018**, *65*, 9593–9603. [[CrossRef](#)]
3. Shokrollahi, P.; James, M.D.; Goldenberg, A.A. Measuring the Temperature Increase of an Ultrasonic Motor in a 3-Tesla Magnetic Resonance Imaging System. *Actuators* **2017**, *62*, 20. [[CrossRef](#)]
4. Flueckiger, M.; Bullo, M.; Chapuis, D.; Gassert, R.; Perriard, Y. FMRI compatible haptic interface actuated with traveling wave ultrasonic motor. In Proceedings of the IEEE Industry Applications Conference Fortieth IAS Annual Meeting, Kowloon, Hong Kong, China, 2–6 October 2015.
5. Chapuis, D.; Gassert, R.; Burdet, E.; Bleuler, H. Hybrid ultrasonic motor and electrorheological clutch system for MR-compatible haptic rendering. In Proceedings of the IEEE/RSJ International Conference on Intelligent Robots & Systems, Beijing, China, 9–15 October 2006.
6. Liu, Y.X.; Xu, D.M.; Yu, Z.Y.; Yan, J.P.; Yang, X.H.; Chen, Y.S. A Novel Rotary Piezoelectric Motor Using First Bending Hybrid Transducers. *Appl. Sci.* **2015**, *5*, 472–484. [[CrossRef](#)]
7. Li, H.Y.; Wang, L.; Cheng, T.H. A High-Thrust Screw-Type Piezoelectric Ultrasonic Motor with Three-Wavelength Exciting Mode. *Appl. Sci.* **2016**, *12*, 442. [[CrossRef](#)]

8. Shao, S.J.; Shi, S.J.; Chen, W.S.; Liu, J.K. Research on a Linear Piezoelectric Actuator Using T-Shape Transducer to Realize High Mechanical Output. *Appl. Sci.* **2016**, *6*, 103. [[CrossRef](#)]
9. Oh, J.H.; Yuk, H.S.; Lim, J.N.; Lim, K.J.; Park, D.H.; Kim, H.H. An analysis of the resonance characteristics of a traveling wave types ultrasonic motor by applying a normal force and input voltage. *Ferroelectrics* **2009**, *378*, 135–143. [[CrossRef](#)]
10. Wang, L.; Liu, J.K.; Lin, Y.X.; Tian, X.Q.; Yan, J.P. A novel single-mode linear piezoelectric ultrasonic motor based on asymmetric structure. *Ultrasonics* **2018**, *89*, 137–142. [[CrossRef](#)] [[PubMed](#)]
11. Wang, J.; Hu, X.X.; Wang, B.; Guo, J.F. A novel two-degree-of-freedom spherical ultrasonic motor using three traveling-wave type annular stators. *J. Cent. South Univ.* **2015**, *22*, 1298–1306. [[CrossRef](#)]
12. Zhang, X.; Zhang, G.; Nakamura, K.; Ueha, S. A robot finger joint driven by the hybrid multi-DOF piezoelectric ultrasonic motor. *Sens. Actuators A Phys.* **2011**, *169*, 206–210. [[CrossRef](#)]
13. Pirrotta, S.; Sinatra, R.; Meschini, A. Evaluation of the effect of preload force on resonance frequencies for a traveling wave ultrasonic motor. *IEEE Trans. Ultrason. Ferroelectr. Freq. Control* **2006**, *53*, 746–753. [[PubMed](#)]
14. Li, J.; Liu, S.; Qu, J.; Cui, Y.; Liu, Y. A contact model of traveling-wave ultrasonic motors considering preload and load torque effects. *Int. J. Appl. Electromagnet Mech.* **2018**, *56*, 151–164. [[CrossRef](#)]
15. Chen, C.; Zhao, C.S. A novel semi-analytical model of the stator of TRUM based on dynamic substructure method. In Proceedings of the USE 2005, The 26th Symposium on ULTRASONIC ELECTRONICS, Tokyo, Japan, 16–18 November 2005; pp. 17–25.
16. Zhao, C.S.; Chen, C.; Zeng, J.S. A New Modeling of Traveling Wave Type Rotary Ultrasonic Motor Based on Three-Dimension Contact Mechanism. In Proceedings of the 2005 IEEE International Ultrasonic Symposium, Rotterdam, The Netherlands, 15–16 October 2005.
17. Zhang, D.; Wang, S.; Xiu, J. Piezoelectric parametric effects on wave vibration and contact mechanics of traveling wave ultrasonic motor. *Ultrasonics* **2017**, *81*, 118–126. [[CrossRef](#)] [[PubMed](#)]
18. Bullo, M.; Perriard, Y. Influences to the mechanical performances of the traveling wave ultrasonic motor by varying the prestressing force between stator and rotor. In Proceedings of the IEEE Symposium on Ultrasonics, Honolulu, HI, USA, 5–8 October 2003.
19. Tavallaei, M.; Atashzar, S.F.; Drangova, M. Robust Motion Control of Ultrasonic Motors under Temperature Disturbance. *IEEE Trans. Ind. Electron.* **2016**, *63*, 2360–2368. [[CrossRef](#)]
20. Moal, P.L.; Cusin, P. Optimization of traveling wave ultrasonic motors using a three-dimensional analysis of the contact mechanism at the stator–rotor interface. *Eur. J. Mech. A. Solids* **1999**, *18*, 1061–1084. [[CrossRef](#)]
21. Yano, Y.; Iida, K.; Sakabe, T.; Yabugami, K.; Nakata, Y. Approach to speed control using temperature characteristics of ultrasonic motor. In Proceedings of the 2004 47th Midwest Symposium On Circuits And Systems, MWSCAS '04, Hiroshima, Japan, 25–28 July 2004.
22. Mashimo, T. Miniature preload mechanisms for a micro ultrasonic motor. *Sens. Actuators A Phys.* **2017**, *257*, 106–112. [[CrossRef](#)]
23. Zhao, C. *Ultrasonic Motors: Technologies and Applications*; Springer Science & Business Media: Berlin/Heidelberg, Germany, 2011.
24. Abdullah, M.; Takeshi, M. Efficiency optimization of rotary ultrasonic motors using extremum seeking control with current feedback. *Sens. Actuators A Phys.* **2019**, *289*, 26–33.
25. El, G.N. Hybrid Modelling of a Traveling Wave Piezoelectric Motor. Ph.D. Thesis, Aalborg University, Aalborg, Denmark, 2000.
26. Ren, W.H.; Lin, Y.; Ma, C.C.; Li, X.; Zhang, J. Output performance simulation and contact analysis of traveling wave rotary ultrasonic motor based on ADINA. *Comput. Struct.* **2019**, *216*, 15–25. [[CrossRef](#)]
27. Kai, J. Dynamic Modeling of Traveling Wave Motor and the Optimal Control of Vibration Mode Vector. Ph.D. Thesis, Hebei University of Technology, Tianjin, China, 2016. (In Chinese).
28. Lu, X.; Hu, J.; Zhao, C. Analyses of the temperature field of traveling-wave rotary ultrasonic motors. *IEEE Trans. Ultrason. Ferroelectr. Freq. Control* **2011**, *58*, 2708–2719. [[CrossRef](#)] [[PubMed](#)]

29. Chen, N.; Qi, C.; Zheng, J.J.; Fan, D.; Fan, S. Impedance Characteristics Test of Ultrasonic Motor Based on Labview and FPGA. In Proceedings of the CSAA/IET International Conference on Aircraft Utility Systems (AUS 2018), Guiyang, China, 19–22 June 2018.
30. PCB Motor Inc. PCB Motor Starter Kit User Guide. Available online: <http://ww1.microchip.com/downloads/en/devicedoc/mcskuserguide75015a.pdf> (accessed on 4 April 2020).



© 2020 by the authors. Licensee MDPI, Basel, Switzerland. This article is an open access article distributed under the terms and conditions of the Creative Commons Attribution (CC BY) license (<http://creativecommons.org/licenses/by/4.0/>).

Article

On-Line Monitoring of Pipe Wall Thinning by a High Temperature Ultrasonic Waveguide System at the Flow Accelerated Corrosion Proof Facility

Se-beom Oh ^{1,2,*}, Yong-moo Cheong ¹, Dong-jin Kim ¹ and Kyung-mo Kim ¹

¹ Nuclear Materials Research Division, Korea Atomic Energy Research Institute, 989-111, Daedeok-daero, Yuseong-gu, Daejeon 34057, Korea; ymcheong@kaeri.re.kr (Y.-m.C.); djink@kaeri.re.kr (D.-j.K.); kmkim@kaeri.re.kr (K.-m.K.)

² Department of Materials Science and Engineering, Dankook University, 119, Dandae-ro, Dongnam-gu, Cheonan 31116, Korea

* Correspondence: sbfull1269@gmail.com

Received: 10 March 2019; Accepted: 8 April 2019; Published: 12 April 2019

Abstract: Pipe wall thinning and leakage due to flow accelerated corrosion (FAC) are important safety concerns for nuclear power plants. A shear horizontal ultrasonic pitch/catch technique was developed for the accurate monitoring of the pipe wall-thickness. A solid couplant should be used to ensure high quality ultrasonic signals for a long operation time at an elevated temperature. We developed a high temperature ultrasonic thickness monitoring method using a pair of shear horizontal transducers and waveguide strips. A computer program for on-line monitoring of the pipe thickness at high temperature was also developed. Both a conventional buffer rod pulse-echo type and a developed shear horizontal ultrasonic waveguide type for a high temperature thickness monitoring system were successfully installed to test a section of the FAC proof test facility. The overall measurement error was estimated as $\pm 15 \mu\text{m}$ during a cycle ranging from room temperature to $150 \text{ }^\circ\text{C}$. The developed waveguide system was stable for about 3300 h and sensitive to changes in the internal flow velocity. This system can be used for high temperature thickness monitoring in all industries as well as nuclear power plants.

Keywords: high temperature pipe; pipe wall thinning; flow accelerated corrosion

1. Introduction

During the operation of nuclear power plants, the thickness of the piping decreases over time which is known as pipe wall thinning. If the reduced thickness is concentrated on one side, the piping could be damaged by the pressure in the pipe, and an internal solution may cause a leak. Pipe wall thinning is mainly caused by FAC (flow accelerated corrosion). FAC occurs mostly in carbon steel pipes, in which the pipe thickness gradually decreases as the Fe ions on the surface of the carbon steel pipe are released. Because pipe wall thinning due to FAC is very slow (a few tens of μm per one year), it is necessary to monitor the piping walls for delamination, cracks and leaks as well as the piping thickness with very high accuracy. This is one of the important issues in the structural stability of a system, which requires continuous monitoring [1–5]. Presently, an ultrasonic method is used, which is one of the nondestructive inspection techniques for measuring the piping wall thickness. The ultrasonic technique is widely used to assess the safety of nuclear piping and to measure the piping wall thickness. Manual ultrasonic methods are generally used to measure the pipe thickness. However, the manual ultrasonic technique has several disadvantages in nuclear power plants. First, the inspection areas of a nuclear power plant are at high temperatures and highly radioactive. Second, the power plant must be shut down and the insulator removed before the thickness of a pipe can be measured because

the transducer must be in direct contact with the pipe surface. When the measurement is completed, it is necessary to install the insulation again, so the shutdown time will be longer. Therefore, if the shutdown of the power plant time is prolonged, it will lead to a loss in power production. This process is inconvenient because it is repeatedly measured during a period of time to assess its structural health. Third, the manual ultrasonic thickness measurement method has a low reliability. The accuracy decreases depending on the operator's skill or condition, the measuring instrument, temperature, the ultrasonic coupling, and the difference in data reading conditions. Therefore, it is necessary to have a stable thickness measurement method for a high temperature and highly radioactive environment without having to stop the operation of the nuclear power plant.

Measuring the thickness of high-temperature piping using ultrasonic waves has several problems that have not been solved. In the case of a nuclear power plant, the temperature of the fluid flowing inside the pipe increases to about 200 °C. At this time, the piping temperature is up to about 150 °C, and the difference in thermal expansion between each of the piezoelectric and coupling materials may cause errors in the thickness measurements. Conventional piezoelectric materials depolarize if they rise above the Curie temperature; thus, current ultrasonic thickness measurement techniques cannot be used at high temperatures above 200 °C [6–8].

To solve this problem, a method for installing a buffer rod system and a waveguide method are currently being studied. The buffer-rod system has the advantage of using the existing longitudinal wave transducer; however, it has a disadvantage that it cannot perfectly protect the piezoelectric element from the high temperature piping because the buffer-block is short, and the distance from the specimen is not long. The ultrasonic waveguide system can be used to protect the piezoelectric element from high temperature piping by using a long thin plate to keep the piezoelectric element away from the test specimen [9–14]. In this method, the ultrasonic dispersion characteristics in the guide should be considered because the ultrasonic wave propagates through the waveguide [15]. The shear horizontal vibration mode can be used because there is no dispersion characteristic when the wave propagates in the plate. Based on these techniques, we developed a pipe wall thinning monitoring system using a shear horizontal ultrasonic transducer and waveguide strip. Clamping devices were designed and installed with a solid coupling material for safe acoustic contact between the waveguide strip and the pipe surface. The shear horizontal waveguide and clamping device provided an excellent S/N ratio and high measurement accuracy for long time exposure at high temperature conditions.

2. Issue of High-Temperature Ultrasonic Thickness Measurements

The ultrasonic thickness measurement principle is usually performed by measuring the flight time between continuous echoes in the time domain. The thickness of the specimen can be determined by calculating the material flight time of the waves and the known ultrasonic velocity values. Assuming that there is minimal ultrasonic dispersion, a sharper ultrasonic signal will increase the resolution of the measurement, and in general is the most accurate way to perform the temporal measurement by measuring the peak to peak time or the perform pulse-echo overlap [16]. Pipe wall thinning of carbon steel pipes in nuclear power plants occurs at several tens of micrometers per year, thus the measurement errors should be minimized. Several factors have been discussed as ways to overcome these errors [17]. First, environmental factors cause errors due to the geometric factors of the piping such as surface roughness, specimen curvature and contact pressure between the coupling material and the transducer as well as ultrasonic velocity errors in the specimen due to changes in the temperature. Thus, the device should be calibrated, and the surface condition should be maintained to minimize measurement errors. Second, there are errors due to the transducer performance and signal processing, such as measurement conditions between the transducer and the specimen, the performance of the analog-to-digital converters and delays caused by digital signal processing, respectively [18].

Typical piezoelectric ceramic elements are exposed to temperatures higher than the Curie temperature resulting in depolarization of the element, which then loses its piezoelectric properties making it difficult to accurately measure the signal. The signal quality of the piezoelectric

vibrator degrades, and the error in determining the peak position of the signal may increase as the temperature varies. It is necessary to improve the acoustic contact condition between the transducer and the specimen by minimizing the deterioration of the probe at high temperatures. Third, there is a problem with the couplant. For a high temperature pipe, the couplant used at room temperature will evaporate, resulting in an error on the contact surface. Stable ultrasonic sound effect was maintained by using a special high temperature couplant that does not evaporate even in an environment of 150 °C. A dry couplant (gold plate) was used between the waveguide strip and the surface of pipe to minimize the error due to thermal expansion. The gold plate can minimize errors due to thermal expansion between the two objects by constantly maintaining its shape of the coefficient at high temperatures.

3. Ultrasonic On-Line Monitoring System for Measuring Wall Thinning of High Temperature Pipe

The conventional buffer-rod type system is widely used as a technique for measuring the thickness of high temperature test specimens. It can be used by inserting a buffer block between the ultrasonic transducer and the specimen shown in Figure 1a. The material of the buffer block should be acoustically stable, should not deform at high temperatures, and should protect the transducer. Glycerin or machine oil used in conventional ultrasonic couplings does not work properly at high temperatures. Therefore, a special solid material coupling, such as a thin gold plate, was used to maintain good acoustic contact between the buffer rod and the specimen. The advantage is that it minimizes the difference in thermal expansion between the buffer rod materials and the specimen, which can be maintained for long periods of the test. Figure 1b shows a buffer-rod type high temperature ultrasonic transducer assembled in a test pipe for thickness monitoring.

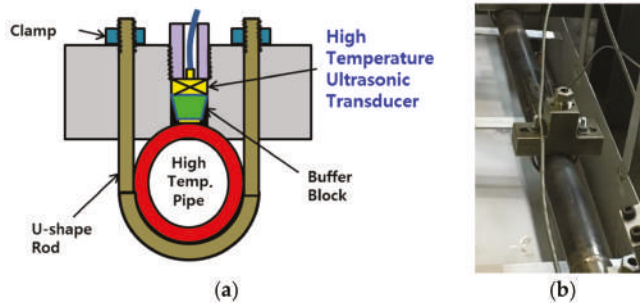


Figure 1. (a) An assembly drawing diagram of a high temperature pipe using a buffer-rod type measurement system; (b) an installed buffer-rod type system for thickness monitoring on a pipe.

Another approach to measure pipe thickness at high temperatures is to use an ultrasonic waveguide strip. This improved method was attempted using a waveguide strip to reduce the acoustic parameters between the ultrasonic transducer and the specimen. A pair of shear horizontal transducers and a long waveguide strip were designed and manufactured. The shear horizontal vibration mode was chosen to ensure that there was proper ultrasonic wave transmission at the thin strips. The shear horizontal mode had sharp and clear ultrasonic signals within a certain frequency range because there was low dispersion in the plate. This vibration mode is advantageous for obtaining sensitive and accurate experimental data at high temperatures [19]. The shear horizontal wave transducer was attached to the edge of the waveguide strip shown in Figure 2. When the transducer and the waveguide strip contacted each other exactly at a perpendicular level, the shear horizontal mode was stably transmitted to the waveguide. On the opposite side of the waveguide strip, a clamping device was designed and fabricated to precisely hold the specimen, and two waveguide strips were installed in parallel to divide the transmitter and receiver. A thin solid plate (gold plate) was used as a couplant between the waveguide strip and the test specimen similar to the buffer-rod system. The transducer

used a waveguide strip that was far from the specimen, which was maintained at about 35 °C when the temperature of the pipe was 150 °C. This meant that the developed system completely freed the transducer from the constraints of high temperatures. The waveguide pitch/catch method using two waveguide strips can increase the S/N ratio compared to the pulse/echo technique. Two strips were used to set up the waveguide system device. A transducer was connected to each strip, one on the transmitting transducer and the other on the receiving transducer. The two strips were spaced 1 mm apart to filter the noise received at the surface of the pipe to be measured. If the strip is placed at 1 mm, it measured only the wanted signal because of the time difference between the signal transmitted to the pipe surface, and the signal reflected from the opposite side of the pipe. Because it received a signal only from the piping specimen, noise from undesired reflections at the end of the strip were prevented. This method had no main bang signal, and the signal reflected from the end of the waveguide strip was very small. Additionally, the multiple reflected signals on the back wall of the pipe, which was to be inspected, had a high S/N ratio.

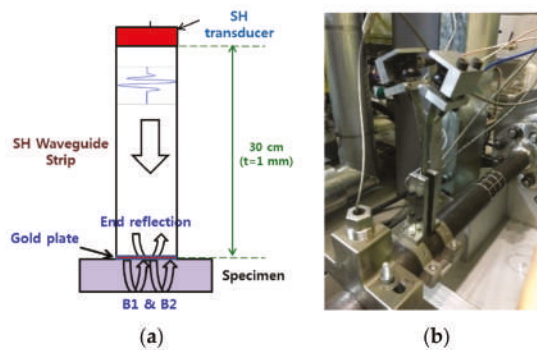


Figure 2. (a) Conceptual diagram of a pair of waveguide strips for high temperature thickness monitoring; (b) installed waveguide system for thickness monitoring on a pipe.

4. High Temperature Pipe Thickness Measuring Program

The thickness measurement program was designed as a moving gate in real time to accurately measure the reflected flight time. The first gate was set to the signal from the end of the transmitting waveguide strip shown in Figure 3. The second gate was set to the first back wall echo signal, and the third gate was set to the second back wall echo signal. The second and third gates were set as the moving gates to follow the first gate setting. The moving gate moves along with the movement of the rf signal according to the noise or the temperature change, making it possible to measure the peak to peak signal stably. The peak of the first and second back wall echoes were automatically determined by the flight time and denoted as t_1 and t_2 shown in Figure 3. The ultrasonic wave velocity was constant and the path length of the actual reciprocating wave can be seen by the strip and pipe wall thickness. Thus, the time of the received rf signal can be calculated. The shear horizontal wave velocity of the carbon steel is about 3300 m/s, and the flight time reflected by the waveguide strip 300 mm in length is calculated to be 170 μ s. The flight time between the first back wall and the second back wall of a 5.54 mm thick pipe is estimated to be about 3.2 μ s. All ultrasonic rf (radio frequency) waveforms are in the time domain and displayed on the PC screen. Moreover, this system inspects the signal quality and is designed to display an alarm indicator on the screen when receiving unwanted signals. Between t_1 and t_2 , the flight time was automatically calculated on average, hundreds of times to obtain accurate thickness data. Because ultrasonic velocity is a function of temperature, variation in the ultrasonic velocity at high temperatures can be a main problem in terms of measurement data errors. Therefore, to measure the thickness in real time at high temperature, pre-calibration is required to reflect the relationship between the ultrasonic velocity and the temperature.

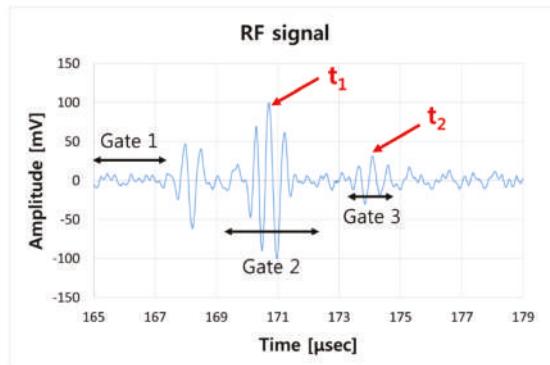


Figure 3. Typical ultrasonic rf signals by a developed waveguide with the pitch/catch method at 150 °C.

The ultrasonic velocity can be determined as a function of the temperature by measuring the variation in the velocity with a temperature change in the material to be measured. Figure 4 shows the measurement data of the shear mode wave velocity in a carbon steel pipe based on a variation in the temperature. The velocity of the ultrasonic waves was measured by heating the same materials pipe as the pipe used in the FAC proof facility to the furnace from 0 to 250 °C. The pipe thickness did not change when measuring the sound velocity change by calculating the time of the received signal according to the temperature change [20]. This function was entered into the thickness measurement program to reduce the error due to the temperature variation.

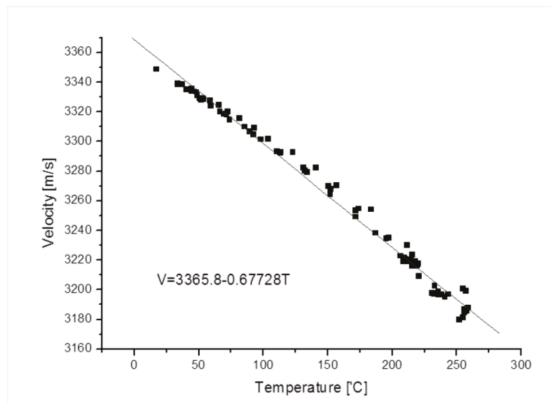


Figure 4. Calibration of the shear horizontal wave velocity with varying temperatures for a carbon steel pipe SA 106.

5. Verification Experiment in the FAC Proof Facility and Results

The FAC demonstration test facility was manufactured to operate in the same environment as a nuclear power plant. This facility is designed to operate for 1200 h at high temperatures at more than 150 °C, per one cycle and with the adjustable pH, DO, and flow rate for the fluid flowing inside the piping. To measure pipe wall thinning, we prepared a test section with the insulation removed from part of the facility. This section is made of carbon steel (SA 106), and the pipe has an outer diameter of 60.4 mm, a wall thickness of 5.54 mm and a length of 750 mm. The chemical composition of the materials is shown in Table 1. The pipe thickness was measured by the buffer-rod type system and an ultrasonic waveguide high temperature thickness monitoring system. The two systems were installed on the surface of the carbon steel pipe to compare the signals from each other, as shown in Figure 5.

Prior to the experiment, the thickness measurement error was confirmed according to the temperature variation for the stability and accuracy of the system. Figure 6 shows the actual measured waveguide system data. A provisional thickness error range was determined by increasing the temperature of the same material pipe to 200 °C and measuring the change in thickness during the cooling process. The range of the thickness measurement error was $\pm 15 \mu\text{m}$ while the pipe was heated to 0~150 °C and then cooled. These devices were able to acquire ultrasonic signals which were reliable for a long time at high temperatures, and the flight times of the signals through calculations were converted to the thickness of the pipe. Minimizing the measurement errors was possible with normalization of the signal amplitude, the automatic setting of the ultrasonic flight time and moving the gate control by applying a temperature compensation factor. The pipe thickness data were directly compared with the measured data at room temperature during the rest period to determine the reliability of the measured data.

Table 1. The chemical composition of the material (SA 106 Gr. B).

Material	Cr	Mo	Cu	Mn	Ni	Si	C	P	S
SA106 Gr. B	0.02	0.01	0.04	0.37	0.02	0.22	0.19	0.008	0.006



Figure 5. Test section in the flow accelerated corrosion (FAC) facility (left) and another type system installed at a test section (right).

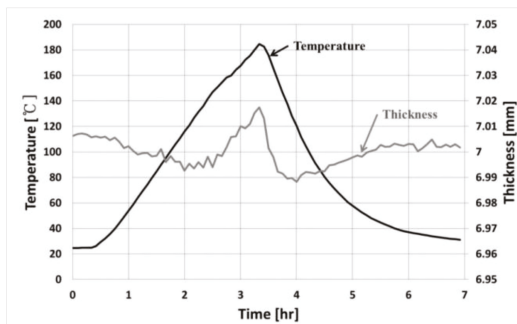


Figure 6. The measurement error by temperature variation in the developed system.

Figure 7 shows the change in the slope of the wall thickness reduction with the flow rate in the waveguide system. This developed system measured the tendency of pipe wall thinning by changing the flow rates from 7 to 10 to 12 m/s every 1100 h. The blue line is the data measured in real time once every hour. The red line slope indicated the FAC rate in each section. As the flow rate increased, the FAC rate became faster and the FAC rate decreased as the flow rate decreased. As the flow rate increased from 7 m/s to 12 m/s, the wall thickness reduction rate also increased. This result meant

that is possible to predict the change in the flow rate inside the pipe by analyzing the rate of pipe wall thinning.

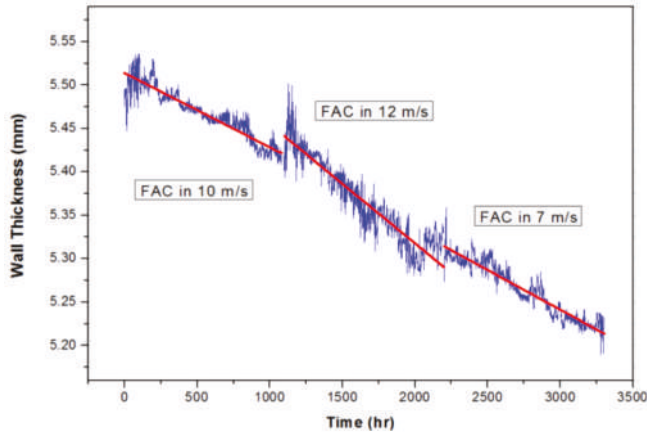


Figure 7. Pipe wall-thickness monitoring of carbon steel piping in the flow accelerated corrosion proof test facility: Different wall-thinning ratios observed depending on the flow velocities.

Figure 8 shows the pipe wall thinning measurement data from approximately 3300 h of operation using the buffer-rod and developed waveguide systems. The temperature of the fluent flowing inside the pipe was maintained at 150 °C, and both devices measured the wall thickness reduction of about 260 μm. The blue line in Figure 8 is the data of thickness thinning of buffer-rod type commercial equipment. From the point at which the flow rate increased from 10 m/s to 12 m/s, it can be seen that the thickness thinning rate tendency was less than that of the developed equipment. Furthermore, although the flow velocity slowed to 7 m/s at a large velocity of 12 m/s, but the buffer-rod type system was measured to show that the thickness reduction rate was increasing. On the other hand, the red line is measuring data by the developed waveguide system. The thickness reduction rate was measured to suit the change in the flow rate. It is possible to compare more clearly converted (mm/year) for the thickness reduction for each period. As the flow rate inside the piping increased, the rate of the pipe wall thinning increased. The developed waveguide system showed more accurate reduction trends as the flow rate changed. The developed waveguide system operated stably at a temperature cycle of 150 °C for a long time, and the measurement error was about ±20 μm.

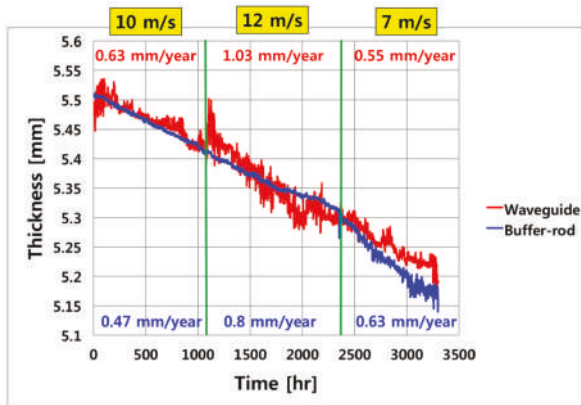


Figure 8. The pipe thickness measurement data using the buffer-rod and waveguide type systems.

Figure 9 shows the result of the manual UT measurement at room temperature. A total of six points were set in the same direction as the position where the two systems were installed, and measurements were made at room temperature. Reliable comparative data measures exactly at the same point, but there was an error generated by removing and reinstalling real-time measuring equipment. Measuring the six zones from A to F next to the point where two pieces of equipment were installed (see Figure 10). A total of six points were measured 10 times and averaged in order to increase the accuracy. The equipment used for the measurement was 38DL PLUS (OLYMPUS). The tendency of the thickness reduction measured with the manual room temperature UT was very similar to that for the high temperature on-line UT system. The reliability of the developed waveguide system was verified by comparing the conventional buffer-rod system and the manual room temperature UT.

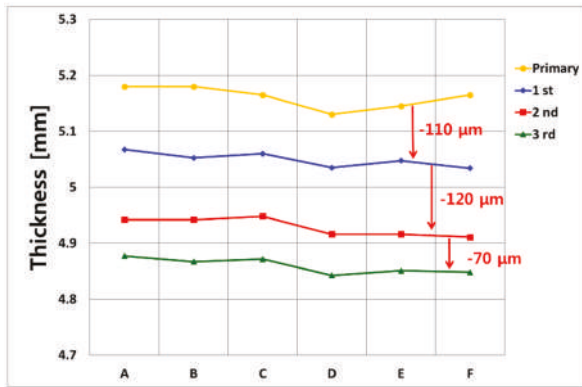


Figure 9. The thickness measurement result of the manual ultrasonic testing (UT) at room temperature.

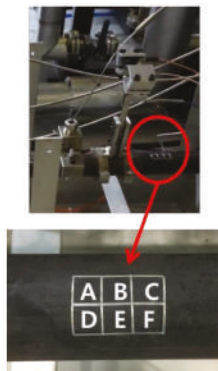


Figure 10. A grid for measuring ultrasonic testing at room temperature in the same direction next to two installed systems.

6. Conclusions

A shear horizontal ultrasonic pitch/catch waveguide system was developed for the accurate online monitoring of the pipe wall thickness in the FAC certification test facility. A clamping device was designed and installed for the gold-plate contact between the end of the waveguide strip and the pipe surface. A computer program was developed for online monitoring of the pipe thickness at high temperatures. The system minimized measurement errors by controlling the moving gate with temperature deviation, normalizing the signal amplitude, automatically determining the ultrasonic flight time and including a temperature compensation function. The buffer-rod and ultrasonic

waveguide high temperature ultrasonic thickness monitoring systems were successfully installed in the test section of the FAC test facility. These systems were confirmed as a stable operation with an error of $\pm 20 \mu\text{m}$ in temperature cycles up to $150 \text{ }^\circ\text{C}$ for 3300 h, and performed better than other similar measurement systems. In addition, the developed waveguide system was able to predict the velocity of the fluid flowing inside the pipe by analyzing the thickness reduction rate.

Finally, it was confirmed that the thickness reduction measurement was very accurate in comparison with the room temperature UT results. This result demonstrates that a waveguide system is sensitive to the flow of internal fluids and can measure thickness better than that of commercial systems. This system can be applied to high temperature thickness monitoring in all industries as well as nuclear power plants.

Author Contributions: S.-b.O. conducted the signal measurement, data analysis and wrote the manuscript; Y.-m.C. provided analysis cooperation and reviewed the manuscript; D.-j.K. supervised this study; K.-m.K supervised this study.

Funding: This work was supported by a Korean Atomic Energy Research Institute (KAERI) Grant funded by the Korean government (Ministry of Science, ICT, and Future Planning).

Acknowledgments: This work was supported by a Korean Atomic Energy Research Institute (KAERI) Grant funded by the Korean government (Ministry of Science, ICT, and Future Planning) and the National Research Foundation of Korea (NRF) Grant funded by the Korean government (2017M2A8A4015158).

Conflicts of Interest: The authors declare no conflict of interest.

References

- Cheong, Y.M.; Kim, K.M.; Kim, D.J. High-Temperature Ultrasonic Thickness Monitoring for a Pipe Thinning in FAC Proof Test Facility. *Nuclear Eng. Technol.* **2017**, *49*, 1463–1471. [[CrossRef](#)]
- Dooley, R.B.; Chexal, V.K. Flow-accelerated corrosion of pressure vessels in fossil plants. *Int. J. Press. Vessels Pip.* **2000**, *77*, 85–90. [[CrossRef](#)]
- Choi, Y.H.; Kang, S.C. Evaluation of Piping Integrity in Thinned Main Feedwater Pipes. *Nucl. Eng. Technol.* **2000**, *32*, 67–76.
- Kim, D.; Cho, Y.; Lee, J. Assessment of Wall-Thinning in Carbon Steel Pipe by Using Laser-generated Guided Wave. *Nucl. Eng. Technol.* **2010**, *42*, 546–551. [[CrossRef](#)]
- Chung, H.S. A Review of CANDU Feeder Wall Thinning. *Nucl. Eng. Technol.* **2010**, *42*, 568–575. [[CrossRef](#)]
- Baba, A.; Searfass, C.T.; Tittermann, B.R. High Temperature Ultrasonic Transducer up to $1000 \text{ }^\circ\text{C}$ using Lithium Niobate Single Crystal. *Appl. Phys. Lett.* **2010**, *97*, 232901.
- Wu, K.T.; Kobayashi, M.; Jen, C.K. Integrated High-temperature Piezoelectric Plate Acoustic Wave Transducers Using Mode conversion. *IEEE Trans. Ultrason. Ferroelectr. Freq. Control.* **2009**, *56*, 1218–1224. [[PubMed](#)]
- Megrèche, A.; Lebrun, L.; Troccaz, M. Materials of $\text{Bi}_4\text{Ti}_3\text{O}_{12}$ Type for High Temperature Acoustic Piezo-sensors. *Sens. Actuators A* **1999**, *78*, 88–91. [[CrossRef](#)]
- Carandente, R.; Lovstad, A.; Cawley, P. The Influence of Sharp Edges in Corrosion Profiles on the Reflection of Guided Waves. *NDT&E Int.* **2012**, *52*, 57–68.
- Zhou, W.J.; Ichchou, M.N.; Mencik, J.M. Analysis of Wave Propagation in Cylindrical Pipes with Local Inhomogeneities. *J. Sound Vib.* **2009**, *319*, 335–354. [[CrossRef](#)]
- Nurmalia, N.; Nakamura, H.; Ogi, M.; Hirao, K. Nakahata, Mode Conversion Behavior of SH Guided Wave in a Tapered Plate. *NDT&E Int.* **2012**, *45*, 156–161.
- Honarvar, F.; Salehi, F.; Safavi, V.; Mokhtari, A.; Sinclair, A.N. Ultrasonic Monitoring of Erosion/Corrosion Thinning Rates in Industrial Piping systems. *Ultrasonics* **2013**, *53*, 1251–1258. [[CrossRef](#)] [[PubMed](#)]
- Kazys, R.; Voleisis, V.; Voleisiene, B. High Temperature Ultrasonic transducer: Review. *Ultrasound* **2008**, *63*, 7–17.
- Francis, L.A.; Friedt, J.M.; Bertrand, P. Influence of Electromagnetic Interferences on the Mass Sensitivity of Love Mode Surface Acoustic Wave Sensors. *Sens. Actuators A* **2005**, *123*, 360–369. [[CrossRef](#)]
- Cheong, Y.M.; Kim, H.P.; Lee, D.H. A Shear Horizontal Waveguide Technique for Monitoring of High Temperature Pipe Thinning. In Proceedings of the 2014 Spring Meeting of the KNS, Jeju, Korea, 28–30 May 2014.
- Dixon, S.; Edwards, C.; Palmer, S.B. High Accuracy Non-contact Ultrasonic Thickness Gauging of Aluminum Sheet using electromagnetic Acoustic Transducers. *Ultrasonics* **2001**, *39*, 445–453. [[CrossRef](#)]

17. Maio, L.; Ricci, F.; Memmolo, V.; Monaco, E.; Boffa, N.D. Application of laser Doppler vibrometry for ultrasonic velocity assessment in a composite panel with defect. *Compos. Struct.* **2018**, *184*, 1030–1039. [\[CrossRef\]](#)
18. Cheong, Y.M.; Kim, H.N.; Kim, H.P. An Ultrasonic Waveguide Technique for On-line Monitoring of the High Temperature Pipe Thinning. In Proceedings of the Transactions of the Korean Nuclear Society Spring Meeting, Jeju, Korea, 29–30 May 2014.
19. Celga, F.B.; Cawley, P.; Allin, J.; Davies, J. High-temperature (>500 °C) Wall Thickness Monitoring Using Dry-coupled Ultrasonic Waveguide transducers. *IEEE Trans. Ultrason. Ferroelectr. Freq. Control.* **2011**, *58*, 156–167.
20. Cheong, Y.M.; Kim, J.H.; Hong, J.H.; Jeong, H.K. Measurement of Dynamic Elastic Constants of RPV Steel Weld due to Localized Microstructural Variation. *J. Korean Soc. Non-Destruct. Test.* **2001**, *20*, 559–564.



© 2019 by the authors. Licensee MDPI, Basel, Switzerland. This article is an open access article distributed under the terms and conditions of the Creative Commons Attribution (CC BY) license (<http://creativecommons.org/licenses/by/4.0/>).

Article

A Low-Cost Continuous Turbidity Monitor

David Gillett ¹ and Alan Marchiori ^{2,*}¹ Department of Chemical Engineering, Bucknell University, Lewisburg, PA 17837, USA² Department of Computer Science, Bucknell University, Lewisburg, PA 17837, USA

* Correspondence: amm042@bucknell.edu; Tel.: +1-570-577-1751

Received: 31 May 2019; Accepted: 8 July 2019; Published: 10 July 2019

Abstract: Turbidity describes the cloudiness, or clarity, of a liquid. It is a principal indicator of water quality, sensitive to any suspended solids present. Prior work has identified the lack of low-cost turbidity monitoring as a significant hurdle to overcome to improve water quality in many domains, especially in the developing world. Low-cost hand-held benchtop meters have been proposed. This work adapts and verifies the technology for continuous monitoring. Lab tests show the low-cost continuous monitor can achieve 1 nephelometric turbidity unit (NTU) accuracy in the range 0–100 NTU and costs approximately 64 USD in components to construct. This level of accuracy yields useful and actionable data about water quality and may be sufficient in certain applications where cost is a primary constraint. A 38-day continuous monitoring trial, including a step change in turbidity, showed promising results with a median error of 0.45 and 1.40 NTU for two different monitors. However, some noise was present in the readings resulting in a standard deviation of 1.90 and 6.55 NTU, respectively. The cause was primarily attributed to ambient light and bubbles in the piping. By controlling these noise sources, we believe the low-cost continuous turbidity monitor could be a useful tool in multiple domains.

Keywords: turbidity; low-cost; continuous water quality monitor; water

1. Introduction

The United Nations states that high-quality drinking water is at the core of sustainable development and is critical for socioeconomic development, healthy ecosystems, and for human survival itself. It is vital for reducing the global burden of disease and improving the health, welfare, and productivity of human populations. It is central to the production and preservation of a host of benefits and services for people. Water is also at the heart of adaptation to climate change, serving as the crucial link between the climate system, human society, and the environment [1].

Water quality monitoring is the process by which critical characteristics of water (physical, chemical, biological) are measured. Turbidity is one of the most universal metrics of water quality. It is a measure of the cloudiness (the inverse of clarity) of water. In watersheds, the presence of high turbidity can be indicative of both organic and inorganic materials. In the case of organic materials, high turbidity can indicate problems such as increased algae growth caused by fertilizer run-off. In the case of inorganic materials, high turbidity can indicate problems such as high suspended sediment caused by erosion during a rainstorm or water churn caused by high winds. Turbidity is a non-specific measure and therefore alone cannot identify the root cause of water cloudiness. However, under certain conditions, it can be used to estimate certain quantitative parameters such as stream loading, total suspended solids, and soil loss. There is a variety of published research on the effect of turbidity on different organisms and the implications on human drinking water [2–4].

Therefore, turbidity is a useful measure for many water resource management applications. This monitoring can help inform decisions regarding the allocation of funds and what future actions would be the best for a watershed. Presently, the sensors that are used are expensive, typically costing

thousands of dollars. This causes most of the sensors to be owned by companies that communities hire to take samples a small number of times a year. This is far from the best approach as rapid changes in turbidity are indicative of problems. The best time to tackle these problems is right when they occur. With current sampling frequency, these rapid changes are unlikely to be measured and extremely unlikely to have proper actions taken to deal with the root cause of these changes. The key to efficient and proactive water resource management is continuous and accurate monitoring. However, the cost and complexity of deploying such monitoring systems presently limit their use. It is critical that the cost of individual sensors be decreased to make widespread implementations of these monitoring systems feasible. Also, it is critical that the accuracy of these sensors be high enough to provide useful water quality data. Automated continuous sensing would allow the labor cost of water monitoring to decrease substantially as after the initial setup, except for minor ongoing maintenance, the sensors run continuously without human intervention. An automated sensor platform could also be used by people with little, if any, formal training in water monitoring.

Open-source technologies have been identified as the most promising solution to this challenge [5]. As a result, some groups have begun developing their own low-cost monitoring solutions [6–9]. However, these prior works for turbidity monitoring focus on hand-held meters and leave continuous monitoring for future work. Lambrou et al. [10] built a complete continuous monitoring system using off-the-shelf sensors without addressing cost or complexity concerns. Lorena Parra et al. built a low-cost water quality monitoring system for fish farming that contained a simple turbidity sensor [11]. Kofi Sarpong Adu-Manu et al. [12] broadly review methods for water quality monitoring focusing on technologically advanced methods employing wireless sensor networks. In this paper, we present the development of a low-cost continuous turbidity sensor. Our goal is a sensor that could be used in both watershed and drinking water continuous monitoring applications.

2. Related Work

Standard laboratory methods to measure turbidity are well understood and the most commonly used standard is maintained as method 180.1 by the U.S. EPA [13]. This method specifies a tungsten lamp illuminating a sample from not more than 10 cm away with a photo-electric detector oriented 90° from the source. This method is specified from 0–40 nephelometric turbidity units (NTU) with instrument sensitivity of at least 0.02 NTU in water under 1.0 NTU. The NTU units themselves are defined by the response of the nephelometric sensor to known standards. There is no mathematical definition of NTU.

There are at least four other standards for measuring turbidity using nephelometry (ISO 7027, GLI Method 2, Hatch Method 101033, and Standard Methods 2130B) [14]. These variants specify different light sources and detector arrangements. However, none of these standard methods lend themselves to low-cost continuous water quality monitoring. In this work, we follow the general approach of using a light source with a detector located at 90° built using only commonly available electronic components, 3D printable structures, and open-source software with the goal of determining if such a low-cost sensor could be suitable for continuous water quality monitoring applications.

To our knowledge, Christopher Kelly and his team proposed the first low-cost turbidity sensor [8]. This project represents the first publicly available peer-reviewed characterization of an affordable nephelometric turbidimeter. The team set out to create a battery-powered, high accuracy turbidity meter for drinking water monitoring in low-resource communities. This goal required a few design constraints that they set out to meet: run on a single set of batteries for weeks to months of regular use, a high measurement accuracy, and the ability to differentiate small changes in turbidity especially over the range of 0–10 NTU, the sensor must have all of its parts documented and be able to be made by non-experts who want to create their own version of the sensor.

The developed system is a cuvette-based turbidity meter using a single near infrared light emitting diode and a TSL230R light-to-frequency sensor set at 90° apart in a single beam design. This is where there are a single LED emitter and a single receiver perpendicular to the light beam from the LED.

The receiver converts light intensity to a signal that can be read by a microcontroller. The theory behind this design is that the clearer the solution, the more light that makes it straight through the solution. The more turbid the solution, the more light that is reflected perpendicular to the light beam. The meter does not store the data but rather displays it on a LED display for manual recording. Using turbidity standards created using cutting oil and water, the team tested a known turbidity meter next to the created turbidity sensor and measured the readings from both. This data was used to create four calibration curves (each for a different range) that are used to convert the light-to-frequency sensor output from the created turbidity meter to the turbidity reported by the commercial sensor.

The study showed the created turbidity meter had an accuracy within 3% of the commercial sensor or 0.3 NTU whichever is larger over the range of 0.02 NTU to 1100 NTU. They reported that in 8 trials results were within 0.01 NTU for the four turbidity standards under 0.5 NTU. These results support the notion that a low-cost turbidity meter is a possibility; however, more tests to evaluate and verify these results are needed. The proposed next steps as of when the paper was written were to account for thermal fluctuation effects on the turbidity of a solution, minimizing the light leakage into the sensor housing through the external casing, investigating the use of GSM data transmission, and investigating an inline immersible version of the turbidity meter.

Closely related is the optical sensor for sea quality monitoring by Filippo Attivissimo et al. [9]. This sensor is designed to take in situ continuous measurements of chlorophyll fluorescence and turbidity. The sensor has a blue LED, red LED, and photodiode evenly spaced surrounding the water sample. It achieves high sensitivity by using a numeric lock-in amplifier. Preliminary turbidity measurements were made using a solution of milled flour in seawater. Although promising, the results were limited, and the precision of the turbidity measurement was not presented.

Optical fibers can also be employed in the measurement of turbidity and to detect specific organic molecules [15]. Ahmad Fairuz Bin Omar and Mohd Zubir Bin MatJafri present a good overview of the optical properties important for turbidity measurement and a design of an optical fiber turbidimeter [16]. While their design provides laboratory support for the device, the authors state that continued development is needed before it is appropriate for field measurements.

Kevin Murpty et al. also developed a low-cost autonomous optical sensor for water quality monitoring [17]. The device is similar to commercially available turbidity sondes. It contains five color LEDs and a photodiode in a cylindrical sensor body to enable spectral analysis of water quality by submerging the device. Laboratory tests and a field deployment verified the operation of the device. The measurements had high correlation with a commercial turbidity sonde. The system component cost was approximately €650 which is significantly higher than other low-cost systems proposed by others.

3. Appliance Sensors

As a first step to the development of a low-cost continuous turbidity sensor, we evaluated existing commercial low-cost appliance turbidity sensors. These sensors are used in dishwasher and clothes washing machines typically to determine when the contents of the appliance are clean. It was hoped that they would be able to sufficiently determine differences in water clarity to provide useful data for water management applications. Three different turbidity sensors from Amphenol were tested (TST-10, TSD-10, and TSW-10) pictured in Figure 1. All models contain an LED emitter and a phototransistor oriented directly across (180°) from the LED. The output is proportional to the amount of light traveling through the sample and arriving at the phototransistor instead of to the measurement of the scattered light provided by a nephelometric meter. The primary difference between the various models is the mechanical enclosure. The TST-10 is a flow-through design while the TSD-10 is designed to be inserted into the water flow. Either of these could be adapted for continuous monitoring applications.



Figure 1. Amphenol TST-10 (left) and TSD-10 (right). TSW-10 is similar to the TSD-10 (not pictured) (images from Amphenol).

Each sensor was tested using the reference circuit specified in the datasheet [18–20] shown in Figure 2 and recording the voltage output of the sensor using an Arduino Mega’s internal analog to digital converter. The more light that is transmitted through the sample to the receiver the higher the output voltage. This higher voltage means the solution is clearer which is equivalent to saying that it has lower turbidity.

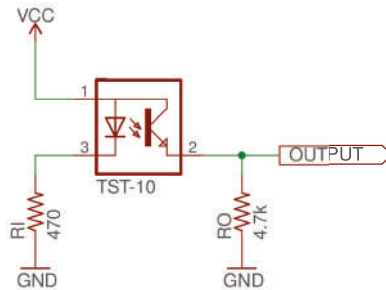


Figure 2. Amphenol (TST-10) appliance turbidity test circuit where $VCC = 5\text{ V}$. Other Amphenol models use the same circuit.

To test the hardware variation between sensors, we created test solutions by adding a small amount of cutting oil to water and tested four appliance sensors of the same model in the same solution. Ideally, the sensors should output the same voltage in the same solution. We performed a simple linear conversion from voltage to approximate NTU using the output curve specified in the data sheet for each sensor. Table 1 shows the observed variation between the sensors in this experiment. The result shows the actual variation is less than the worst-case value calculated from the curve in the data sheet. The TST-10 performed best with 50 NTU difference; however, for most water management applications this variation is far too large to be useful.

Table 1. Variation between the appliance sensors of the same model.

Sensor	Specified Variation (NTU)	Observed Variation (NTU)
TSD-10	305	162
TST-10	325	50
TSW-10	748	348

To improve accuracy, we can individually calibrate each sensor. According to the TST-10 datasheet, the useful range of the sensor is 0–4000 NTU with a voltage differential of 2.7 V. We used tap water ($NTU \approx 0$) and recorded the sensor’s maximum voltage. The minimum voltage is specified at 4000 NTU with output voltage 2.7 V less.

To estimate the sensor’s precision, we can use a first-order linear approximation of the output over the full 4000 NTU range of the sensor. Therefore, the maximum resolution of the sensor using the

Arduino's 10-bit analog to digital converter is 7.25 NTU per analog-to-digital converter (ADC) count. As the last bit of ADC output is typically noisy, we expect the best possible result using this approach to be ± 7.25 NTU with slightly better results under 1000 NTU and slightly worse results over 1000 NTU due to the non-linear output of the sensor. For most water management applications, ± 1 NTU is useful, therefore, we conclude that directly connecting the sensors to the ADC cannot provide the needed resolution for water management applications even without noise or other sources of error.

4. Validation of the Low-Cost Nephelometric Sensor

From our previous experiments with the appliance sensors and the Arduino's ADC, we conclude a nephelometric sensor with higher resolution ADC is necessary to achieve the precision necessary for water management applications. To explore this design space, we first constructed a sample-based sensor similar to the one developed by Kelley et al. [8].

This design overcomes the ADC precision by using a TAOS TSL235R light-to-frequency converter, shown in Figure 3, to measure light intensity rather than providing an analog output. Internally the device has a photodiode sensitive to light in the range 320 nm–1050 nm. The diode current is converted to a square wave with 50% duty cycle where the output frequency is proportional to the light intensity. The range of frequencies that the converter outputs are from 0–800 kHz. Using the Arduino's onboard Timer/Counter and Paul Stoffregen's FreqCount library [21], we can measure the average frequency over a short interval (e.g., 1 s) with very high accuracy and precision. This approach to measuring light intensity results in far greater resolution than what is possible using the Arduino's ADC. As a result, the sensor has a much larger dynamic range yielding higher resolution readings that are no longer strongly limited by the ADC resolution.

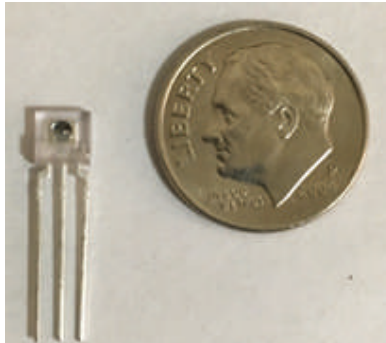


Figure 3. TAOS TSL235R light-to-frequency converter.

To evaluate the sensor, we constructed a simple test tube-based design that was 3D printed shown in Figure 4. The test tube holder allowed the 100 mA IR LED and TAOS TSL234R to be mounted securely in both 90° and 180° configurations. The IR LED was driven by an Arduino GPIO pin through a series 1 kΩ resistor. The frequency count was read using FreqCount on an Arduino Mega 2560.

Figure 5 shows the results from several validation tests of the light-to-frequency sensor. These tests begin without a test tube inserted (Air) and three different empty test tubes. Then we test two solutions, distilled water (≈ 0 NTU) and a 126 NTU calibration solution. The figure shows a box plot of the measured output frequency measurements for each test on the X-axis. Each frequency measurement was generated by averaging 10 samples on the Arduino Mega and was repeated to produce 50–100 data points. From these results, we see little variation between measurements, we can clearly identify empty test tubes with frequency around 52–54 kHz, and an empty test chamber (i.e., no test tube inserted) with frequency around 47 kHz. The median of the 126 NTU calibration solution and distilled water yielded 1329.2 Hz difference. A two-point linear calibration from these values suggests sensing resolution better than 0.1 NTU per Hz may be possible (i.e., 126 NTU/1329.2 Hz = 0.095 NTU/Hz).

Although further tests would need to be performed with more NTU standards to classify the accuracy and ensure a linear response.

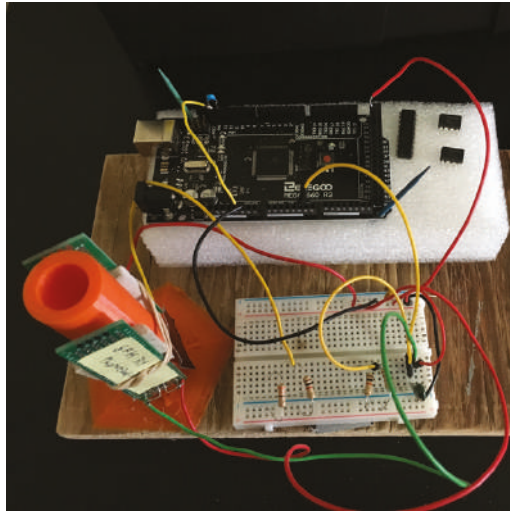


Figure 4. Circular sample holder and test circuit.

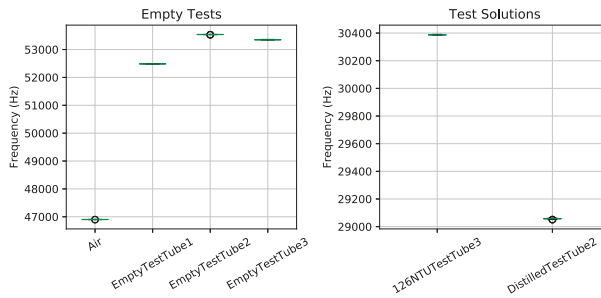


Figure 5. Light-to-frequency initial results using standard test tubes.

However, these results are promising but not as good as those reported by Kelly et al. [8]. We suspect some of the error is due to the large reflections and optical impurities in the test tube. Because of the circular shape of the test tube, it is nearly impossible to keep the IR LED exactly perpendicular to its surface. As a result, we decided to switch to plastic cuvettes as they are similar but lower cost than the quartz cuvettes used by Kelly et al. [8]. Cuvettes have straight sides and are typically used in spectrophotometry where optical clarity is important.

The housing was redesigned to have a square shape with internal walls to block any light from getting to the receiver unless it first went through the sample as shown in Figure 6a. We tested the sample holder with distilled water and a calibration solution. The test solutions were measured with a calibrated Hach 2100P turbidity meter before the experiment and measured 0.39 and 86 NTU, respectively. Figure 6b shows the observed frequency output from the light-to-frequency converter. The median difference between the samples was 581.45 Hz. Assuming a linear response, this would yield a resolution of 0.15 NTU per Hz (85.61 NTU/581.45 Hz). However, there is some overlap in the measured results between the samples and the standard deviation of the samples was large at 142.2 and 254 Hz. Moreover, this resolution is slightly worse than the test-tube-based design.

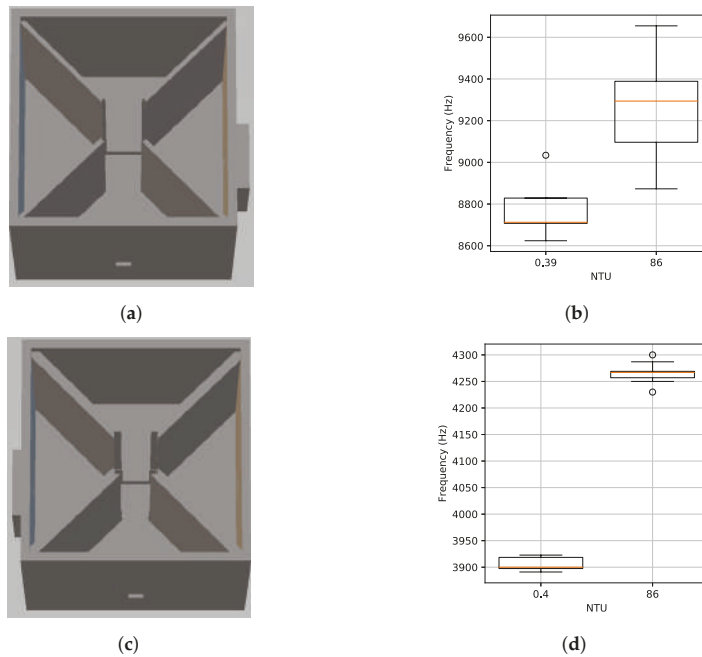


Figure 6. Square cuvette sample holder designs with a light-to-frequency converter at 90° from the IR LED as well as the results from validation tests. (a) Initial square design. (b) Frequency output for initial square sample holder. (c) Revised square sample holder with thicker walls and tighter fit to cuvette. (d) Frequency output for revised square sample holder.

After investigation, we found that the cuvettes could rotate slightly in the sample holder and that external ambient light was causing variation in the output frequency. To rectify these problems, we revised the design to have a tighter fit to the cuvette to eliminate rotation and increased the wall thickness to reduce the effect of external light. The revised sample holder is shown in Figure 6c. We repeated the experiment with distilled water and our calibration solution. The results in Figure 6d show a significant reduction in frequency at both readings and significantly reduced variation. This result is consistent with the reduction of external light and more constant cuvette position. Although the average frequency difference was reduced to 367 Hz (0.23 NTU per Hz), the noise was greatly reduced with standard deviation of 12.0 and 19.0 Hz yielding statistically different readings in all cases.

With these results, we conclude that a sample-based low-cost nephelometric turbidity sensor using a light-to-frequency converter can provide the needed resolution needed for many water quality monitoring applications. Additionally, our revised cuvette-based sample holder successfully reduced variation in the readings. With further study and improvement, such as increasing LED brightness, we believe the performance could be improved further. This general design will be used to inform the future development of a low-cost continuous turbidity sensor.

5. Low-Cost Continuous Turbidity Sensing

From our previous experiments, we have validated that a low-cost nephelometric turbidity sensor can meet the requirements (i.e., better than 1 NTU resolution) needed for providing useful data for water quality monitoring applications. To provide continuous turbidity data, we will adapt the basic sensor design for flow-through applications. Many applications, such as drinking water and agriculture use commonly available pipes to transport water, such as PVC. In the U.S., schedule 40 and

80 are common specifications of PVC pipe which are available in a variety of colors and importantly for this application, clear.

Our approach to the continuous low-cost turbidity monitor is to attach an LED and a light sensor on the outside of a clear PVC pipe segment oriented 90° apart in the nephelometric configuration. In the previous tests, the separation between the LED and sensor was proportional to the width of the cuvette, which is 10 mm. In the piped configuration, this distance will be proportional to the pipe size, which could be several inches. Because the LED will be illuminating a much larger volume of water through a much thicker wall, we surmise it is useful to increase the brightness. High-powered IR LEDs (several watts) are not readily available and specialty IR LEDs are expensive. However, high-powered white LEDs are common. As a result, we replaced the IR LED with a commonly available Cree XLamp white LED (4000 K). To properly drive the LED, we use a commonly used constant current LED driver (Diodes Incorporated AL8805) configured to deliver up to 500 mA of current to the LED via a PWM control signal. This allows us to also replace the IR light-to-frequency converter with a low-cost ambient light sensor (TSL4531). These sensors are commonly used to control display brightness and provide a digital i2c output of light intensity as an integer value that is calibrated to lux. To support wireless data collection, we connect the LED driver and light sensor to an ESP32 Wi-Fi-enabled microcontroller. A diagram of the complete low-cost continuous turbidity sensing system is shown in Figure 7.

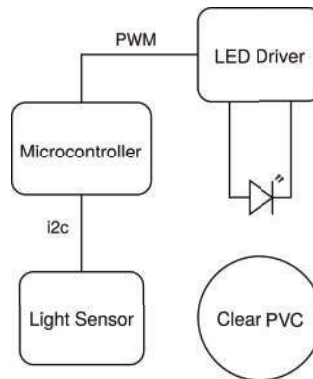


Figure 7. Low-cost continuous turbidity monitoring system diagram.

To provide consistent contact with the PVC pipe, we designed a 3D-printable mounting ring to mechanically fix the LED and sensor to the pipe. Different pipe diameters can be accommodated by adjusting the dimensions of the mounting ring. Figure 8 shows a rendering of (a) our initial design and (b) revised mounting ring. With the initial design, the LED and ambient light detector were mounted to a small PCB and glued to the mounting ring. Because the PCB used through-hole connections, solder joints on the bottom of the PCB caused an uneven fit with the ring. This mechanical ring was also narrow (1 inch) and allowed ambient light to reach the light sensor. As a result, the design was revised to include PCB standoffs, recessed areas to accommodate solder joints, screw holes were added to the ring, and the height of the ring increased to block more ambient light. The mounting ring was sized to tightly fit over a section of 2-inch schedule 40 clear PVC pipe and printed in black ABS on an Ultimaker 2+ 3D printer. Black was selected to minimize reflected light in the device. Although we did not characterize this effect, we tested other colors and found black to have the lowest light level with the LED on. This suggests that reflections are minimized as desired.

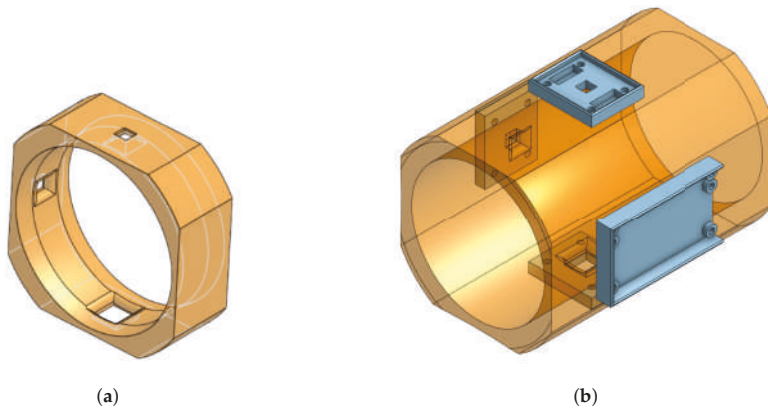


Figure 8. Nephelometric sensor mounts for clear pipes. (a) Initial design. (b) Revised design including PCB mounts and reduced ambient light.

The approximate unit component cost of the completed sensor is 64 USD. The component costs are shown in Table 2. This makes the low-cost continuous turbidity monitor more expensive than the affordable open-source turbidimeter (\$25–\$35) by Kelley et al. [8]. However, much of the cost difference is due to the WiFi microcontroller and printed circuit boards which add significant value by providing wireless communication and improved reliability over a breadboard circuit. This also compares favorably to commercial turbidity probes for water quality from manufacturers such as YSI, In situ, and Eureka where prices range from \$1000 to \$5000, depending on the specific model. Even compared to the low-cost autonomous optical sensor by Murphy et al. at €650 [17], we see a significant reduction in cost.

Table 2. Unit component cost of the prototype sensor.

Component	Approximate Cost (USD)
ESP32 microcontroller	20
TSL4531 light sensor	1
XLamp MX-6 LED (2)	2
Printed circuit boards	10
PVC pipe 2 in × 12 in	16
Black ABS filament (83 g)	5
Miscellaneous components	10
Total	64

5.1. Laboratory Calibration

Four low-cost continuous turbidity monitors were constructed and tested over the range of 0–100 NTU to explore the variation that exists in the different devices made from the same components. The devices are labeled with the last two digits of their ESP32 WiFi MAC address. For calibration, the devices were oriented vertically over a short section of clear PVC pipe with silicone caulk securing the mounting ring to the pipe and a Qwik Cap sealing the bottom as shown in Figure 9. Test solutions were added to fill the PVC pipe and a cover was placed over the top to block ambient light.



Figure 9. Sensor 18 configured for laboratory calibration.

The test solutions were created by diluting a 4000 NTU formazin standard with deionized water (≈ 0.20 NTU) to produce solutions with values of (0.20, 5, 20, 40, and 100 NTU) [22]. The test solutions were made, and the devices were filled with deionized water and allowed to collect data for 12 h. This allowed the components and test solutions to reach a constant temperature and any air bubbles to dissipate. The devices were rinsed thoroughly with deionized water between different samples to clean any residual sample out of the pipe. Each of the samples was tested in each device for at least 10 min where the light intensity at 90-degrees, 180-degrees and the dark reading (90-degree sensor reading without the LED on) was measured every 6 s during the sampling interval. If more than 100 samples were collected for a given test solution, only the middle 100 samples were used in the analysis. Manual turbidity readings were also made of the test sample every 2 min using a Hach 2100P turbidity meter. This was done as a single reading from the meter can vary. We do not believe that the standards degraded during the testing.

After the laboratory sampling was complete, the data from each device was fit to a model of the form:

$$NTU = c_1 \times d_0 + c_2 \times d_{90} + c_3 \times d_{180} + \epsilon \quad (1)$$

where d_0 is the light intensity at 90 degrees from the LED with the LED off in lux, d_{90} is the light intensity with the LED on at 90 degrees from the LED in lux, d_{180} is the light intensity with the LED on at 180 degrees from the LED in lux, and ϵ is the y-intercept. These values were computed using ordinary least squares linear regression comparing the predicted NTU to the average manual NTU reading of the sample. Models were generated for each device individually in addition to a combined model using data from all the devices. To explore the impact of each sensor (90 degrees and 180 degrees from the LED), models were generated with each sensor individually as well as both of the sensors. Table 3 shows all computed model parameters, the R^2 measure, and variance (σ^2) of the residual.

Table 3. Individual and combined model parameters, R^2 , and residual variance (σ^2) for using the 90- and 180-degree sensors, only the 90 degree, and only the 180 degree sensor respectively. The units of c_1 , c_2 and c_3 are NTU/lux. The unit of ϵ and σ^2 are NTU and NTU² respectively.

Device	Sensor (s)	c_1	c_2	c_3	ϵ	R^2	σ^2
Device 18	d_{90}, d_{180}	-0.2956	0.1608	-0.0046	41.2997	1.0000	0.0093
Device 18	d_{90}	-0.2970	0.2088	0.0000	-16.0266	0.9999	0.0316
Device 18	d_{180}	-0.3372	0.0000	-0.0200	232.7049	0.9989	0.2582
Device 8C	d_{90}, d_{180}	0.1112	0.2313	0.0018	-38.2779	0.9998	0.2446
Device 8C	d_{90}	0.1055	0.2136	0.0000	-15.4716	0.9998	0.2570
Device 8C	d_{180}	0.3477	0.0000	-0.0212	259.3874	0.9984	2.3556
Device 94	d_{90}, d_{180}	-0.0995	0.3770	0.0117	-174.0959	0.9996	0.5432
Device 94	d_{90}	-1.1277	0.2398	0.0000	-17.6853	0.9993	1.0413
Device 94	d_{180}	-2.5629	0.0000	-0.0204	254.4228	0.9972	4.2926
Device B8	d_{90}, d_{180}	-0.5757	0.3274	0.0059	-100.8465	0.9999	0.1515
Device B8	d_{90}	-0.9409	0.2537	0.0000	-21.2899	0.9997	0.4269
Device B8	d_{180}	-1.9002	0.0000	-0.0201	251.4739	0.9957	5.5707
Combined	d_{90}, d_{180}	1.6055	0.2252	-0.0003	-13.6549	0.9934	8.0515
Combined	d_{90}	1.6541	0.2286	0.0000	-17.8185	0.9934	8.0627
Combined	d_{180}	1.2328	0.0000	-0.0202	246.3589	0.9558	53.9348

The value of c_2 is expected to be positive as more light reflected at 90 degrees would be more indicative of a turbid solution and all the models follow this. The value of c_3 is expected to be negative as the more turbid the solution, the less light that would pass straight through it to reach the d_{180} sensor. Device 8C, 94, and B8's models including both sensors (d_{90}, d_{180}) do not follow this expectation and have a reduced magnitude, suggesting the d_{180} sensor provides inconsistent data in this NTU range.

From these results, we see that in general, the computed model fits the data well for the d_{90} and d_{180} as well as the d_{90} only device-specific models. The variance using both sensors was slightly smaller, suggesting that the d_{180} sensor does provide some information when used with the d_{90} sensor. The d_{180} only models have significantly larger variance when compared to the other models. The combined model also has variance that is more than an order of magnitude larger, even with both sensors, indicating there is variation between devices. This variation could be caused by the mechanical assembly construction, different brightness of the LED resulting from manufacturing differences in the LED itself or LED driver circuit, and manufacturing differences that impact the clarity of the PVC pipe. The idea of device-specific calibration is not unique to low-cost sensing. It is widely used in many manufacturing processes to compensate for errors caused by real-world manufacturing constraints without having to determine each source of variance. As a result, we omit the combined model from further analysis.

To visually explore the results, Figure 10 shows several plots for the predicted NTU vs. measured NTU using the low-cost turbidity monitor. Each row presents results from a specific device while each column shows increasing NTU ranges. Missing plots result from not testing every sample on every device. The results with only the 180-degree sensor are omitted for clarity as this case performed significantly worse than the others. If the model were to produce the exact same value as the measured readings, the points would fall on the dotted diagonal line. The further the points fall from the diagonal line the larger the error of the prediction. For example, the B8 device model can predict the NTU readings for all the samples within about ± 1.0 NTU. The B8 model overpredicts the NTU for the 38 to 40 NTU sample and underpredicts the NTU for the 20 to 22 NTU sample. The diagonal line bisects the plotted points for the 0 to 1 NTU sample and the 95 to 100 NTU standard, suggesting that the model, on average, predicts these cases well.

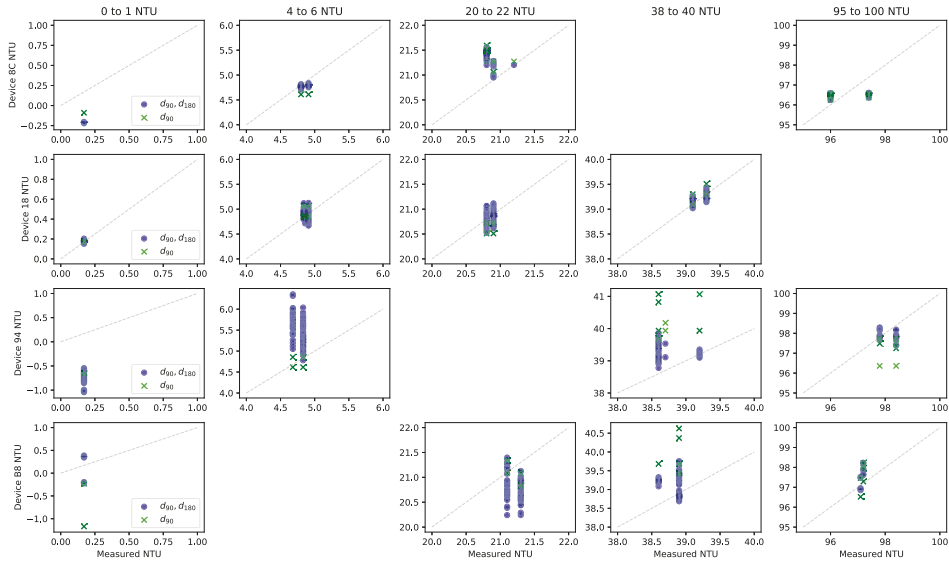


Figure 10. Predicted NTU vs. measured NTU for the individual models on the 5 tested NTU ranges.

To better understand these results, Figure 11 shows the cumulative distribution function (CDF) of the absolute value of the residual using the computed models. The residual is the difference between the estimated value and measured value computed individually for both sensor configurations. The range is limited to (0, 1) for clarity. Residuals from all device-specific models are combined in the final “All Devices” plot. The d_{180} model is not shown because it performed significantly worse than the others. We see the devices perform similarly with most of the residuals less than 1 NTU. Device 18 does the best and 94 does the worst while 8C and B8 are in the middle. For all devices, with both sensors, the median residual was -0.0032 NTU with a standard deviation of 0.4870 NTU.

Figure 12 shows the CDF of the combined absolute value of the residuals from all device-specific models at each tested NTU range. This confirms that the device can be used over this whole range with consistent performance. However, this uniformity is mostly a result of performing linear regression with an equal number of data points (100) in each range. By oversampling any particular NTU range, the generated model would produce a better fit in that range at the expense of performance in the other ranges. This could be useful in certain applications to better detect small variations from an expected turbidity value.

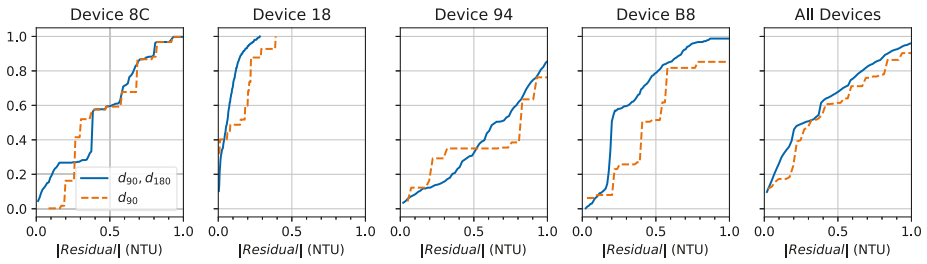


Figure 11. Cumulative distribution function of the absolute value of the residual by device.

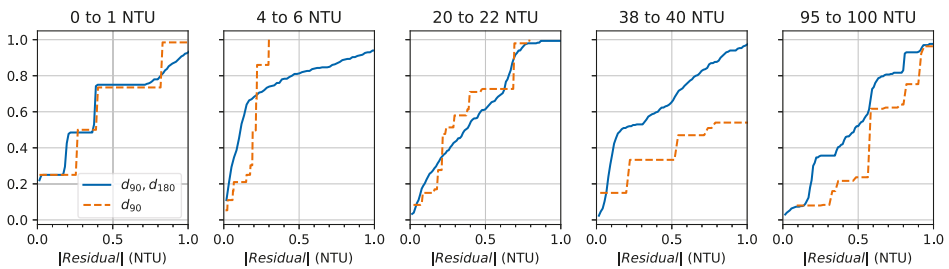


Figure 12. Cumulative distribution function of the absolute value of the residual by NTU range.

These results show that with device-specific calibration the device will achieve accuracy closer to 1.0 NTU than our goal of 0.10 NTU over the range of 0–100 NTU. However, since the median residual was near zero, averaging multiple samples could reduce noise to approach this goal. This dataset did not have enough samples to fully investigate this question, so we will explore this in the next section.

5.2. Pumped Tank Test

Having calibrated and explored the performance of the low-cost continuous turbidity monitor in a laboratory setting, we now move to a simulated real-world test. For this test, we used a 1000-gallon water tank and a 1000 GPH pool pump to circulate the water. To explore if the device should be on the pump inlet or outlet, we installed a device on both. Device B8 was installed on the pump inlet and device 94 was installed on the pump outlet. Figure 13 shows a diagram of the pumped tank test. The sensors were installed using three-foot pipe segments between the tank and the pump.

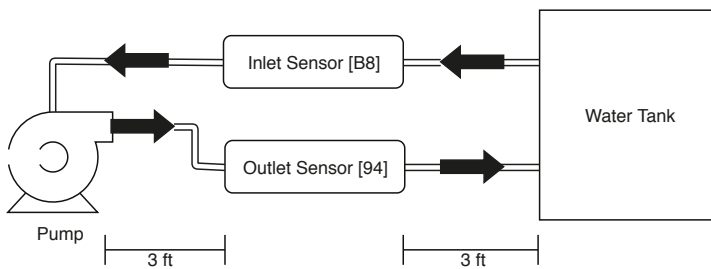


Figure 13. Diagram of pumped tank test.

The tank was filled with fresh drinking-quality water and manual turbidity measurements were made daily with the Hatch 2100P turbidimeter. These measurements were linearly interpolated

between samples to produce a continuous turbidity value in the tank for analysis. The low-cost continuous turbidity monitor readings were made once every 6 s. Timestamps for each sample were recorded by the device and the clock was synchronized with a public NTP server at the start of the experiment. The timestamp and raw sensor values were then transmitted over a WiFi network to a database for storage. For analysis, the raw sensor values were linearly interpolated to a constant 1 Hz rate and a 20-min moving average of 1200 samples at 1 Hz containing about 200 raw samples was computed over 5-min periods, resulting in 288 samples per day. We chose these values to reduce the amount of data as we expect turbidity to change relatively slowly and simultaneously reduce sensor noise by averaging multiple readings. Experimentally we found that averaging over 1-min periods (10 raw samples) was sufficient to eliminate most of the sensor noise but we elected to use longer periods in our analysis to produce the desired sample rate.

The filtered sensor readings were then used in the device-specific laboratory models (Table 3) to estimate the NTU reading in the tank. A small offset was present at installation, so we adjusted each device's ϵ parameter after making the first manual reading to remove this error. Shortly after the installation, device 94 failed and the LED and light sensor was replaced with the components from device 18. Data is reported as device 94; however, the model generated by device 18 is used to predict NTU. Figure 14 shows results for 38 days of measurements. During two intervals between days 5 and 7, the data collection failed, and no samples were recorded. For analysis, the missing data were linearly interpolated between the available samples.

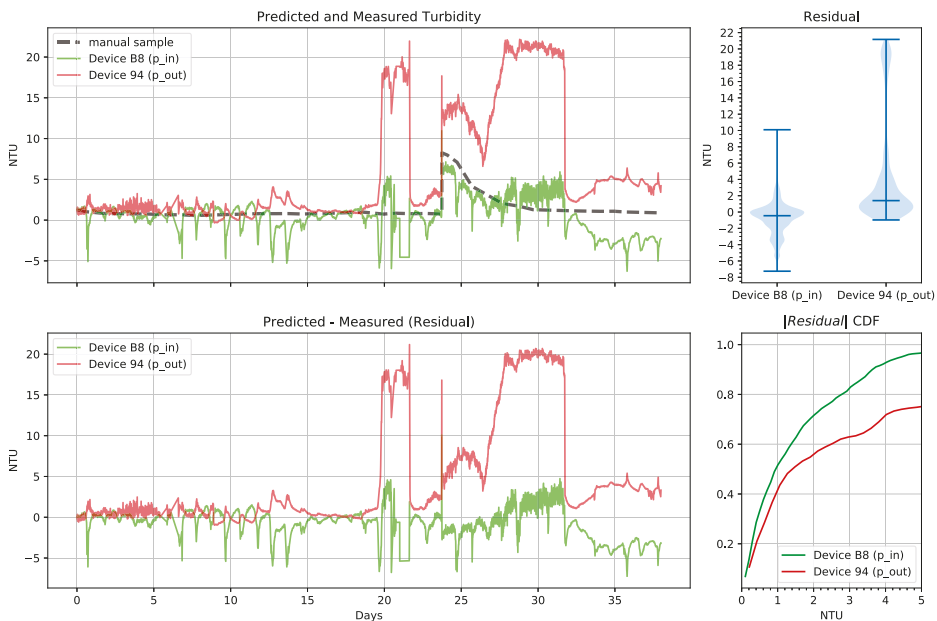


Figure 14. Pumped tank low-cost continuous turbidity monitor predictions from the pump inlet (p_in) and outlet (p_out) and manual measurements from a hand-held turbidimeter showing all collected data (days 0 through 37).

Initially, through day 5, the sensor on the outlet had significant noise. On day 6 we discovered that bubbles were present in the pipes near the outlet sensor and we purged the air from the pipes. On day 9 we discovered that a small hole was allowing air into the pipes. We sealed the hole and

both sensors showed significantly reduced noise after this. In sealing the hole, we repositioned the outlet sensor, which caused an offset in the readings. At day 20 there was another air leak that caused a significant error and was sealed by day 22.

To investigate the response of the sensor to changing turbidity, we continued our measurements and added one quarter cup of Coffee Mate[®] powdered coffee creamer to the 1000-gallon tank on day 23 at the pump inlet. This quickly increased the tank turbidity to about 8 NTU. The inlet sensor closely tracked this change demonstrating the impulse response of the sensor. On day 27 both sensors NTU reading began increasing and we discovered the patch to the pipe had failed. We let this continue until day 32 when it was patched again.

The median residual and standard deviation for the inlet and outlet low-cost continuous turbidity monitors over the entire test were -0.4507 , 1.9063 NTU and 1.3997 , 6.5511 NTU, respectively. The cumulative distribution function of the absolute value of the residual shows that overall only slightly more than 50% of the predictions are within 1 NTU as expected from the laboratory tests even with the better performing inlet monitor. However, the large errors resulted from air in the pipes. When no air was present on days 15 through 17, the median residual and standard deviation was -0.1881 , 0.2643 NTU and 0.2266 , 0.1138 NTU respectively and all of the predictions were within 1 NTU with 80% of them being within 0.5 NTU.

Comparing the inlet and outlet monitors in the presence of bubbles on days 20 and 27, we see the inlet is much less sensitive to the presence of bubbles. We speculate that by going through the pump, the relatively large bubbles passing through the inlet monitor were broken up into many more small bubbles before passing through the outlet monitor. This resulted in a correspondingly larger estimated turbidity on the outlet monitor.

Both sensors showed patterns of daily periodic errors. These patterns are more apparent when examining the relatively stable period between days 15 through 17, shown in Figure 15. On this plot we added the measured solar radiation (W/m^2) from a nearby weather station for reference. The inlet sensor has a more negative residual during the day while the outlet sensor has a more positive residual and the Pearson correlation coefficients between the residual and the solar radiation was -0.58 and 0.17 respectively. To explain the difference in sign, we reexamine the model parameters from Table 3 and recall that the parameter c_3 has the opposite sign between these two devices. Furthermore, the absolute value of the parameter is larger for the inlet device. This parameter corresponds to the 180 degree sensor. As a result, we conclude that this phenomenon is almost certainly caused by ambient light. While both sensors and devices were affected, the 180 degree sensor on device B8 was the most sensitive to ambient light. The position of the devices in the test also contributed to these differences. Because our laboratory experiments were taken in relatively dark conditions, the model did not properly account for the influence of ambient light even with the dark term in the model.

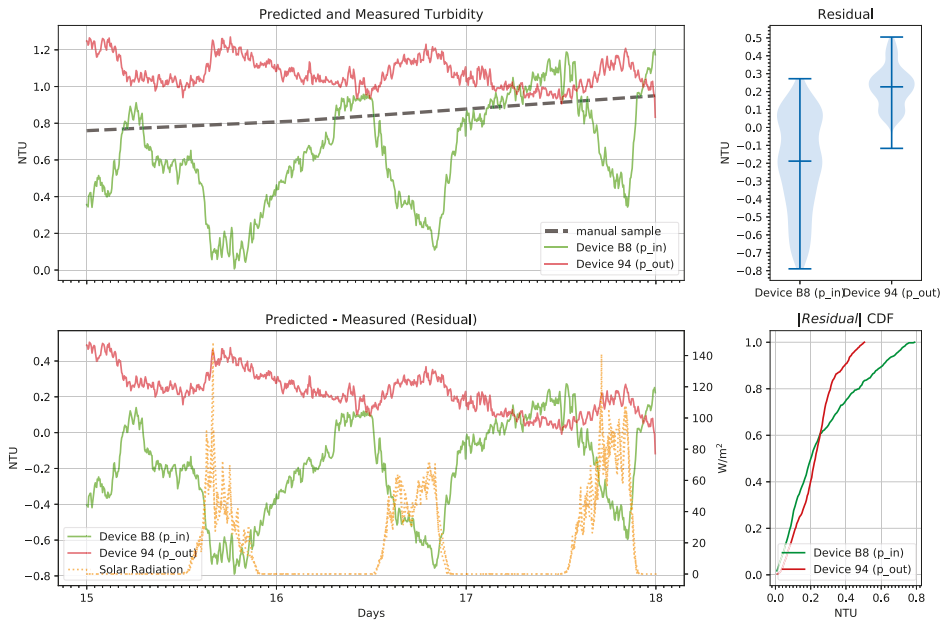


Figure 15. Pumped tank low-cost continuous turbidity monitor predictions from the pump inlet (p_in) and outlet (p_out) and manual measurements from a hand-held turbidimeter showing days 15 through 17.

5.3. Discussion

In this section, we describe the creation of a low-cost continuous nephelometric turbidity monitor built using commonly available components. The turbidity monitor is designed to fit over a short section of clear PVC pipe. This approach reduces the mechanical complexity of the system since no sensing components are ever in direct contact with water.

Laboratory experiments demonstrated the model was able to reliably estimate turbidity within 1 NTU with some noise present in the readings. Since the median residual was near 0, averaging multiple readings could approach our goal of 0.1 NTU resolution under well-controlled conditions.

The pumped tank test demonstrated that the sensor can continuously predict turbidity installed either on the inlet and outlet of a pump. However, the inlet sensor had better impulse response to a turbidity change. The inlet sensor showed more interference from ambient light, but we attribute this to sensor positioning and not an artifact of the pump position. The outlet of the pump was more affected by bubbles, this was attributed to the fact the pump formed some bubbles during operation. These bubbles likely dissipated when they reached the tank resulting in the inlet sensor not seeing the same level of bubbles. Overall, neither sensor achieved the same accuracy as in the lab experiment, even with averaging many sensor readings. However, on days 15–17 when no air was present, the performance of both sensors was equal to the lab experiments. By eliminating ambient light and bubbles we believe this level of performance can be maintained over longer periods. Furthermore, even at the current level of performance, many applications could benefit from low-cost continuous turbidity monitoring by detecting larger changes in turbidity (e.g., >1 NTU). Results from the last days of the experiment showed a significant offset was present suggesting that periodic calibration may be required. We plan to explore the long-term stability of the low-cost continuous turbidity monitor in future work.

6. Conclusions and Future Work

In this paper, we explored the development of a low-cost continuous turbidity monitor. We began by evaluating readily available appliance turbidity sensors. While inexpensive, in our tests they do not have the required accuracy for water quality monitoring applications. They were also prone to a large amount of noise and are difficult to precisely calibrate. Examining prior work on low-cost turbidity sensors, we verified that accurate low-cost sample-based turbidity sensors can be constructed. In our tests, the main source of error was the imprecision of the sample holder (Cuvette or Test Tube) in the sensor apparatus. Using this design as a starting point, we adapted the sensor for use in piped-water applications. Lab tests verified that with individual calibration, accuracy better than 1 NTU is possible over the range 0–100 NTU. A 38-day long experiment was performed with the low-cost continuous turbidity monitor in a piped-water application. The monitor showed more error than in the lab experiments, yielding ≈ 5 NTU accuracy and good response to changes in turbidity. The primary source of error was attributed to bubbles in the liquid and ambient light. This may be sufficient for some continuous monitoring applications. For other applications where higher accuracy is needed, we believe that by reducing ambient light on the sensor and eliminating all air from in the pipes will yield accuracy better than 1 NTU. Like all other turbidity sensors, periodic calibration is necessary to maintain the accuracy of the low-cost continuous turbidity monitor.

As we found that device-specific calibration significantly improves performance, a simpler way to calibrate the sensor is recommended as lab-made turbidity standards are not commonly available by citizen scientists. There are other processed liquids that have consistent turbidity such as apple juice and tea which could be used for calibration. A validated procedure to calibrate the sensor with these liquids could be developed. We also plan longer trials to verify the long-term behavior of the low-cost continuous turbidity monitor. One long-term concern is if and when to remove and clean the clear PVC section. Since PVC can develop a static charge, contaminants may be attracted to the clear pipe segment. It is not clear if the pumped liquid is sufficient to remove these contaminants. We plan to redesign the mounting ring to simplify removal for inspection and cleaning.

Author Contributions: Conceptualization, Methodology, Software, Formal Analysis, Investigation, Data Curation, Writing—Original Draft Preparation, Writing—Review & Editing, Visualization, A.M. and D.G.; Validation, D.G.; Resources, Supervision, Project Administration, Funding Acquisition, A.M.

Funding: This research received no external funding.

Conflicts of Interest: The authors declare no conflict of interest.

References

1. United Nations Educational, Scientific and Cultural Organization (UNESCO). Water in the post-2015 development agenda and sustainable development goals. In *International Hydrological Programme (IHP)*; UNESCO: Paris, France, 2014.
2. Duan, W.; Takara, K.; He, B.; Luo, P.; Nover, D.; Yamashiki, Y. Spatial and temporal trends in estimates of nutrient and suspended sediment loads in the Ishikari River, Japan, 1985 to 2010. *Sci. Total Environ.* **2013**, *461–462*, 499–508. [[CrossRef](#)] [[PubMed](#)]
3. Duan, W.; He, B.; Nover, D.; Yang, G.; Chen, W.; Meng, H.; Zou, S.; Liu, C. Water Quality Assessment and Pollution Source Identification of the Eastern Poyang Lake Basin Using Multivariate Statistical Methods. *Sustainability* **2016**, *8*, 133. [[CrossRef](#)]
4. Duan, W.; He, B.; Chen, Y.; Zou, S.; Wang, Y.; Nover, D.; Chen, W.; Yang, G. Identification of long-term trends and seasonality in high-frequency water quality data from the Yangtze River basin, China. *PLoS ONE* **2018**, *13*, 1–18. [[CrossRef](#)] [[PubMed](#)]
5. Burke, D.G.; Allenby, J. Low Cost Water Quality Monitoring Needs Assessment. Available online: <https://chesapeakeconservancy.org/what-we-do/innovate/water-quality-monitoring/low-cost-water-quality-monitoring/> (accessed on 1 February 2019).

6. Metzger, M.; Konrad, A.; Blendinger, F.; Modler, A.; Meixner, A.; Bucher, V.; Brecht, M. Low-Cost GRIN-Lens-Based Nephelometric Turbidity Sensing in the Range of 0.1–1000 NTU. *Sensors* **2018**, *18*, 1115. [[CrossRef](#)] [[PubMed](#)]
7. Hicks, S.; Aufdenkampe, A.; Montgomery, D. Creative Uses of Custom Electronics for Environmental Monitoring at the Christina River Basin CZO. In Proceedings of the American Geophysical Union Annual Fall Meeting, San Francisco, CA, USA, 3–7 December 2012.
8. Kelley, C.; Krolick, A.; Brunner, L.; Burklund, A.; Kahn, D.; Ball, W.; Weber-Shirk, M. An Affordable Open-Source Turbidimeter. *Sensors* **2014**, *14*, 7142–7155. [[CrossRef](#)]
9. Attivissimo, F.; Carducci, C.G.C.; Lanzolla, A.M.L.; Massaro, A.; Vadrucchi, M.R. A Portable Optical Sensor for Sea Quality Monitoring. *IEEE Sens. J.* **2015**, *15*, 146–153. [[CrossRef](#)]
10. Lambrou, T.P.; Panayiotou, C.G.; Anastasiou, C.C. A low-cost system for real time monitoring and assessment of potable water quality at consumer sites. In Proceedings of the SENSORS, Taipei, Taiwan, 28–31 October 2012; pp. 1–4. [[CrossRef](#)]
11. Parra, L.; Sendra, S.; García, L.; Lloret, J. Design and Deployment of Low-Cost Sensors for Monitoring the Water Quality and Fish Behavior in Aquaculture Tanks during the Feeding Process. *Sensors* **2018**, *18*, 750. [[CrossRef](#)] [[PubMed](#)]
12. Adu-Manu, K.S.; Tapparelo, C.; Heinzelman, W.; Katsriku, F.A.; Abdulai, J.D. Water Quality Monitoring Using Wireless Sensor Networks: Current Trends and Future Research Directions. *ACM Trans. Sens. Netw.* **2017**, *13*, 4:1–4:41. [[CrossRef](#)]
13. O'Dell, J.W. *Method 180.1 Determination of Turbidity by Nephelometry*; Environmental Monitoring Systems Laboratory Office of Research and Development U.S. Environmental Protection Agency: Cincinnati, OH, USA, 1993.
14. Fondriest Environmental, Inc. *Fundamentals of Environmental Measurements: Measuring Turbidity, TSS, and Water Clarity*. 2014. Available online: <https://www.fondriest.com/environmental-measurements/measurements/measuring-water-quality/turbidity-sensors-meters-and-methods/> (accessed on 1 May 2018).
15. Mizaikoff, B. Infrared optical sensors for water quality monitoring. *Water Sci. Technol.* **2003**, *47*, 35–42. [[CrossRef](#)] [[PubMed](#)]
16. Bin Omar, A.; Bin MatJafri, M. Turbidimeter Design and Analysis: A Review on Optical Fiber Sensors for the Measurement of Water Turbidity. *Sensors* **2009**, *9*, 8311–8335. [[CrossRef](#)] [[PubMed](#)]
17. Murphy, K.; Heery, B.; Sullivan, T.; Zhang, D.; Paludetti, L.; Lau, K.T.; Diamond, D.; Costa, E.; O'Connor, N.; Regan, F. A low-cost autonomous optical sensor for water quality monitoring. *Talanta* **2015**, *132*, 520–527. [[CrossRef](#)]
18. Amphenol. *TST-10 Turbidity Sensor Datasheet*; Amphenol Thermometrics, Inc.: St. Marys, PA, USA, 2014.
19. Amphenol. *TSD-10 Turbidity Sensor Datasheet*; Amphenol Thermometrics, Inc.: St. Marys, PA, USA, 2014.
20. Amphenol. *TSW-10 Turbidity Sensor Datasheet*; Amphenol Thermometrics, Inc.: St. Marys, PA, USA, 2014.
21. Stoffregen, P. FreqCount Library. Available online: <https://github.com/PaulStoffregen/FreqCount> (accessed on 1 May 2018).
22. Sadar, M. *Turbidity Standards*; Technical Information Series—Booklet No. 12; Hach Company: Loveland, CO, USA, 2003.



© 2019 by the authors. Licensee MDPI, Basel, Switzerland. This article is an open access article distributed under the terms and conditions of the Creative Commons Attribution (CC BY) license (<http://creativecommons.org/licenses/by/4.0/>).